

# Clear-air turbulence and gravity waves in a front/jet system

Diplomarbeit im Fach Meteorologie  
von  
Christian Kühnlein

Fakultät für Physik der Ludwig-Maximilians-Universität  
München

2006



---

# Contents

<b>1</b>	<b>Introduction</b>	<b>5</b>
<b>2</b>	<b>Analysis of the front/jet system</b>	<b>9</b>
2.1	Evolution of the large-scale flow . . . . .	9
2.2	Observations . . . . .	15
<b>3</b>	<b>Mesoscale Numerical Simulations</b>	<b>23</b>
3.1	Comparison with ECMWF analyses . . . . .	23
3.2	Inertia-gravity wave dynamics . . . . .	26
3.3	Comparison with observations . . . . .	39
3.4	Differences between MM5 simulations . . . . .	44
<b>4</b>	<b>Clear-air turbulence generation mechanisms</b>	<b>49</b>
4.1	Wave-turbulence coupling . . . . .	49
4.2	Some hypotheses about the clear-air turbulence generation . . . . .	50
<b>5</b>	<b>Inertia-gravity wave source dynamics</b>	<b>53</b>
5.1	Spontaneous adjustment . . . . .	53
5.2	Shear generation . . . . .	62
5.3	Moist convective generation . . . . .	62
5.4	Summary . . . . .	65
<b>6</b>	<b>Conclusion</b>	<b>67</b>
	<b>Appendix A</b>	<b>69</b>
	MM5 model configuration . . . . .	69
	<b>Acronyms</b>	<b>71</b>
	<b>Bibliography</b>	<b>73</b>
	<b>Danksagung</b>	<b>79</b>
	<b>Erklärung</b>	<b>81</b>



# 1 Introduction

Aircraft flying in the free atmosphere rarely encounter turbulence. However, serious turbulence encounters occur over mountains and in the vicinity of convective storms or jet streams. Even over the ocean, clear-air turbulence (CAT<sup>1</sup>) encounters can lead to injuries and fatalities. Serious CAT encounters over the Pacific Ocean are rather frequent. They mostly occur in the vicinity of the meandering subtropical jet (STJ). It is an unsolved question which jetstreams have severe CAT and others do not.

In this thesis, we investigate a particular CAT encounter by a research aircraft several hundred kilometers north of the Hawaiian Islands in January 1998. In this case, the in-situ measurements indicated vertical accelerations up to  $\pm 4.8 \text{ ms}^{-2}$  (0.5 g's) in the region of an upper-level front/jet system above the Pacific Ocean. An unexpected encounter of a commercial airplane with accelerations of that magnitude and scale could be a danger to the aircraft and passengers. We strive to identify the peculiarities of this case in order to build hypotheses under which dynamical conditions the production of moderate-to-severe CAT occurs.

Turbulent motions are irregular and appear as strongly vortical motions with spatial scales considered here equal to or smaller than  $\sim 100 \text{ m}$ . Their spatial and temporal occurrence is rather spotty. Early radar observations revealed a vertical scale of  $\sim 100 \text{ m}$  (Browning 1971), whereas CAT areas can spread over a region of  $\sim 100 \text{ km}$ . Sometimes, these CAT regions are accompanied by high vertical accelerations and strong windshears (e.g. Dutton and Panofsky 1970; Ellrod and Knapp 1992; Lane et al. 2004). However, CAT events which affect aircraft can be either really turbulent or consist of wavy motions with a small horizontal scale (e.g. Lane et al. 2003; Jiang and Doyle 2004).

A well-known source of CAT production is the Kelvin-Helmholtz or shearing instability of a stably stratified shear flow (Atlas et al. 1970; Browning 1971). Maximum amplification of the instability is reached when the vertical profile of the horizontal velocity has an inflection point, e.g. above and below the core of a jet stream. The necessary condition for a steady, linear and inviscid shear flow is that the gradient Richardson number falls below a critical value  $Ri_c$ . In the literature,  $Ri_c = 0.25$  was derived for a two-dimensional problem (Miles 1961; Howard 1961), but there are indications that  $Ri_c = 1.0$  should be used for a three-dimensional problem (Miles 1986).

A further source of CAT constitutes overturning or breaking gravity waves. If we speak of gravity waves (sometimes called buoyancy waves) in this thesis, we refer to

---

<sup>1</sup>The term clear-air turbulence especially refers to turbulence occurring several kilometers above the earth's surface in an environment free of clouds and strong convective updrafts (Dutton and Panofsky 1970).

internal oscillations in a stably stratified fluid where the forces acting in the vertical direction are buoyancy and the earth's gravity. Gravity waves having intrinsic frequencies  $\hat{\omega}$  in the range  $N > \hat{\omega} > f$  and small aspect ratios (vertical/horizontal scale  $\ll 1$ ) are referred to as hydrostatic waves. Here,  $N$  and  $f$  represent the Brunt-Väisälä frequency and the Coriolis parameter, respectively. According to (Gill 1982), these waves propagate vertically. For large temporal scales ( $\hat{\omega} \sim f$ ), the Coriolis force becomes important as well, and the hydrostatic gravity waves under the influence of rotation are then commonly named inertia-gravity waves (IGWs) or low-frequency gravity waves, e.g. Holton 1992. Their propagation direction is slanted and typical horizontal wavelength is  $\sim 100$  km.

Gravity waves are ubiquitous in the atmosphere and appear from many different sources. The most important ones are the flow over topography and moist convection. Gravity waves, with typically greater aspect ratios ( $< 1$ ), excited from flow over mountainous or hilly terrain are known sources of CAT. These mountain waves can propagate upwards from the ground into the free atmosphere and break down, thereby possibly producing strong CAT (e.g. Clark et al. 2000; Jiang and Doyle 2004). Convectively generated gravity waves are sources of CAT, too. In an investigation of the generation of turbulence above deep convection through very high-resolution numerical simulations, Lane et al. 2003 found that small-scale gravity waves with a horizontal wavelength around 6 km excited by the convective updrafts broke down in a layer of 4 km deep and 30 km wide above the cloud top.

Another, less investigated source of CAT production is the coupled front/jet system. A variety of mechanisms in amplifying and breaking baroclinic waves can cause CAT (Ellrod and Knapp 1992). Gravity waves in front/jet environments are generated by spontaneous (geostrophic, balance) adjustment, shearing instability, symmetric instabilities, accelerating fronts and frontal convection (Fritts and Alexander 2003, and references therein). Especially, over flat terrain or over the oceans, these are likely candidates for the dynamical causes of CAT.

The prediction of CAT in the troposphere and lower stratosphere is a major challenge because of the multiple scales involved in the phenomenon. However, CAT prediction is an important task for the increasing air traffic (e.g. Eichenbaum 2003). Unfortunately, current CAT forecast products are not sophisticated enough to provide a reliable prediction for airlines (Sharman et al. 2006).

Nowadays, the short-range and medium-range synoptic-scale weather forecasts are fairly accurate. So we can expect an improved prediction of the conditions (e.g. deformation, vertical shear and stability) under which CAT is produced. The model-resolved flow and the turbulent scales are dynamically linked by the divergence of the turbulent fluxes. Although it is obvious that CAT is intrinsically unpredictable, the deterministic procedure appears reasonable since turbulence theory shows a downscale cascade of energy (e.g. Dutton and Panofsky 1970). It is known that the correlation between model-resolved Richardson numbers and the turbulent vertical velocity variance is rather low (Bacmeister et al. 1994; Smith and DelGenio 2001). However, current operational CAT

forecast schemes use so-called CAT-indices based on resolved-scale quantities. Besides the Richardson number, many other CAT-indices are calculated on the model grid (e.g. deformation, unbalanced flow indicators, horizontal temperature gradient, eddy dissipation rate, frontogenesis function, vertical velocity, etc.). Sharman et al. 2006 could show that a combination of 10 different CAT-indices weighted with near-realtime information (i.e. pilot reports of turbulence (PIREPs)) increases the skill of the CAT forecast products in the range of 6 to 48 h.

Recent research suggests the use of a measure of gravity wave activity in order to improve CAT prediction algorithms in forecast models. This arose from findings of a causal relationship between IGWs and CAT occurrences through observations and high-resolution numerical simulations (Pavelin et al. 2001; Lane et al. 2004; Koch et al. 2005). The IGWs in these studies appeared in the region of an upper-level front/jet system. As a result of the relentless increase of numerical resolution used in weather forecasting models, a significant part of sub-synoptic and mesoscale gravity waves can be nowadays resolved. Along with other measures under which conditions they become unstable and eventually break could be used to improve turbulence forecasting. It seems reasonable also to examine synoptic environments in which gravity or inertia-gravity waves, conducive to the generation of CAT occur.

The thesis is organized as follows. In Chapter 2, the synoptic and sub-synoptic environment is explained on the basis of operational analyses provided by the European Centre for Medium-Range Weather Forecasts (ECMWF). These data sets show also the presence of IGWs in the region of CAT encounter. The in-situ data measured during the CAT encounter by a research aircraft will then quantify the properties of the CAT region. A subsequent examination of the dropsonde data suggests the existence of IGWs directly in the region of the CAT. In Chapter 3, results from high-resolution numerical simulations are used to provide further insights into the dynamical structure around the CAT occurrence and possible connections between the IGWs and the CAT. The last chapter contains a diagnostic IGW source analysis using the simulation data. The thesis concludes with a short discussion and an outlook.



## 2 Analysis of the front/jet system

In this chapter, operational T213/L30 ECMWF analyses are applied to characterize the synoptic and sub-synoptic flow patterns before and during the observed CAT event (Section 2.1). In Section 2.2, the in-situ and dropsonde measurements collected by the National Oceanographic and Atmospheric Administration's (NOAA) Gulfstream-IV (G-IV) weather reconnaissance aircraft are presented. The in-situ measurements show evidence of a moderate-or-greater CAT event above the core of the STJ in the region of an equatorward breaking Rossby wave. Furthermore, ECMWF and dropsonde analyses indicate the presence of IGWs.

### 2.1 Evolution of the large-scale flow

Figs. 2.1-2.4 illustrate the 24 hour-period of flow evolution from 29 Jan 1998 00 UTC until Jan 30 1998 00 UTC, i.e. before and during the time of the G-IV flight mission. The displayed section covers a major fraction of the North Pacific Ocean.

On 29 Jan at 00 UTC, an intensifying baroclinic wave was located between the Aleutian and the Hawaiian islands with its center at around  $41^\circ\text{N}$ ,  $168^\circ\text{W}$  (Fig. 2.1). Up to this time, the system has already undergone significant cyclogenesis. It showed the typical appearance of a mid-latitude cyclone with cold air advection to the west and south, and warm air advection to the east of its center in the lower troposphere (Fig. 2.1c). The strong north-south thermal gradient in the lower troposphere to the south-west of the cyclone forced a strong westerly jet flow above (Fig. 2.1a,d).

The distribution of Ertel's potential vorticity (PV) (e.g. Hoskins et al. 1985) on the 310 K isentropic surface (Fig. 2.1a) was similar to the short-wave structure of the geopotential height field  $Z$  at 500 hPa (Fig. 2.1c,d). In the region of the trough, a southward extrusion of stratospheric air (a large positive PV-anomaly<sup>1</sup>) constitutes an equatorward breaking Rossby wave of type "LC2" (Thorncroft et al. 1993) wrapping itself up cyclonically (Fig. 2.1a). In contrast, on the 340 K isentropic surface, the STJ with horizontal velocities  $v_h$  of more than  $90 \text{ ms}^{-1}$  was nearly zonally oriented (Fig. 2.1b).

On the anticyclonic shear side of the jet stream at around  $180^\circ\text{W}$ , negative PV values indicate an inertially unstable region. As the breaking of the baroclinic wave continued, the high stratospheric PV values evolved in a V-like shape with large gradients along the western side at 310 K, see the diagnostics at 12 UTC on 29 Jan in Fig. 2.2. The PV and

---

<sup>1</sup>A positive PV-anomaly means high values of PV relative to other values of PV on the same isentropic surface and at the same latitude.

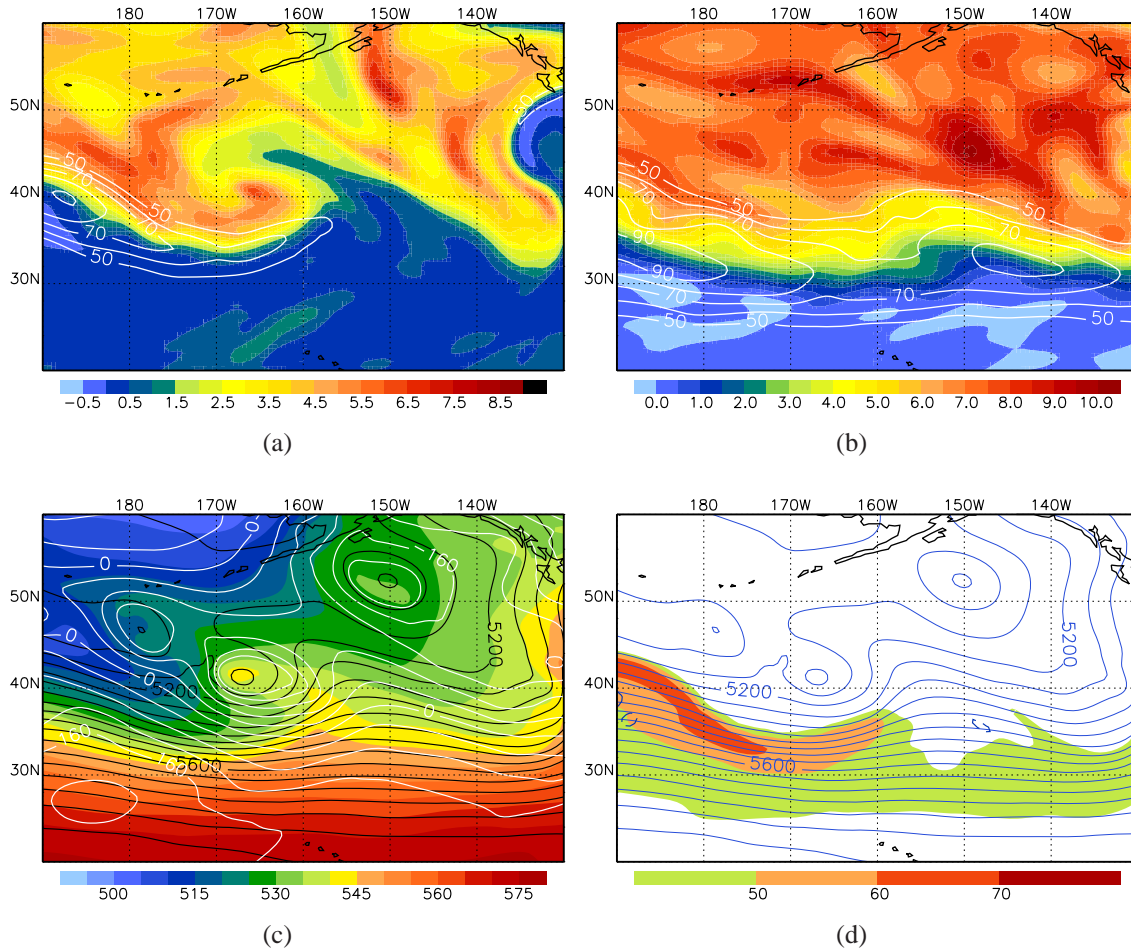


**Figure 2.1:** ECMWF analysis data from 29 Jan 1998 at 00 UTC. PV (PVU which is equal to  $10^{-6} m^2 s^{-1} K kg^{-1}$ , shaded) and horizontal wind  $v_h > 50 \text{ ms}^{-1}$  ( $\text{ms}^{-1}$ , white contour lines,  $\Delta v_h = 10 \text{ ms}^{-1}$ ) on two middleworld isentropes at 310 K (a) and 340 K (b), respectively. Thickness of the 1000-500 hPa layer (dam, shaded) and geopotential height  $Z$  at 1000 hPa (m, white contour lines,  $\Delta Z = 40 \text{ m}$ ) and at 500 hPa (m, black contour lines,  $\Delta Z = 50 \text{ m}$ ) in panel (c). Horizontal velocity divergence  $\nabla_h \cdot \mathbf{v}_h$  at 100 hPa (blue solid contour lines positive, dashed contour lines negative values with the following levels:  $\pm 5, \pm 10, \pm 15, \dots, 10^{-5} \text{ s}^{-1}$ ),  $v_h > 50 \text{ ms}^{-1}$  ( $\text{ms}^{-1}$ , shaded) and  $Z$  (m, blue contour lines,  $\Delta Z = 50 \text{ m}$ ) at the 500 hPa pressure level in panel (d). The domain covers a large part of the Pacific Ocean including the Aleutian and Hawaiian islands.

$\theta$  gradients are associated with an intense jet flow along that edge (Fig. 2.2a). This northwesterly mid-tropospheric jet (MTJ)<sup>2</sup> exhibited horizontal windspeeds  $v_h$  of more than

<sup>2</sup>Here, MTJ stands for a secondary isolated velocity maximum or a downward reaching tongue of high velocity below the core of the STJ, see Fig. 2.5 and Fig. 2.7.

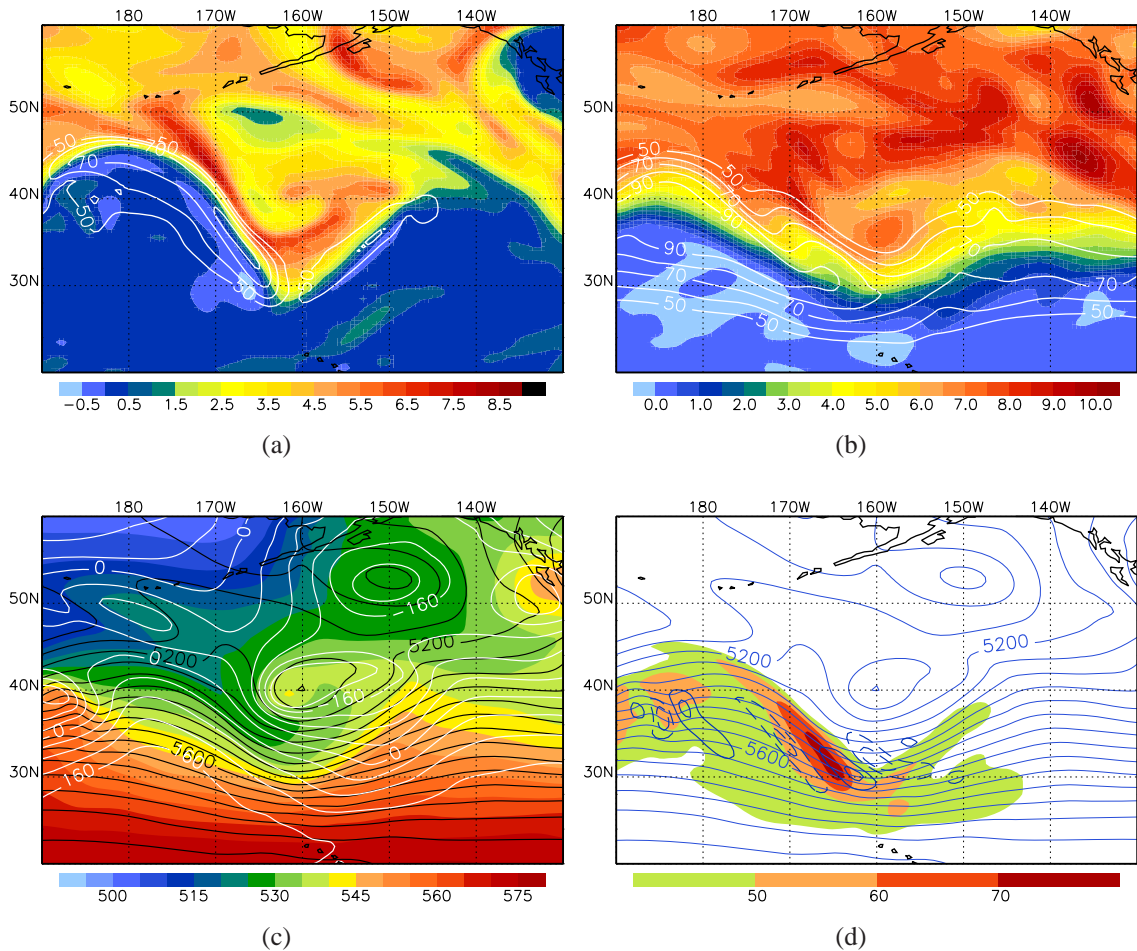


**Figure 2.2:** As in Fig. 2.1 but for 12 UTC on 29 Jan 1998.

$80 \text{ ms}^{-1}$  at 310 K.

PV is conserved for adiabatic, frictionless flows. Air parcels then follow material lines of PV on isentropic surfaces (e.g. Hoskins et al. 1985; Holton 1992). Thus, a region of strong cyclonic curvature and centrifugal accelerations of the air parcels around the southern tip of the V-shaped PV pattern is indicated. On the eastern edge of this pattern, a south-westerly jet with a velocity maximum of  $60 \text{ ms}^{-1}$  was present. Lower (i.e. sub-geostrophic) windspeeds at the base of the trough were likely associated with an opposing inertial-advective ageostrophic wind component due to the cyclonic curvature (e.g. Keyser and Shapiro 1986). Lower windspeeds at the base of the trough led to notable flow deceleration upstream and retarded the north-westerly jetstreak to make it around the base.

The 1000-500 hPa thickness (Fig. 2.2c) shows a narrowing of the cold air tongue to the south-west of the cyclone from 00 to 12 UTC. This might be the result of the baroclinic evolution (i.e. growing amplitude of the baroclinic wave and the southward excursion of the trough) itself or due to a ridge that formed upstream. The enhancement of the

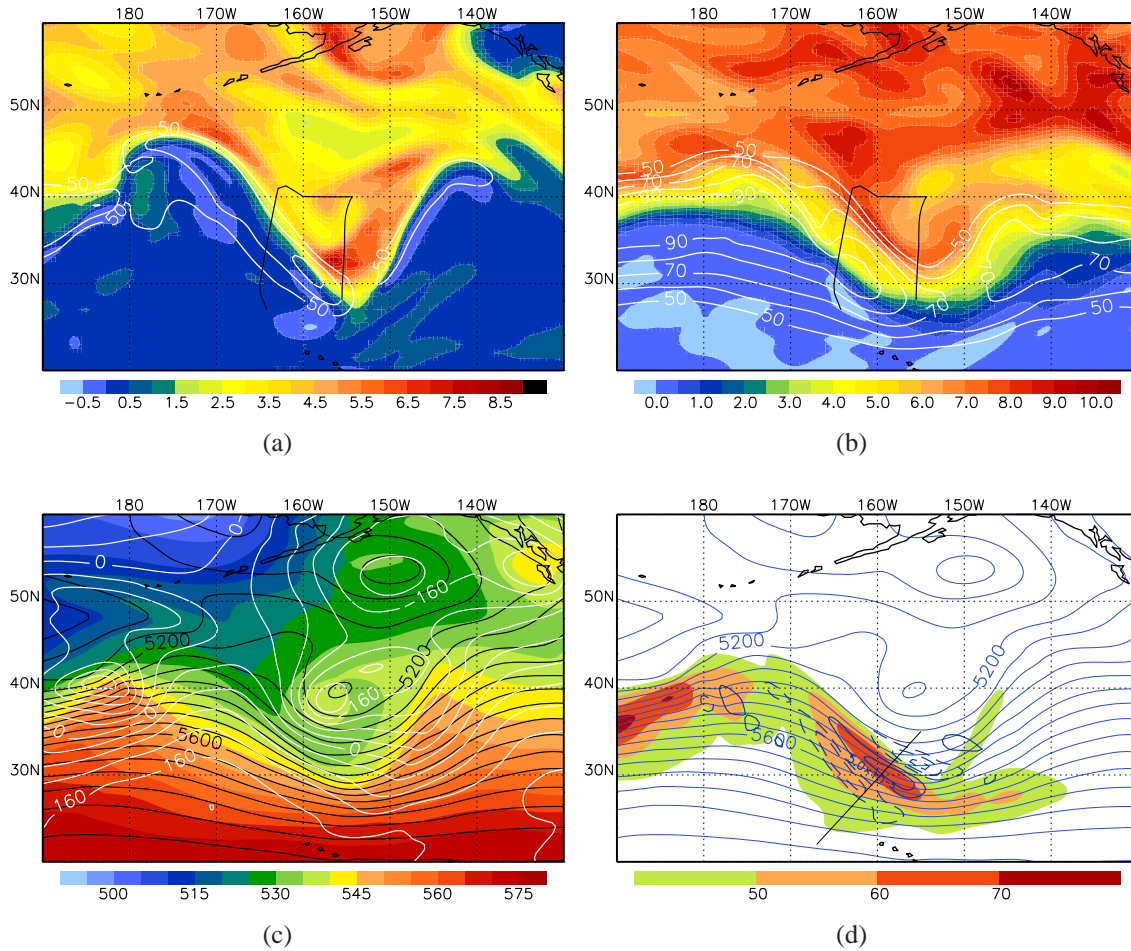


**Figure 2.3:** As in Fig. 2.1 but for 18 UTC on 29 Jan 1998. Additionally, the NOAA’s G-IV flight track is displayed in panels (a) and (b) (thick black line). The flight was performed in an anti-clockwise direction at a pressure level of  $\approx 175$  hPa or a geometric height of  $\approx 12.6$  km between 2100 UTC 29 Jan and 0159 UTC 30 Jan 1998. The potential temperature  $\theta$  at flight level was always greater than 350 K.

baroclinicity at low- to mid-tropospheric levels and the associated development of the very strong north-westerly MTJ (more than  $70 \text{ ms}^{-1}$  on the 500 hPa pressure surface, Fig. 2.2d) was accompanied by the appearance of waves in the lower stratosphere.

The horizontal divergence ( $\nabla_h \cdot \mathbf{v}_h$ ) at 100 hPa showed a packet of waves with one ridge between two troughs directly above the MTJ system (Fig. 2.2d). The horizontal wavelength  $\lambda_h$  of about 600 km was sufficiently large to be resolved by the ECMWF analyses. They constituted an IGW packet with phase lines oriented parallel to the jet axis at 500 hPa (see later). IGW motions are strongly ageostrophic.  $\nabla_h \cdot \mathbf{v}_h$  is thus an ideal parameter to distinguish such motions from the balanced large-scale quasi-geostrophic (or quasi-nondivergent) flow. Finally, this illustration was selected as the appearance of the waves was likely connected with the dynamics of the mid-tropospheric front/jet system. This

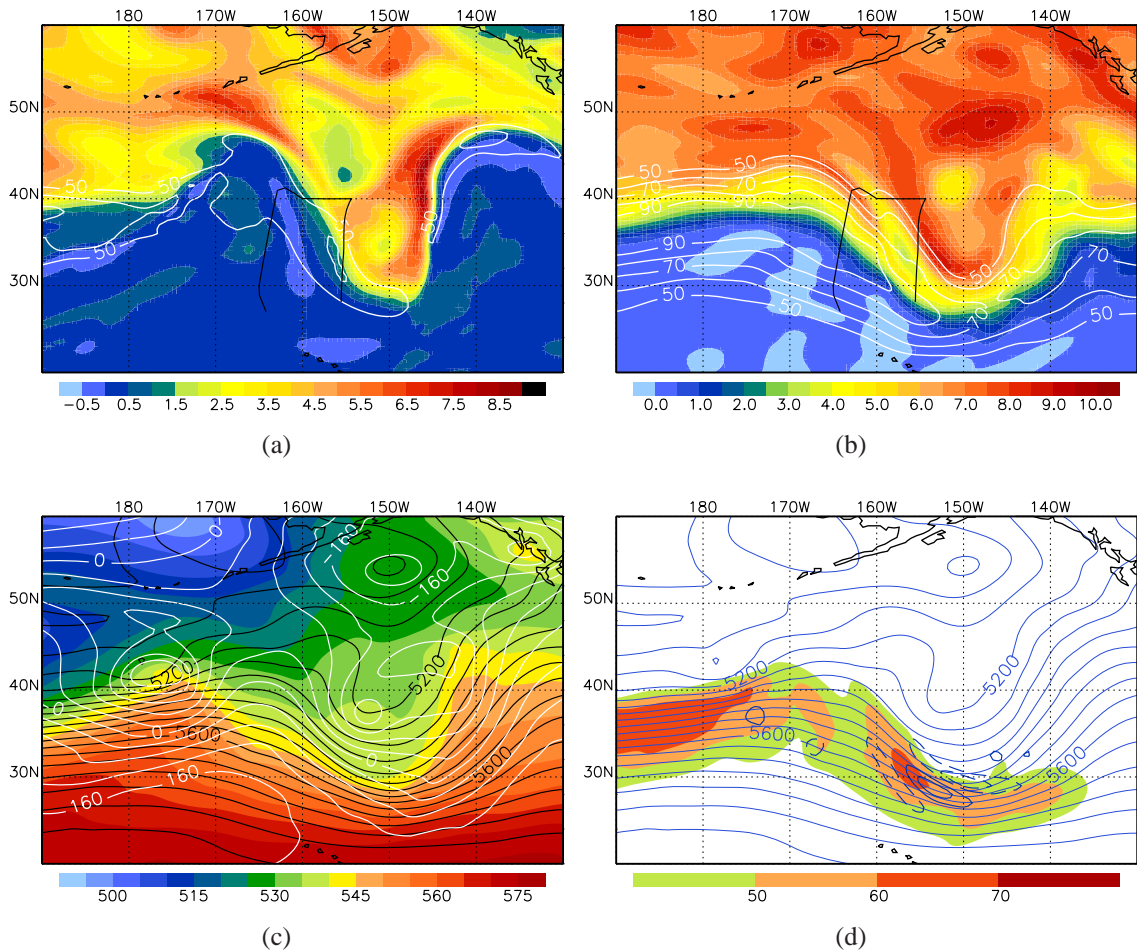


**Figure 2.4:** As in Fig. 2.1 but for 00 UTC on 30 Jan 1998. Additionally, the NOAA’s G-IV flight track is displayed in panels (a) and (b) (thick black line). The flight was performed in an anti-clockwise direction at a pressure level of  $\approx 175$  hPa or a geometric height of  $\approx 12.6$  km between 2100 UTC 29 Jan and 0159 UTC 30 Jan 1998. The potential temperature at flight level was always greater than 350 K.

IGW packet will be called larger-scale inertia-gravity wave (LGW)<sup>3</sup> in the following examination (a smaller-scale inertia-gravity wave (SGW) arises later on also). The LGW is further investigated by use of high-resolution numerical simulations in Chapter 3.

In addition, enhanced values of  $\nabla_h \cdot \mathbf{v}_h$  organized in a wave-like pattern existed upstream above the ridge axis (see Fig. 2.2). This particular synoptic-scale flow configuration, i. e. the diffluent exit region of a jet streak, is known to be a favourable location for the occurrence of mesoscale gravity waves (e.g. Uccellini and Koch 1987; Guest et al.

<sup>3</sup>The scale here refers to the horizontal scale.

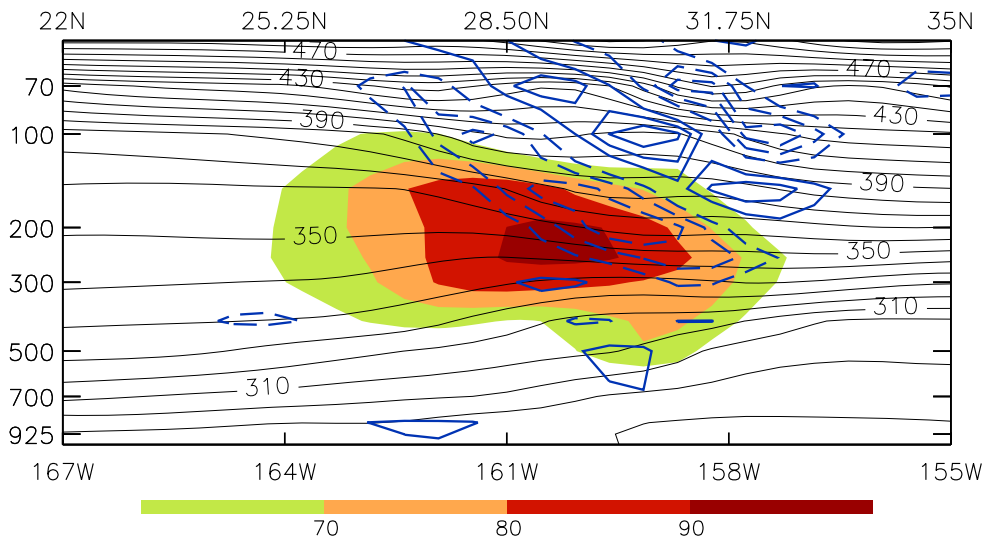


**Figure 2.5:** Vertical cross-section along the black line sketched in Fig. 2.3d at 1800 UTC. Isentropes (K, black contour lines,  $\Delta\theta = 8$  K),  $v_h > 60$   $\text{ms}^{-1}$  ( $\text{ms}^{-1}$ , shaded) and  $\nabla_h \cdot \mathbf{v}_h$  (blue solid contour lines positive, dashed contour lines negative values with levels of  $\pm 3, \pm 6, \pm 9, \dots, 10^{-5} \text{s}^{-1}$ ).

2000; Zhang 2004).

Until 18 UTC (Fig. 2.3), the phase lines of the LGWs relative to the MTJ axis kept their orientation despite the jet axis turned a few degrees during the baroclinic evolution of the breaking Rossby wave. The isotach maximum at 500 hPa decreased about  $10 \text{ms}^{-1}$ .

The initially nearly zonally-oriented STJ (Fig. 2.1b) experienced a strong meridional distortion (Fig. 2.3b) due to the baroclinic development underneath. The jet stream bent equatorward and attained a significant meridional wind component. The width of STJ narrowed at the trough axis and the zonal flow had decreased.

In Fig. 2.5, the vertical cross-section along the black line of Fig. 2.3d at 18 UTC shows the downward reaching tongue of the high wind speeds of the MTJ ( $v_h$  greater than  $60 \text{ms}^{-1}$  below 500 hPa). In the baroclinic zone, the isentropes slope upward towards the colder air located to the north-east in the troposphere. Below the MTJ, and as required by thermal wind balance, they had a greater slope than further to the south at same altitudes. There, the  $60 \text{ms}^{-1}$ -isotach contour line was nearly horizontal and located above 500 hPa. Above the STJ core with  $v_h$  greater than  $90 \text{ms}^{-1}$ , the stratospheric winds strongly decreased resulting in a large negative vertical shear. It should be noted here, that the STJ is typically associated with only a shallow layer of high baroclinicity directly below the jet (Bluestein 1993). In the case considered here, there was high baroclinicity down to lower tropospheric levels (Fig. 2.5) and this resulted in the appearance of the intense MTJ.

The LGW extended vertically from 300 to 50 hPa into the stratosphere (note the different contour increments of  $\nabla_h \cdot \mathbf{v}_h$  in comparison to the horizontal cross-sections, see captions Fig. 2.5 and 2.3). The phase lines (also seen in the isentropic surfaces) sloped upwards to the south-west. A rather large vertical wavelength for an IGW,  $\lambda_z \approx 8$  km,

was estimated as twice the vertical distance from the lowest convergent phase front to the divergent phase above, and  $\lambda_z \approx 6$  km from the divergent phase to the convergent one above. However, one has to take into account the coarse vertical resolution of the operational ECMWF analyses on standard pressure surfaces. A horizontal wavelength between  $\lambda_h \approx 530$  and  $\lambda_h \approx 700$  km was estimated at 100 hPa from Fig. 2.3d.

Towards 00 UTC 30 Jan (Fig. 2.4), the mature cyclone began to weaken. The geopotential heights of 1000 and 500 mb in the region of the core both rose. Also, gradients of the lower tropospheric thermal field (1000-500 mb thickness) weakened (Fig. 2.4c). The positive V-shaped PV-anomaly at 310 K contracted zonally in its northern part (Fig. 2.4a). The amplification of the positive PV-anomaly at 340 K (Fig. 2.4) proceeded till 00 UTC. After 00 UTC 30 Jan, thermal gradients in the baroclinic wave continued to weaken and the LGW packet eventually disappeared.

Forecasts of the described large-scale baroclinic development had stimulated the reconnaissance flight of the NOAA-Gulfstream-IV research aircraft. The flight track is displayed in Figs. 2.3a,b and 2.4a,b (see figure captions for an explanation). The in-situ and dropsonde measurements of this flight are presented in the next section.

## 2.2 Observations

This section presents in-situ and GPS-dropsonde measurements from a research flight of NOAA's G-IV weather reconnaissance aircraft during the North Pacific Experiment 1998 (NORPEX-98). The aircraft base was at Honolulu on the island of Oahu/Hawaii. The objective of NORPEX-98 was to study the impact of additional data collected in a sensitive region over the data sparse Pacific Ocean on the skill of numerical weather prediction. The special emphasis lay on improving forecasts of land-falling winter storms. Altogether, 38 winter storm reconnaissance missions were flown between 14 Jan and 27 Feb 1998 (see Langland et al. 1999).

On the research flight on 29 Jan 1998, moderate-to-severe CAT was encountered by the NOAA G-IV. Measurements were made along the flight track as shown in Figs. 2.3a,b and 2.4a,b. The CAT encounter over the ocean far away from any orography inspired the current study to search for the causes of the flight level turbulence. In the next section, in-situ measurements made during the CAT encounter at flight level ( $\approx 175$  hPa or  $\approx 12.6$  km) are presented. Afterwards, the GPS-dropsonde measurements will be investigated to show the presence of IGWs directly in the region of the CAT.

### 2.2a. In-situ measurements

Fig. 2.6 depicts the in-situ data of the vertical velocity  $w$ , horizontal velocity  $v_h$ , and potential temperature  $\theta$  at the flight altitude during the period from 2100 to 2140 UTC. This selected time sequence corresponds to the first portion of the northbound flight. The aircraft flew at a mean speed of  $197 \text{ ms}^{-1}$  relative to the ground. This gives a flight distance of 473 km in this period. The data presented here were measured with a frequency of 1 Hz,

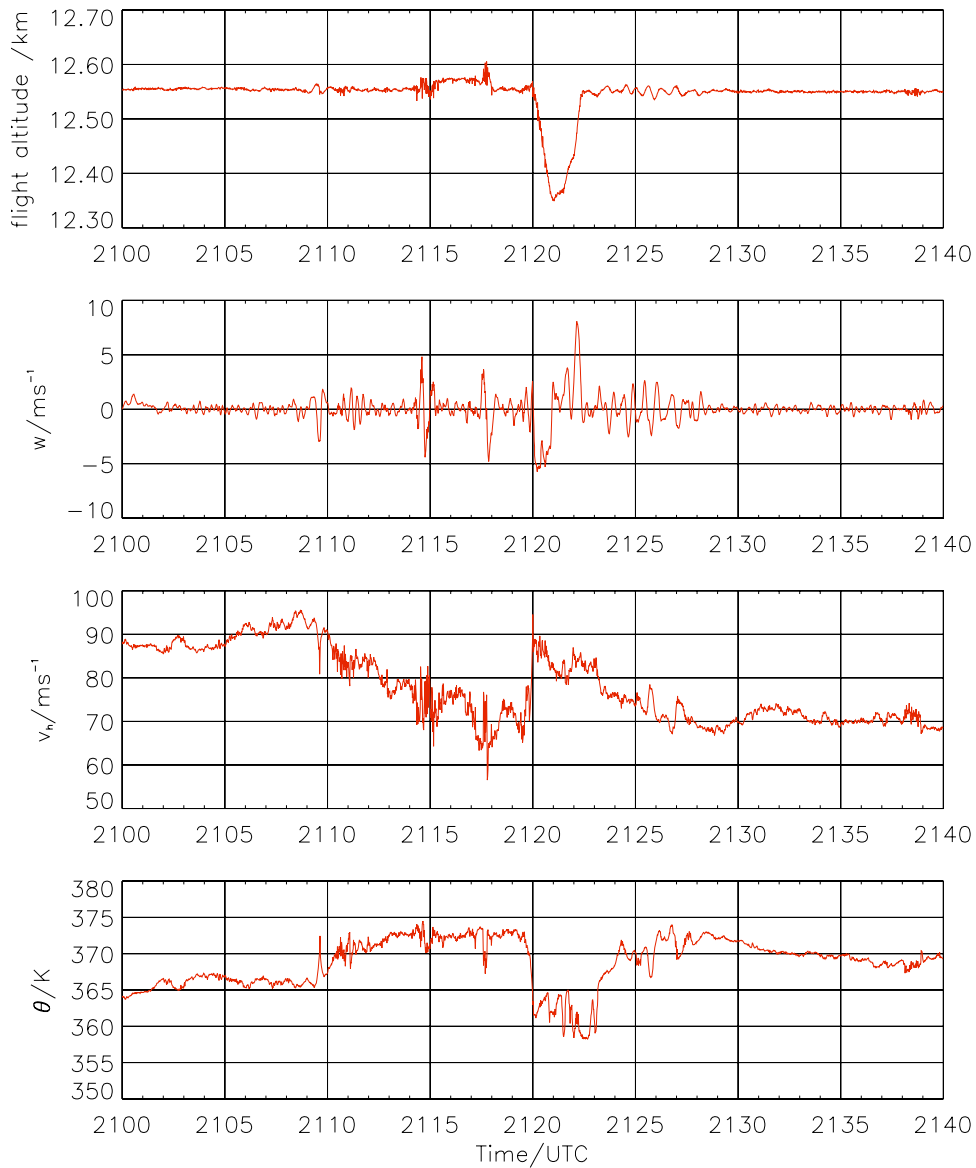


**Figure 2.6:** In-situ measurements from the NOAA G-IV aircraft in the northward flight leg between 2100 and 2140 UTC on 29 Jan 1998. From top panel to bottom panel: flight altitude (km), vertical velocity  $w$  ( $\text{ms}^{-1}$ ), horizontal velocity  $v_h$  ( $\text{ms}^{-1}$ ) and potential temperature  $\theta$  (K). The data were measured with a frequency of 1 Hz.

which provides a resolution on the order of 400 m (according to the Nyquist-frequency important in Fourier analysis). Between 2108 and 2129 UTC, the vertical velocity shows a high variability in comparison to the relatively smooth time lags before and after. Individual peaks of around  $\pm 5 \text{ ms}^{-1}$  were observed and extreme values of  $8.2$  and  $-5.75 \text{ ms}^{-1}$ , respectively, were recorded between 2120 and 2123 UTC. Wave-like oscillations of the vertical velocity with a wavelength around 30 km can be identified in that period.

The flight altitude dropped by about 200 m at around 2120 UTC. As this drop was not an intended flight maneuver it must have been caused by vertical accelerations of the ambient flow experienced by the aircraft. The subsequent ascent was caused by the compensating steering of the auto-pilot.

The aircraft flew above the STJ in a region of negative vertical shear of the horizontal wind vector and in a statically stable environment. Thus, an increase in  $v_h$  and a decrease in  $\theta$  should have been occurred during the fall. Similar variations exist in the measurements. However, by closer inspection of the observations we found that this already happened prior to the sinking of the aircraft:  $v_h$  increased by more than  $20 \text{ ms}^{-1}$  and  $\theta$  decreased by about 5 K in a 30 seconds-interval before 2120 UTC when the flight altitude remained nearly constant. Assuming the conservation of momentum and potential temperature, this can only be explained by an upward transport of potentially colder and higher momentum air from below. This vertical transport was most likely associated with gravity waves. During the period of elevation change, the variations in  $v_h$  and  $\theta$  were small. Furthermore,  $v_h$  did not increase and  $\theta$  did not decrease during the fall and vice versa during the ascent as expected. A turbulent mixing region would be a reasonable explanation of such a signature in the recorded parameters. According to the sensors, vertical accelerations in that flight leg yielded extreme values of  $+4.0, -4.8 \text{ ms}^{-2}$  ( $\sim 0.5 \text{ g's}$ ).

Altogether, all these features show that the G-IV flew through a region of CAT. Its strength according to the measurements can be classified moderate (Lane et al. 2004), but it is not exactly clear whether the sensors produced correct values in this extreme flight situation. An experienced member of the crew reported that the CAT in this flight leg was severe (personal communication, Melvyn Shapiro, NOAA). As a result, it is concluded that the G-IV encountered a region of moderate-to-severe CAT (Koch et al. 2005).

### 2.2b. *Dropsonde analysis*

A vertical cross-section along the northward flight leg shows  $\theta$  and  $v_h$ . This contour plot was produced from the individual asynoptic dropsonde analysed by M. A. Shapiro (Fig. 2.7). Arrows indicate locations where the dropsondes were released at  $\approx 175 \text{ hPa}$ . The flight leg was 1336 km long and the average distance between dropsonde releases amounted to about 110 km. When a GPS-dropsonde is released, it requires a vertical distance of about 700 m until the recording sensors are in equilibrium with the atmospheric environment and delivers reliable measurements (equilibrium level at  $\approx 180\text{-}200 \text{ hPa}$ ).

Significant baroclinicity existed through the entire depth of the troposphere in the right (southern) part of the section. Large baroclinicity, i.e. a large horizontal gradient of  $\theta$ , is generally associated with a proportional vertical change of  $v_h$  in order to satisfy thermal wind balance. This explains the striking intense vertical shear of  $v_h$  along the northward upsloping upper-level front, i.e. the layer of dense isentropes between 800 and 400 hPa. As will be shown later, stratospheric air (e.g., air rich in ozone and PV) intruded downwards (see Fig. 3.2). Such a downward reaching tongue of stratospheric air is called a tropopause fold and develops by differential vertical motions associated with frontogenesis (Danielsen

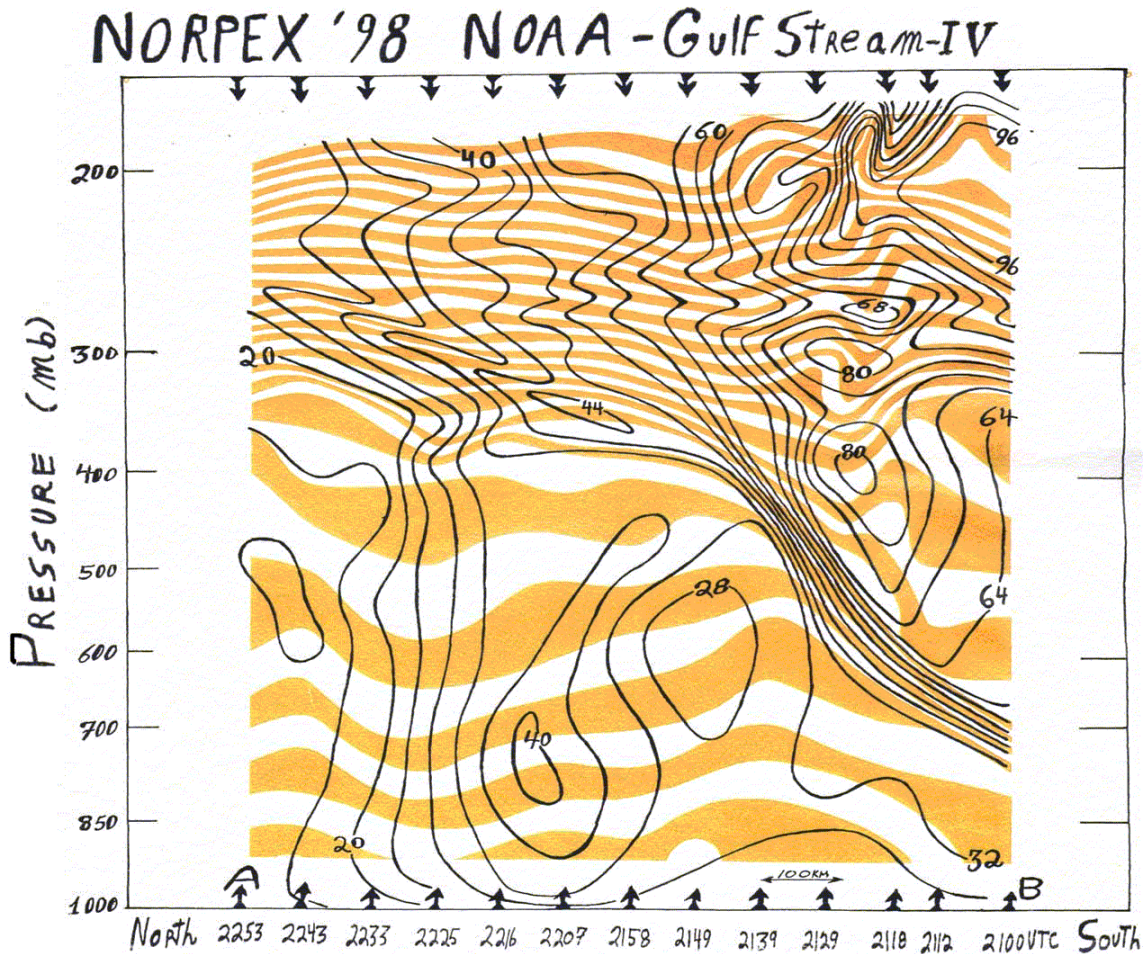


**Figure 2.7:** Dropsonde-derived vertical section along flight track. Isentropes in K (orange-white shaded zebra-like pattern,  $\Delta\theta = 2$  K) and horizontal velocity  $v_h$  ( $\text{ms}^{-1}$ , black contour lines,  $\Delta v_h = 4$   $\text{ms}^{-1}$ ). The arrows at the lower and upper border indicate the release positions of the dropsondes. The time at the lower border show the corresponding release time at flight level ( $\approx 175$  hPa). Courtesy of the figure: M. A. Shapiro, NOAA.

1968; Keyser and Shapiro 1986; Koch et al. 2005). Typically, the air in such a fold has properties between tropospheric and stratospheric air (Shapiro 1980). Tropopause folding is an important mechanism in stratosphere-troposphere exchange (e.g. Sprenger et al. 2003). The strong shear layer together with the isotach maximum of  $80 \text{ ms}^{-1}$  at 400 hPa will be referred to as the mid-tropospheric jet MTJ system, as mentioned earlier. The transition zone from low static stability below (small vertical gradient of  $\theta$ ) to high static stability (large vertical gradient of  $\theta$ ) above between 300 and 400 hPa corresponds with the tropopause.

The region of the G-IV-CAT encounter was located above the core of the STJ ( $v_h^{max} = 94 \text{ ms}^{-1}$ ) at around 200 hPa and extended further to the cyclonic shear side. As can be discerned from Fig. 2.6, it coincided approximately with the dropsonde releases

at 2112, 2118, and 2129 UTC, respectively. Beneath the CAT region, the isentropic surface showed alternating spots of reduced and enhanced static stability down to the mid-tropospheric shear layer. In accordance with these wave-like perturbations, the isotachs were disturbed, too. The appearance of these alternating perturbations resembles a hydrostatic mountain wave pattern (e.g. Gill 1982). Probably, the perturbations above the baroclinic zone and below the CAT region were produced by vertically-propagating gravity waves. A horizontal wavelength along the cross-section from the disturbance of the isentropes was estimated to  $\lambda_h \approx 100\text{-}150\text{ km}$ , a vertical wavelength to  $\lambda_z \approx 3\text{-}4\text{ km}$  and a maximum peak-to-peak amplitude of  $\approx 750\text{ m}$  (around 260 hPa). The interpretation of this cross-section must consider the coarse horizontal resolution between the dropsondes. There existed layered structures in the isotachs and isentropes to the north of jet system in the lower stratosphere around 280 hPa, likely also due to gravity waves. In the next chapter, we seek for arguments to support all these hypotheses by applying high-resolution numerical simulations.

The analysis of a selected dropsonde which was released at 2118 UTC and referred to as dropsonde DS3 is presented next. As can be seen in Fig. 2.7, the dropsonde fell from the CAT region down through the MTJ system and the baroclinic zone with the strong shear values. The upper panel of Fig. 2.8 shows values of potential temperature ( $\theta$ ), horizontal wind components ( $u, v, v_h$ ) and relative humidity (RH). The blue horizontal line denotes the equilibrium level of the dropsonde. The raw dropsonde data were processed with the ASPEN<sup>4</sup> software which removed outliers from the profile and applied a smoothing with a 10 s time window. This corresponds to a vertical distance of 100-200 m depending on the fall velocity (and therefore on the environmental density). The irregularly gridded data with a resolution of 7 to 12 m were interpolated onto a regular grid with vertical intervals of 15 m. Upwards from the blue line, the dropsonde data at the equilibrium level and the flight level data at the release position of the respective dropsonde were linearly interpolated. Vertical profiles of the squared Brunt-Väisälä frequency,

$$N^2 = \frac{g}{\theta} \frac{\partial \theta}{\partial z} \quad (2.1)$$

in which  $g$  is the gravitational acceleration, the vertical shear of the horizontal velocity components squared

$$S^2 = \left( \frac{\partial u}{\partial z} \right)^2 + \left( \frac{\partial v}{\partial z} \right)^2, \quad (2.2)$$

and Richardson number defined as

$$Ri = \frac{N^2}{S^2} \quad (2.3)$$

---

<sup>4</sup><http://www.eol.ucar.edu/rtf/facilities/software/aspn/aspn.html>

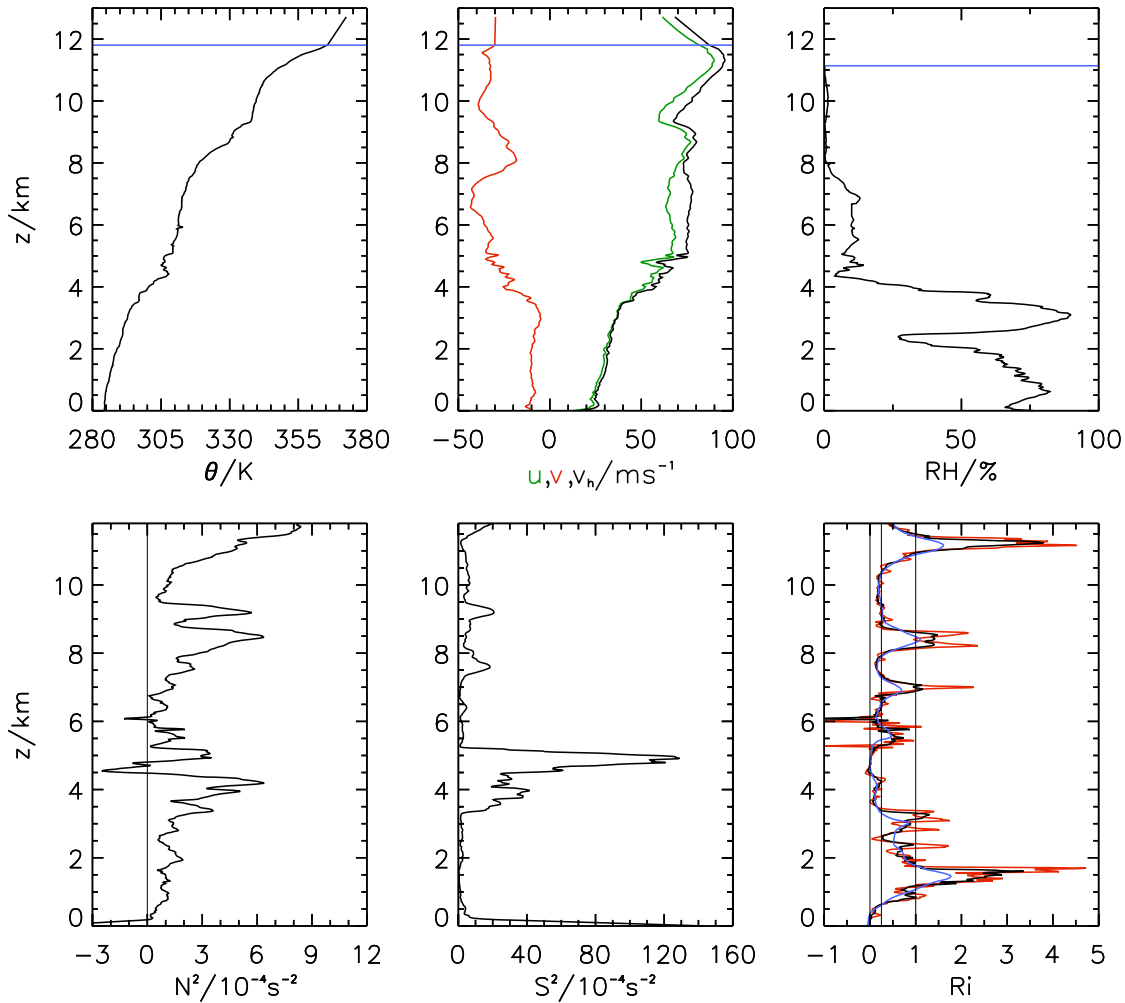


**Figure 2.8:** Vertical profiles of measurements and derived quantities from the dropsonde released at 2118 UTC (dropsonde DS3). Top row from left to right:  $\theta$ , zonal ( $u$ ) and meridional ( $v$ ) wind components (green and red lines) and  $v_h$  (black line), and relative humidity over water  $RH$ , bottom row from left to right: squared Brunt-Väisälä frequency  $N^2$  (see (2.1)), squared vertical shear of horizontal velocity components  $S^2$  (see,(2.2)), and Richardson number  $Ri$  (see (2.3)). See text for a further description.

were calculated from these gridded data. These derived profiles were smoothed by a moving average using a vertical smoothing window of 300 m. Because there is always some arbitrariness in the choice of the filter length, two additional lines of  $Ri$  were drawn, one with a smoothing window of 150 m (red line) and the other with 600 m (blue line), respectively.

The  $\theta$  and  $N^2$  of dropsonde DS3 revealed layers of alternating static stability. A convective boundary layer above the sea surface was followed by an increase of static stability associated with the northward upsloping front (compare Fig. 2.7). Above an altitude

of 4.8 km,  $\theta$  decreased with height resulting in a negative  $N^2$ . This indicates an unstable layer with a depth of roughly 500 m ( $N$  is actually imaginary in this layer). This height range coincided with a layer of strong vertical shear of  $v_h$  below the MTJ system. It is possible that a shearing instability caused turbulence in this layer. However, we cannot verify this hypothesis based on the existing measurements. Nevertheless, and as mentioned in the introduction, if  $Ri < Ri_c$ , what is definitely the case here, the destabilizing vertical windshear is large enough to overcome the stabilizing effect of thermal stratification and the flow becomes turbulent<sup>5</sup>(Miles 1986). Turbulent motions then remain as long as the Richardson number stays below the critical value  $Ri_c$ . It is characteristic for this particular sounding that very low values of  $Ri$  were calculated throughout the entire troposphere. Low values of  $Ri$  indicate the presence of highly nonlinear processes.

Above the strong shear layer, the vertical  $\theta$ -gradient remained small in accordance with small  $v_h$ -changes with increasing altitude up to 8 km. The velocity maximum of  $96 \text{ ms}^{-1}$  at around 11.3 km altitude is associated with the core of the STJ. There is a strong vertical shear of  $0.016 \text{ s}^{-1}$  below and  $-0.025 \text{ s}^{-1}$  above the velocity maximum. The strong negative shear above this jet maximum towards the G-IV flight level is particularly important for a potential explanation of the CAT appearance. An estimate of the bulk Richardson number

$$Ri_B = \frac{(g/\bar{\theta})\Delta\theta\Delta z}{(\Delta v_h)^2}, \quad (2.4)$$

taking differences solely from data at the equilibrium level and the flight level, gives  $Ri_B \approx 0.47$ . Here,  $\bar{\theta}$  was taken as  $\theta$  at the equilibrium level. Therefore, the observations revealed a dynamically unstable layer adjacent to the flight level of the G-IV in the region where the measured vertical velocity fluctuations and the detected vertical accelerations were strongest (c. f. Fig.2.6). This finding suggests that the CAT might have been caused by local instabilities in the negative shear region above the STJ. It must be emphasized that dropsonde DS3 had the most extreme characteristics, i.e. very low values of  $Ri$  throughout the entire profile, in comparison to the other dropsondes. The estimated  $Ri_B$  showed also the lowest values for dropsonde DS3.

Finally, it remains to investigate if the background shear above the STJ alone or if additional processes such as vertically propagating gravity waves might have led to the production of CAT in the dynamically unstable layer. As the dropsonde observations themselves and the ECMWF analyses indicate the presence of gravity waves in this region, high-resolution numerical simulations are used in the next chapter to investigate the gravity wave dynamics and possible interrelationships between the CAT and gravity waves.

---

<sup>5</sup>Again, turbulent means that the flow has small-scale eddies smaller than  $\sim 100\text{m}$ .



## 3 Mesoscale Numerical Simulations

In this chapter, high-resolution numerical simulations serve to investigate the baroclinic development and the associated gravity-wave characteristics. Furthermore, we search for possible dynamical connections between gravity waves and CAT production. Both phenomena were present simultaneously in the region of the G-IV reconnaissance flight (see Section 2.2).

### 3.1 Comparison with ECMWF analyses

The PSU/NCAR mesoscale weather prediction model MM5 (Mesoscale Model, Version 5) in its non-hydrostatic formulation is applied. The model has been used successfully to simulate flows from the synoptic-scale down to the mesoscale including features like developing fronts and gravity waves (e.g. Dudhia 1993; Dörnbrack et al. 1999; Zhang et al. 2000; Zülicke and Peters 2006). Two different model domain configurations were used, each of them was run in a dry and a moist version, respectively. Multiple two-way nesting was applied. The reader is referred to Appendix A for details about the configuration of the different model runs (see Table 3 there).

The simulations with domain configuration R2D and R2M (Table 3 in Appendix A) are found to best approximate the G-IV observations. This can likely be ascribed to the arrangement of the numerical model domains. The outermost domain D1 was positioned to include the trough of the breaking Rossby wave. The innermost domain D3 was aligned to include the region of the G-IV-encountered CAT in its center. Most importantly, the respective simulations incorporated the highest grid resolutions of all performed simulations. Most of the following analysis is based on their results.

Figs. 3.1 and 3.2 are drawn in the same style as the respective figures of the ECMWF analyses (Figs. 2.3 and 2.5). The entire outer domain D1 is shown, which covers a large part of the developing baroclinic wave. The geopotential heights of the 500 and 1000 hPa surfaces were about 40 m lower compared to the ECMWF analyses (see Fig. 3.1c). Therefore, the jet at 500 hPa had around  $10 \text{ ms}^{-1}$  higher windspeeds in its core (Fig. 3.1d) and extends the maximum  $v_h$  contour at 310 K further to the north-west (c.f. Fig. 3.1a).

Distinct differences appeared in the divergence of the horizontal velocity at 100 hPa (Fig. 2.3d). In addition to the LGW packet present in the ECMWF analysis, there exist some smaller-scale wave disturbances above the eastern part of the 500 hPa-trough. These resulted from the parameterized moist convection in the lower troposphere.

Fig. 3.2 shows the dynamical tropopause (e.g. Hoskins et al. 1985) with its break from the high subtropical to the low polar altitudes across the jet system and two main folds at around 5 and 9 km altitude. The alignment of the LGW phase lines in both the horizontal cross section at 100 hPa (Fig. 2.3d) as well as in the vertical cross section (Fig. 2.5) were

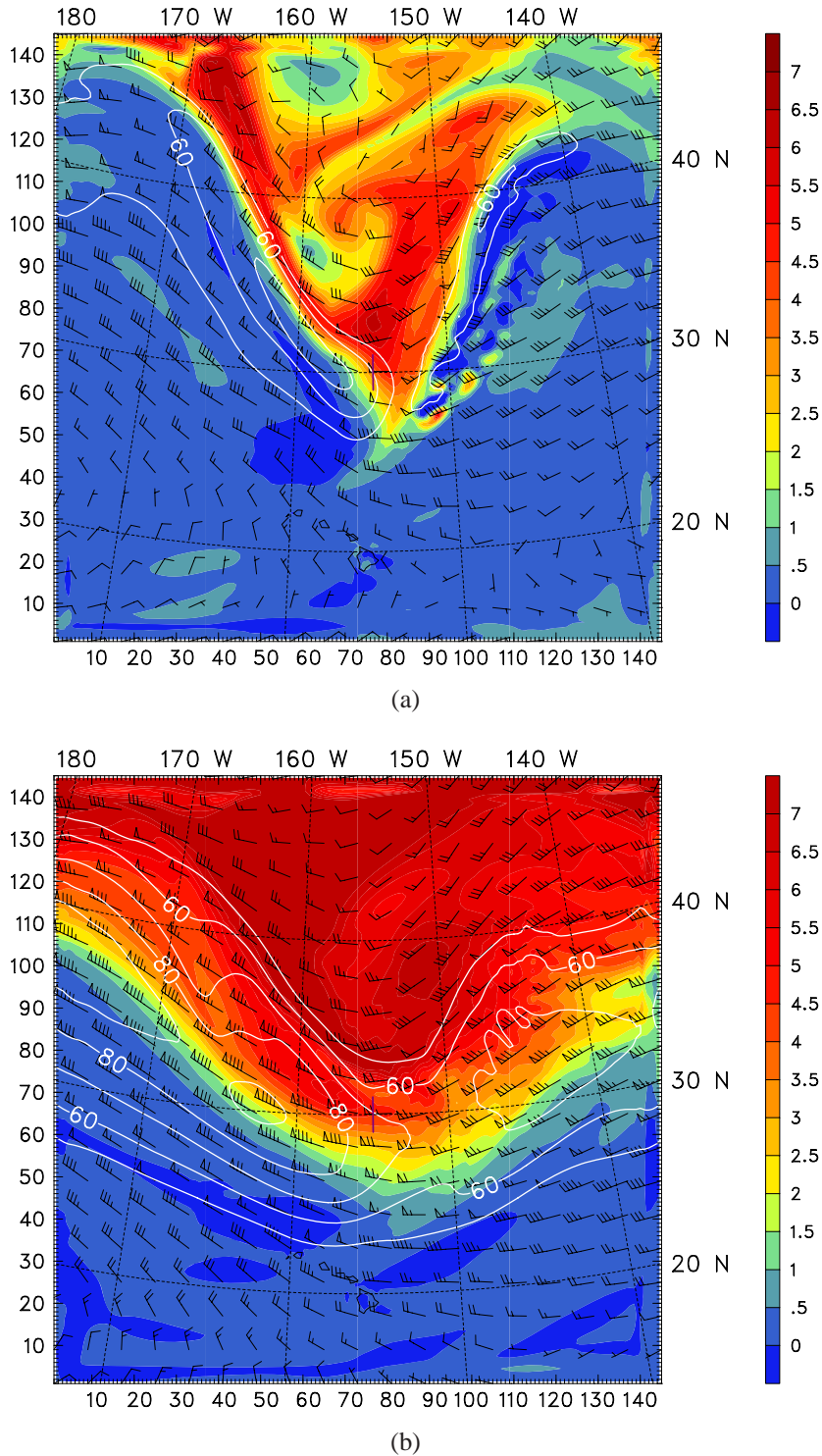
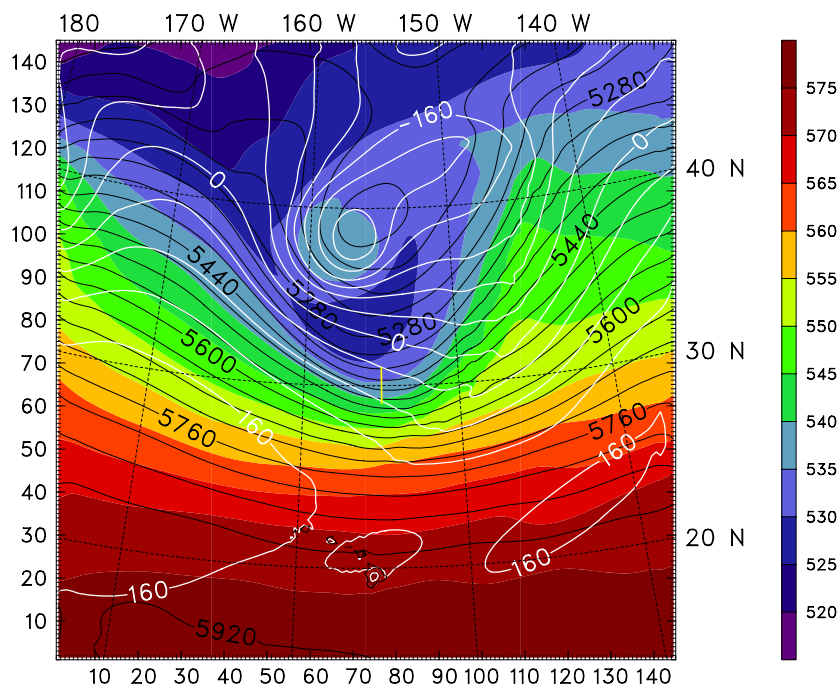
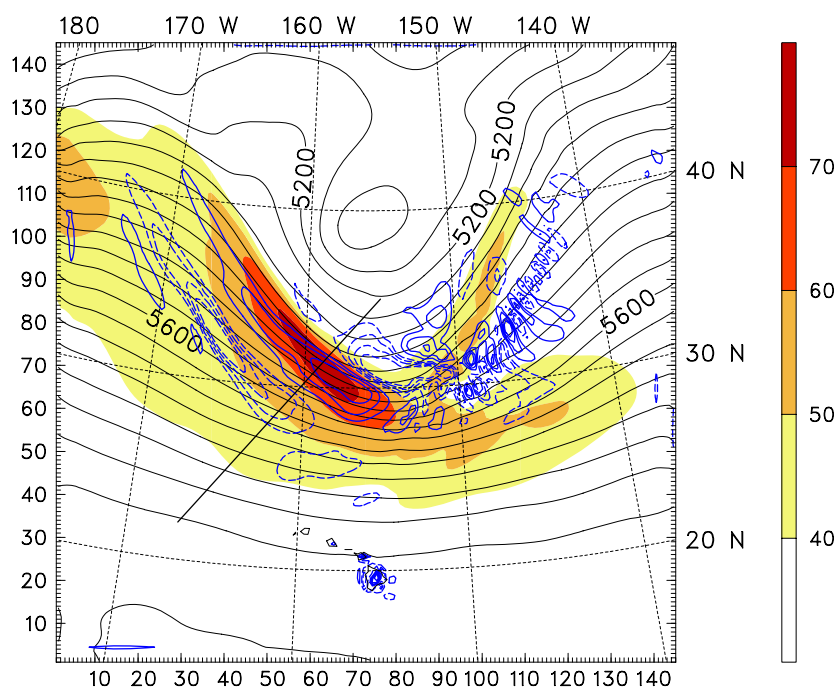


**Figure 3.1:** Data of run R2M D1 from 29 Jan 1998 at 18 UTC. PV (PVU which is equal to  $10^{-6} \text{m}^2 \text{s}^{-1} \text{Kkg}^{-1}$ , shaded) and horizontal wind  $v_h > 50 \text{ ms}^{-1}$  ( $\text{ms}^{-1}$ , white contour lines,  $\Delta v_h = 10 \text{ ms}^{-1}$ ) on two middleworld isentropes at 310 K (a) and 340 K (b), respectively. The domain covers a large part of the Pacific Ocean including the Hawaiian islands. The violet lines in (a), (b) and the yellow in line (c) indicate the flight leg in that the G-IV encountered the CAT at  $\approx 12.6 \text{ km}$  altitude.



(c)



(d)

**Figure 3.1:** (continued) Thickness of the 1000-500 hPa layer (dam, shaded) and geopotential height  $Z$  at 1000 hPa (m, white contour lines,  $\Delta Z = 40$  m) and at 500 hPa (m, black contour lines,  $\Delta Z = 50$  m) in panel (c). Horizontal velocity divergence ( $\nabla_h \cdot v_h$ ) at 100 hPa (blue solid contour lines positive, dashed contour lines negative values with the following levels:  $\pm 5, \pm 10, \pm 15, \dots, 10^{-5} \text{s}^{-1}$ ),  $v_h > 50 \text{ ms}^{-1}$  ( $\text{ms}^{-1}$ , shaded) and  $Z$  (m, black contour lines) at the 500 hPa pressure level in panel (d).

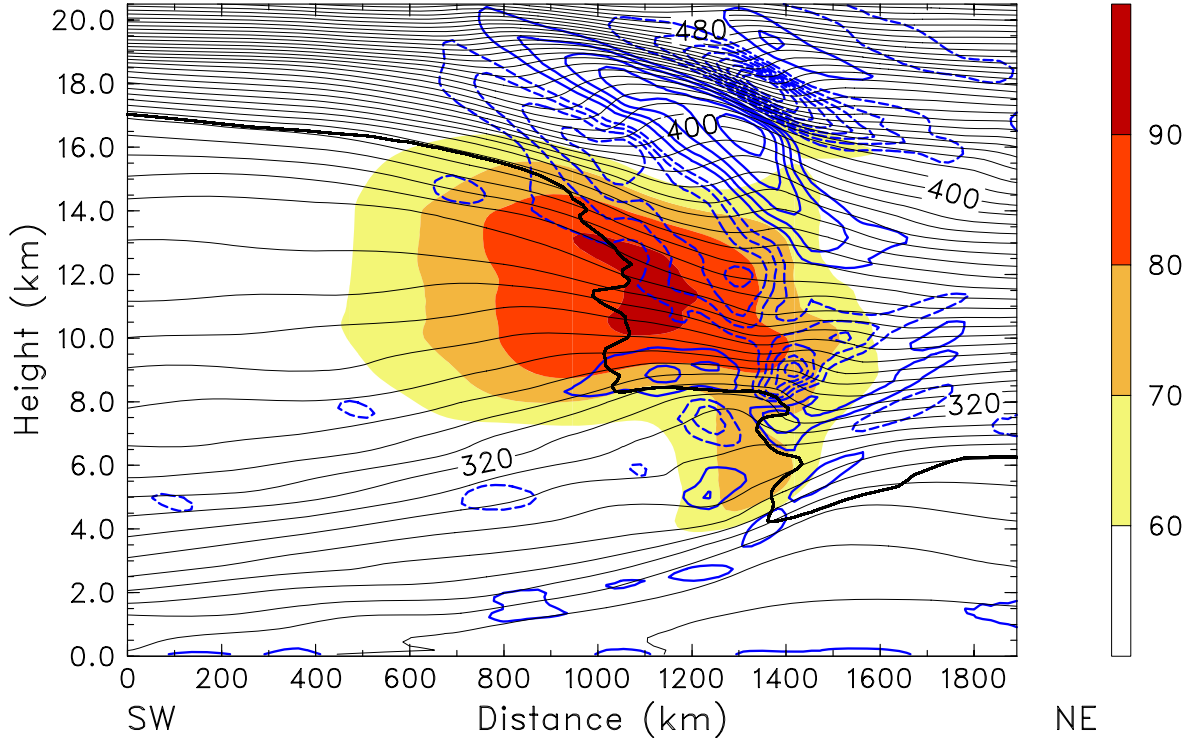


**Figure 3.2:** Data of run R2M D1 from 29 Jan 1998 at 18 UTC. Vertical cross-section along the black line sketched in Fig. 3.1d. Isentropes  $\theta$  (K, black contour lines,  $\Delta\theta = 8$  K),  $v_h > 60 \text{ ms}^{-1}$  ( $\text{ms}^{-1}$ , shaded) and velocity divergence (blue solid contour lines positive, dashed contour lines negative values with levels of  $\pm 3, \pm 6, \pm 9, \dots 10^{-5} \text{ s}^{-1}$ ). Dynamical tropopause (PV=2 PVU, thick black contour line).

similar, but distinct differences appeared in the amplitudes of the waves.

### 3.2 Inertia-gravity wave dynamics

The gravity wave amplitudes are much larger in the MM5 simulations. The convergence (negative divergence) contours in the vertical cross-section at around 18 km altitude reach an impressive maximum magnitude  $|\nabla_h \cdot \mathbf{v}_h|_{max} = 2.4 \cdot 10^{-4} \text{ s}^{-1}$  compared to  $|\nabla_h \cdot \mathbf{v}_h|_{max} = 9.0 \cdot 10^{-5} \text{ s}^{-1}$  in the ECMWF analyses. The peak-to-peak displacement of the 416-K isentrope, which intersected the LGW packet, was about 800 m (see Fig. 3.2). The simulations gave also a maximum vertical velocity  $|w|_{max} = 21 \text{ cms}^{-1}$  associated with the LGW (not shown).  $|\nabla_h \cdot \mathbf{v}_h|_{max}$  and  $|w|_{max}$  were taken as the maximum contour magnitude. The maximum amplitudes occurred directly above the MTJ system (e.g. Fig. 3.2).

Table 1 compares the LGW amplitudes along with horizontal and vertical wavelengths  $\lambda_h$  and  $\lambda_z$ , respectively. The subjectively estimated averages  $\lambda_h$  and  $\lambda_z$  are taken from the

Run	Domain	$\lambda_h(km)$	$\lambda_z(km)$	$ \nabla_h \cdot \mathbf{v}_h _{max}(10^{-4}s^{-1})$
R1M	1	550	5.6	1.8
R1M	2	528	5.5	2.4
R2M	1	526	5.3	2.4
R2M	2	535	5.2	2.4
R2D	1	553	5.3	1.5
R2D	2	540	4.5	2.4
ECMWF		650	6.5	0.9

**Table 1:** Derived quantities of the LGWs above the front/jet system for different runs and domains of the mesoscale simulations and the ECMWF analysis data at 18 UTC on 29 Jan 1998.  $\lambda_h$  and  $\lambda_z$  are estimated average horizontal and vertical wavelengths. The values of  $|\nabla_h \cdot \mathbf{v}_h|_{max}$  display the maximum horizontal divergence magnitude in association with the LGW.

same horizontal- (equal to that of Fig. 3.1d or 2.3d) and vertical cross-sections (equal to that of Fig. 3.2 or 2.5) of the different simulations. Local values of the derived quantities along the LGW packet can vary significantly with geographical location and altitude. In order to obtain an objective analysis, fixed positions relative to the LGW packet were taken to estimate these quantities. The quantity  $\lambda_h$  of the essentially three-phase LGW packet was determined with the following procedure: mean distances between the individual  $|\nabla_h \cdot \mathbf{v}_h|$  phase fronts at 100 hPa were measured manually out from the figures (convergent-divergent and divergent-convergent). The sum of this two values was taken to be  $\lambda_h$ . The same method was applied to obtain  $\lambda_z$  in the vertical cross-sections.

The average  $\lambda_h$ ,  $\lambda_z$  and  $|\nabla_h \cdot \mathbf{v}_h|_{max}$  of the different simulations listed in Table 1 are  $\bar{\lambda}_h = 539$  km,  $\bar{\lambda}_z = 5.2$  km and  $|\nabla_h \cdot \mathbf{v}_h|_{max} = 2.15 \cdot 10^{-4} s^{-1}$ . The quantities  $\bar{\lambda}_h$  and  $\bar{\lambda}_z$  are therefore about 17 % and 20 % smaller,  $|\nabla_h \cdot \mathbf{v}_h|_{max}$  is 139 % greater than the respective ECMWF values. The large  $\lambda_z$  of the ECMWF data might be caused by the coarse vertical resolution of the standard pressure surfaces. Numerical resolutions might be responsible also for the large differences in the divergence maxima.

The  $\lambda_h$  and  $\lambda_z$  estimates from the simulations differ by up to 3% and 14% from  $\bar{\lambda}_h$  and  $\bar{\lambda}_z$ , whereby the smallest value  $\lambda_z = 4.5$  km was estimated in domain D2 of run R2D. This value is about 14% smaller than the corresponding value from the moist run (R2M D2). Except for R2M, the  $|\nabla_h \cdot \mathbf{v}_h|_{max}$ -values basically show greater values with higher numerical resolution (Table 1). R2D D1 had the largest deviation of 30 % from  $|\nabla_h \cdot \mathbf{v}_h|_{max}$ . Altogether, the simulations are in close agreement despite the different numerical configurations. However, the estimates of  $\lambda_z$  resulted in rather large values for inertia-gravity waves with an intrinsic frequency  $\hat{\omega} \sim 2.9f$  (see below). In the following subsection, we determine the characteristics of the LGWs using run R2M.

It is important to note that the IGW amplitudes in our simulations were greater than in other idealized (e.g. O’Sullivan and Dunkerton 1995; Zhang 2004) and real-case (e.g. Plougonven et al. 2003; Lane et al. 2004; Zülicke and Peters 2006) studies of IGWs in association with baroclinic waves.

### 3.2a. LGW discussion

The entire LGW packet propagated in the WSW-direction ( $\phi \approx 100^\circ$ ) and the phase propagation is in the NE-direction ( $\phi \approx 45^\circ$ ) with a ground-based horizontal phase velocity of  $c_h \approx 13.5 \text{ ms}^{-1}$  at 15 km altitude. These values were estimated directly from model output in the time range from 15 to 19 UTC. Given,

$$\hat{\omega} = \omega - \bar{\mathbf{v}} \cdot \mathbf{k}_h \quad (3.1)$$

which relates the ground-based frequency  $\omega$  of a wave to the intrinsic frequency  $\hat{\omega}$ . The relation accounts for the Doppler-shift in a moving fluid with mean (background) velocity  $\bar{\mathbf{v}}$  and a phase that propagates in the direction of  $\mathbf{k}_h$  (e.g. Holton 1992; Nappo 2002). One obtains the intrinsic horizontal phase velocity  $\hat{c}_h$  by using,

$$\hat{c}_h = c_h - v_{\parallel} \quad (3.2)$$

in which  $v_{\parallel}$  is the mean (or background) velocity in the direction of the horizontal wavevector  $\mathbf{k}_h$  (note, that  $c_h = \omega/k_h$ ,  $\hat{c}_h = \hat{\omega}/k_h$ ). In doing so, the LGW is treated approximately as a plane wave with phase lines perpendicular to the wave vector  $\mathbf{k}_h$ . Finally, this allows the LGW intrinsic frequency to be determined with the knowledge of the wavelength ( $\lambda_h = 2\pi/k_h$ ), the phase velocity  $c_h$  and the mean velocity in the direction of phase propagation  $v_{\parallel}$ . Using  $c_h \approx 13 \text{ ms}^{-1}$  and  $v_{\parallel} \approx 31 \text{ ms}^{-1}$  leads to  $\hat{c}_h \approx -18 \text{ ms}^{-1}$ . This means, the LGW phase moved against the mean flow. We adopt the convention of a positive definite intrinsic frequency. This leads us to a wavevector  $\mathbf{k}_h$  that points against the mean flow in the direction of phase propagation in accordance with a negative  $\hat{c}_h$ . The intrinsic frequency with  $\lambda_h \approx 526 \text{ km}$  finally becomes  $\hat{\omega} \approx 2.15 \cdot 10^{-4} \text{ s}^{-1}$  and with a local Coriolis parameter  $f(30^\circ) = 7.3 \cdot 10^{-5} \text{ s}^{-1}$ , the intrinsic frequency can be finally determined as  $\hat{\omega} \approx 2.9 f$ .

Fig. 3.3 displays a wind hodograph of deviations ( $u'$ ,  $v'$ ) from mean profiles calculated from a moving average over a window of 4 km vertical distance and plotted in the height range between 17 and 21 km at 18 UTC. Linear theory for a monochromatic inertia-gravity wave reveals that the ratio  $R$  of the minor to the major axis of the perturbation ellipse ( $u'$ ,  $v'$ ) with height can be written as

$$R = \frac{f}{\hat{\omega}} \quad (3.3)$$

(e.g. Thompson 1978; Gill 1982). A value  $R = 0.65$  is estimated from the simulated hodograph leading to  $\hat{\omega} = 1.1 \cdot 10^{-5} \text{ s}^{-1}$ . Applying a modified version of Eq. 3.3 by taking into account the vertical shear of the mean horizontal velocity perpendicular to the horizontal wavevector ( $\bar{v}^\perp$ ) as proposed by Thomas et al. 1999,

$$R = \left| \frac{f}{\hat{\omega}} - \frac{\lambda_z}{\lambda_h \hat{\omega}} \frac{d\bar{v}^\perp}{dz} \right| \quad (3.4)$$

results into an intrinsic frequency of  $\hat{\omega} = 1.9 \cdot 10^{-4} \text{ s}^{-1}$ . This value agrees closely to the frequency estimated before from the Doppler relationship. Here, I used  $\lambda_h = 520 \text{ km}$  given

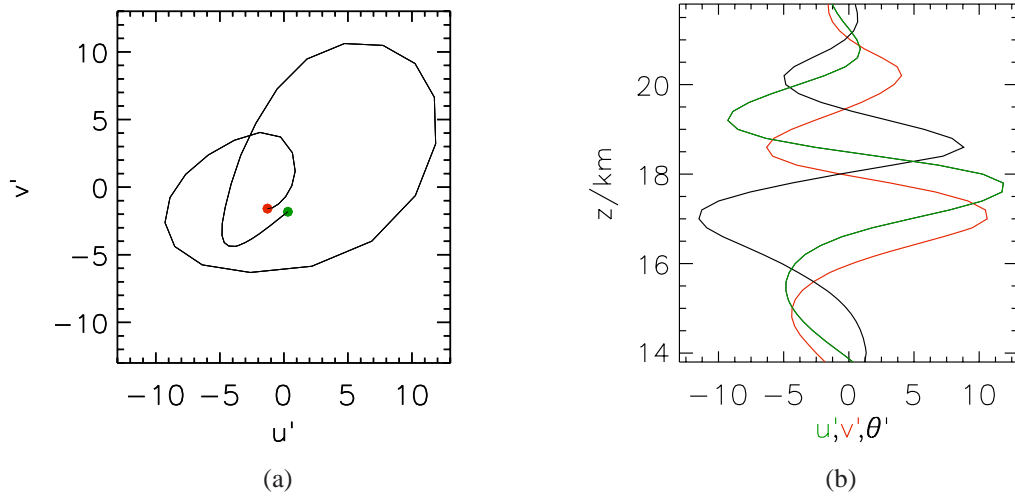


**Figure 3.3:** (a) Hodograph of perturbation horizontal velocity components  $u', v'$  in  $\text{ms}^{-1}$ , (b) a vertical profile of  $u', v'$  and perturbation potential temperature  $\theta'$  in K. Data of run R2M D1 from 29 Jan 1998 at 18 UTC. The profiles are taken from the grid at distance=1300 km in the vertical section of Fig. 3.2 and plotted between 14 and 22 km altitude. The helical hodograph of (a) starts at 14 km (marked by the green dot) and ends at 22 km (red dot). The perturbations were defined as deviations from a mean profile calculated by a moving average with a vertical window of 4 km.

as twice the distance from the divergent to the convergent LGW phase line at 18 km altitude from the vertical cross-section, Fig. 3.2. The vertical wavelength  $\lambda_z = 3.75$  km was estimated from the hodograph as the average in the height range between 14 and 22 km, whereas  $\bar{S}_\perp = d\bar{v}_\perp/dz = -7.0 \cdot 10^{-3} \text{ s}^{-1}$  was determined from the smoothed  $v^\perp$ -profile.

As discussed by Zhang et al. 2004, the determination of the intrinsic frequency by a single hodograph – even if the wave packet can be reasonably described by linear theory – is inaccurate for two reasons. First of all, the modulation of the gravity wave packet in the direction of propagation can be important due to the spatially varying ambient state. In the present case, the LGW packet is subject to a large variation of basic IGW quantities, for example horizontal and vertical wavelengths (see Figs. 3.1d and 3.2). Secondly, there always exists some arbitrariness in the choice of the filter. However, the calculated intrinsic frequency changed to  $\hat{\omega} = 2.0 \cdot 10^{-4} \text{ s}^{-1}$  and  $\hat{\omega} = 2.2 \cdot 10^{-4} \text{ s}^{-1}$  by altering the filter length to 3 and 5 km, respectively. Therefore, the influence of the smoothing window does not cause large errors for this hodograph. A sensitivity test done for the whole set of the different mesoscale simulations as presented in Table 1 never exceeded deviations of  $\hat{\omega}$  greater than  $\Delta\hat{\omega} = \pm 0.3 \cdot 10^{-4} \text{ s}^{-1}$  from  $\hat{\omega} = 1.9 \cdot 10^{-4} \text{ s}^{-1}$ .

It is worth pointing out that the estimated LGW parameters were fairly constant from the begin of wave emission around 03 UTC until around 18 UTC; afterwards, they changed significantly in association with the rapidly evolving large-scale flow (see next section). The perturbation velocity components ( $u', v'$ ) clearly show an anticyclonic rotation with height. This implies an upward propagation of the LGW packet above the jet system in

the lower stratosphere (e.g. Thompson 1978; Thomas et al. 1999). Eventually, this means that the energy source of the wave must be located below 14 km altitude. Many simulated hodographs in the region of the jet system were tested and altogether they showed this behaviour (albeit they indicated varying frequencies and slightly different phase propagation directions).

Fig. 3.2 shows a shortening of the vertical wavelength with altitude above the jet system. This is because the wave encounters a critical level  $z_c$  due to the decreasing horizontal wind speed. A monochromatic gravity wave has a critical level where the mean flow velocity in the direction of the wavevector equals the phase velocity (e.g. Booker and Bretherton 1967; Nappo 2002). As an internal gravity wave propagates towards its critical level it experiences a growth in amplitude of the horizontal velocity and a reduction of the vertical velocity. This is accompanied with an increase of the vertical wavenumber or a shortening of the vertical wavelength (e.g. Nappo 2002). The simulated gravity waves show these properties, see Figs. 3.2 and 3.3. Particularly, Fig. 3.2 shows evidently the more horizontal alignment of the phase lines of the wave and a decrease of their vertical distance with increasing altitude. This creates a permanent growth of the vertical shear of the horizontal velocity as the wave packet approaches the critical level. Eventually, growing vertical shear often leads to a breakdown of the wave via shearing instability before it reaches  $z_c$  (Nappo 2002).

By including wave stress into the discussion, linear inviscid theory shows a reduction of the wave stress by an amount  $\exp(-2\pi\sqrt{Ri_c - 0.25})$  (Booker and Bretherton 1967), where  $Ri_c > 0.25$  is the Richardson number at the critical level (the greater  $Ri_c$  the stronger the attenuation, but an already low  $Ri_c$  leads to an easier breakdown of the wave), while passing through the critical level. Therefore, the deposition of wave pseudo-momentum below the critical level and the associated acceleration of the mean flow (wave-mean flow interaction) leads to strong vertical shear of the mean horizontal velocity. Linear inviscid theory shows also that the wave stress is constant unless the wave is dissipated (Eliassen and Palm 1960). Critical levels are therefore provide regions of wave dissipation and impede gravity waves from propagating further upwards (see Dörnbrack 1998).

In three-dimensional flows, critical levels can result from linear vertical shear, directional vertical shear of the mean flow, or by a turning of the wave vector while propagating upwards (e.g. Shutts 1995; Moldovan et al. 2002). Mathematically, in linear gravity wave theory, a critical level results from a singular point in the differential equations describing the wave motion (i.e., the Taylor-Goldstein equation). A classical critical level exists where the intrinsic frequency is zero ( $\hat{\omega} = 0$ ). This is valid for high and medium frequency waves. For a low-frequency gravity wave ( $\hat{\omega} \sim f$ ) two additional singular points exist at  $\hat{\omega} = \pm f$  (e.g. Moldovan et al. 2002). These are called inertial critical levels (ICLs). As we are studying such low-frequency waves in this thesis, the difference in altitude between the both types of critical levels is important.

Around 18 UTC, the lowest critical level, an ICL in the  $(-f)$ -branch for the LGW lies at an altitude of  $\approx 19$  km. Although this value is not valid everywhere along the

LGW packet, it gives a qualitative explanation why the upward propagating LGW packet dissipates (actually, it is absorbed by the model's explicit and numerical diffusion) between 18 and 20 km altitude and no distinct wave signal is present above 20 km.

### 3.2b. *Smaller-scale wave emission*

From their first appearance until around 18 UTC, the upper tropospheric, lower stratospheric LGW packet with phase lines aligned with the mean wind showed relatively regular characteristics. Subsequently, the patterns and characteristics of the simulated gravity waves changed dramatically until about 22 UTC. This evolution was associated with the strong zonal contraction of the front over an 8-hour period until around the time of the G-IV CAT-encounter: see the thermal structure (isentropes) at 4 km altitude in Fig. 3.4. Most striking, the simulated scale-contraction was strongest directly beneath the flight segment where CAT was encountered (see the violet line in Fig. 3.4), and occurred at the same time as the G-IV flew through that leg between 2109 and 2129 UTC. It is most likely that rapid frontogenesis and the related contraction of the isentropes was caused by the ridge that built upstream.

Simultaneously, the scale-contraction of the rapid frontogenesis in the troposphere was associated with an upper-level instability. From 18 UTC (Fig. 3.5a) to 23 UTC (Fig. 3.5b), the potential temperature perturbations and the vertical velocity at 13 km altitude became amplified to the north-east of the upper-level front which divided colder air to the southwest from warmer to the north-east. Fig. 3.5 does not show the full domain D2: note the grid numbers of the axes and the specification in Table 3 in Appendix A.

A vertical cross-section along the black west-to-east line in Fig. 3.5 illustrates the connection between the strong intensity of the upper-level front and the LGW oscillations, see Fig. 3.6. This can be readily seen by the large wave-induced displacements of the isentropes in the vertical section at 13 km altitude. Again,  $\nabla_h \cdot \mathbf{v}_h$  was used to emphasize the IGW oscillations in Fig. 3.6 and Fig. 3.7. The latter section is plotted along the southwest-to-northeast line drawn in Fig. 3.5.

In both figures, the  $\nabla_h \cdot \mathbf{v}_h$ -pattern altered dramatically from 18 to 23 UTC (Figs. 3.6 and 3.7). Associated with the strong frontogenesis during that time period, the LGW packet contracted horizontally as well, especially in the zonal direction, see Fig. 3.6. The LGW had  $|\nabla_h \cdot \mathbf{v}_h|_{max} = 2.4 \cdot 10^{-4} s^{-1}$  at 18 and 23 UTC, but  $|w|_{max} = 24 \text{ cms}^{-1}$  at 18 UTC and  $|w|_{max} = 33 \text{ cms}^{-1}$  at 23 UTC (not shown).

At 23 UTC, another wave signal characterized by a higher aspect ratio ( $\lambda_z/\lambda_h$ ) than the LGW, appeared above the region of the MTJ system (see  $\nabla_h \cdot \mathbf{v}_h$  and  $\theta$  in Figs. 3.6b and 3.7b). The peak-to-peak displacement of the 368-K isentrope due to this smaller-scale <sup>1</sup>

---

<sup>1</sup>Again, the scale refers to the horizontal scale.

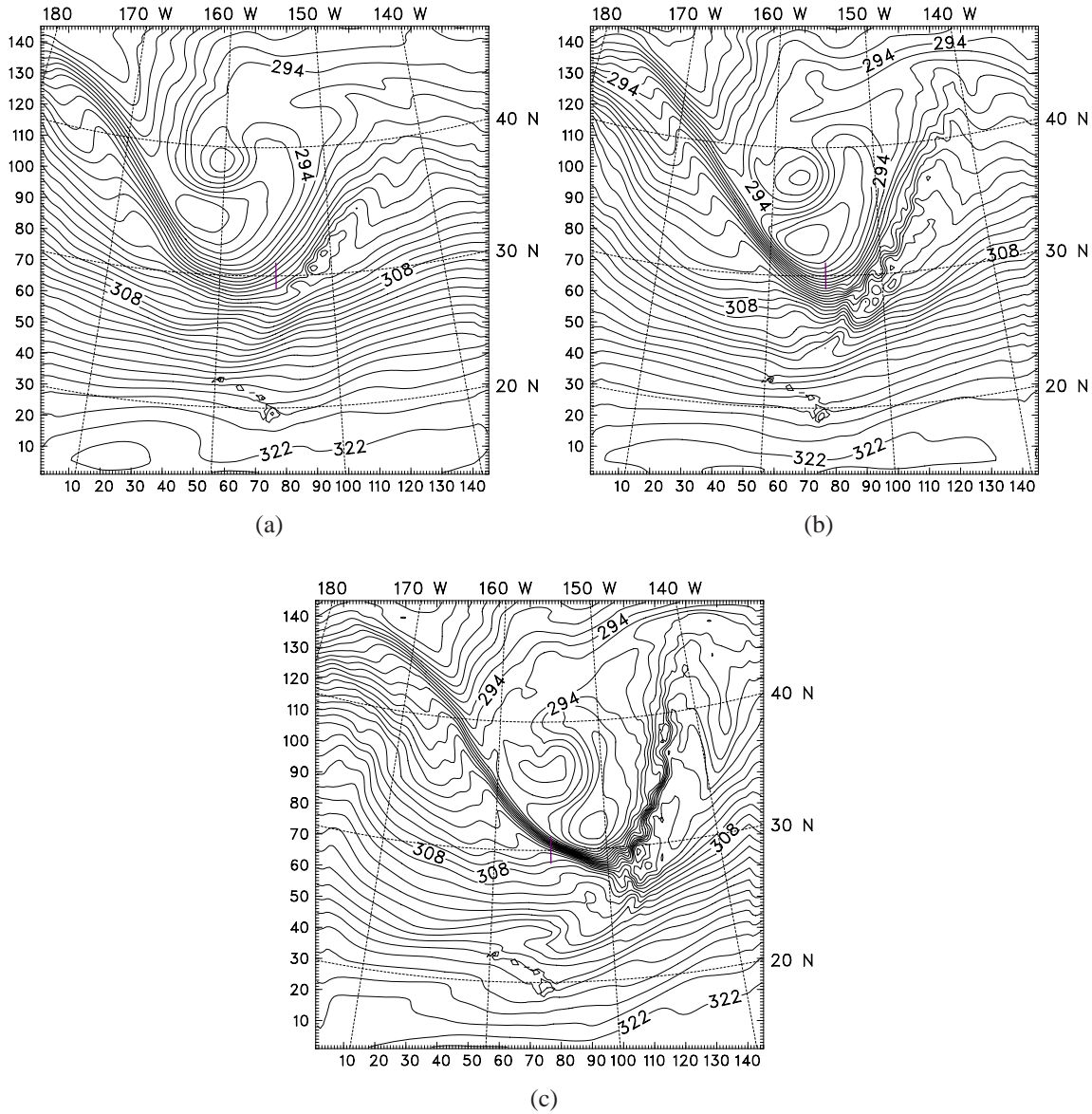
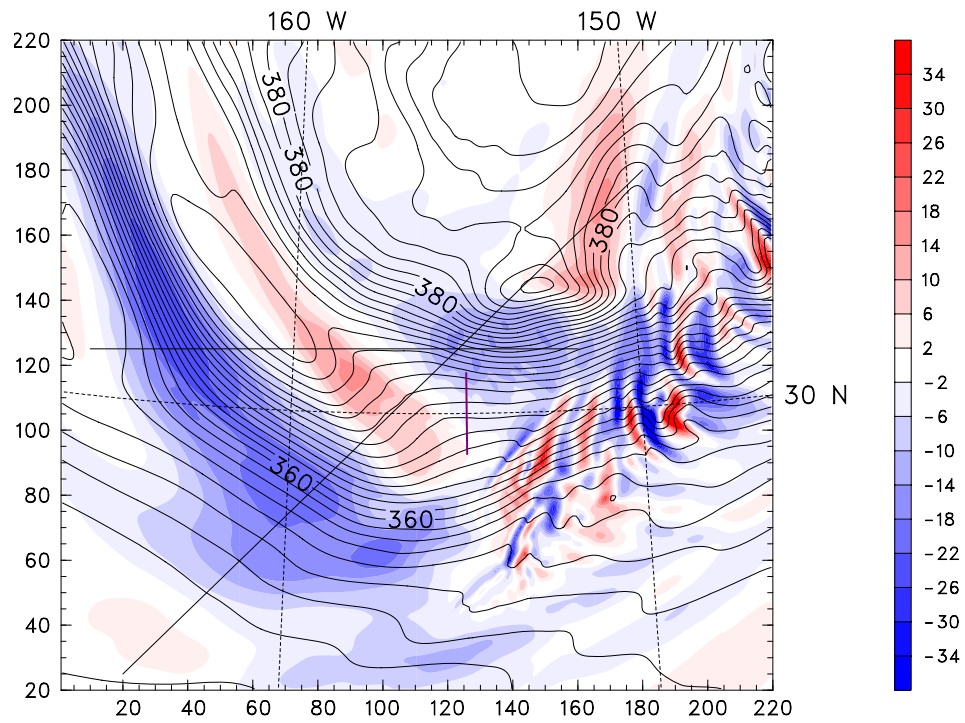


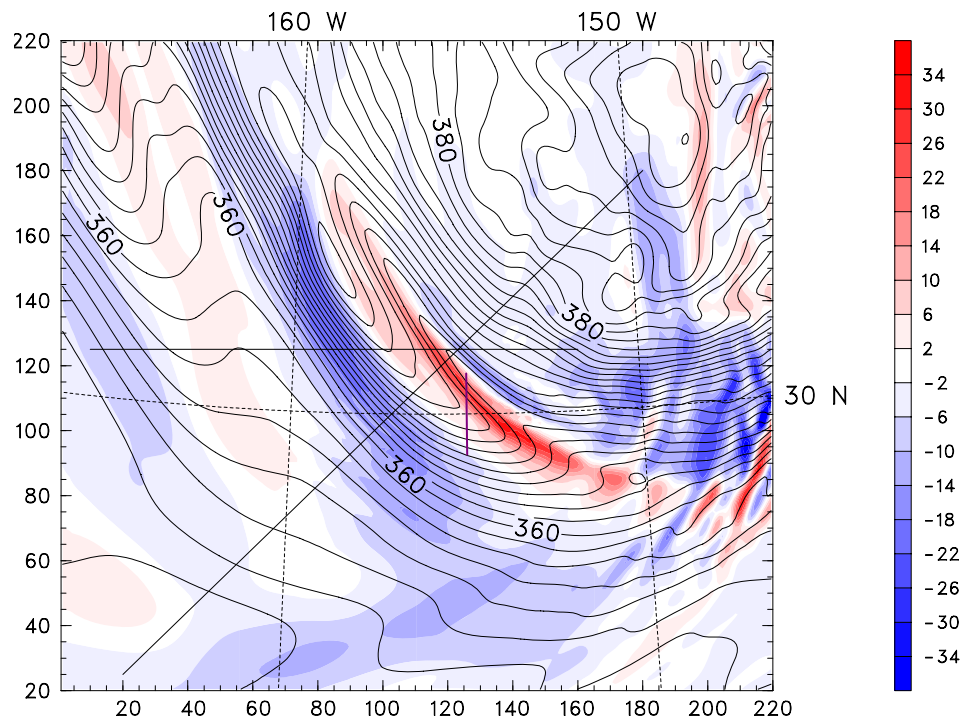
**Figure 3.4:** Data of run R2M D1 from 29 Jan 1998 at (a) 14 ,(b) 18 and (c) 22 UTC. Isentropes  $\theta$  (K, black contour lines,  $\Delta\theta = 1$  K) at 4 km altitude. G-IV CAT-encounter (violet line).

inertia-gravity wave (SGW) signal was about 600 m in both vertical sections (Figs. 3.6b and 3.7b). At 23 UTC, the SGW had amplitudes of  $|\nabla_h \cdot \mathbf{v}_h|_{max} = 1.8 \cdot 10^{-4} s^{-1}$  and  $|w|_{max} = 24 \text{ cms}^{-1}$  (not shown). Fig. 3.5 shows the dramatic change of horizontal wave structure at the 13 km-level from 18 to 23 UTC.

Animation of the vertical sections at different times clearly indicated an upward propagation of the SGW packet. The animation indicated that the wave packet emanated from the downreaching tongue of high velocity in the MTJ or the baroclinic zone beneath. Thus,

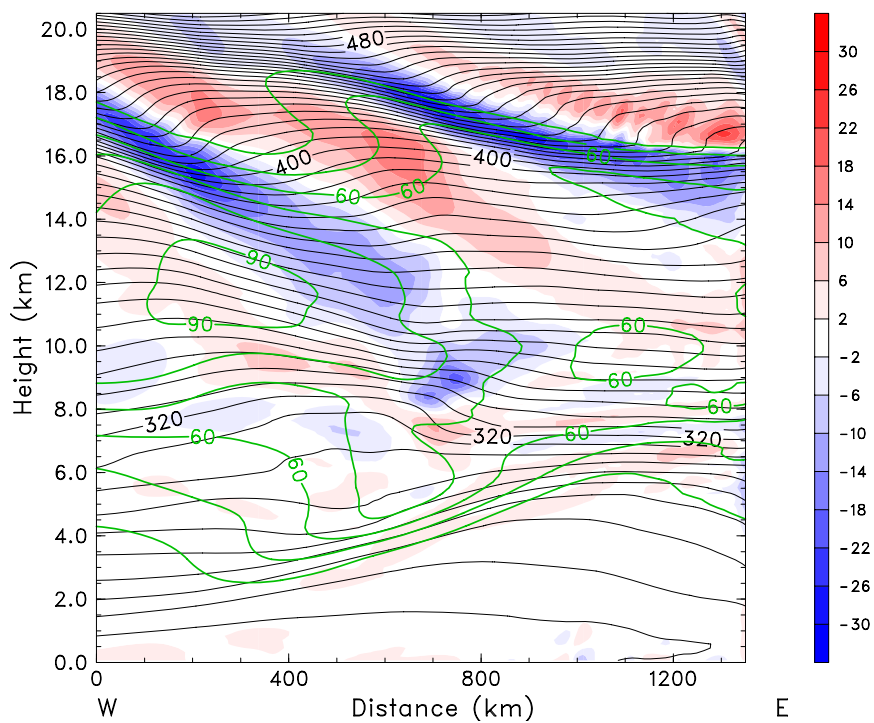


(a)

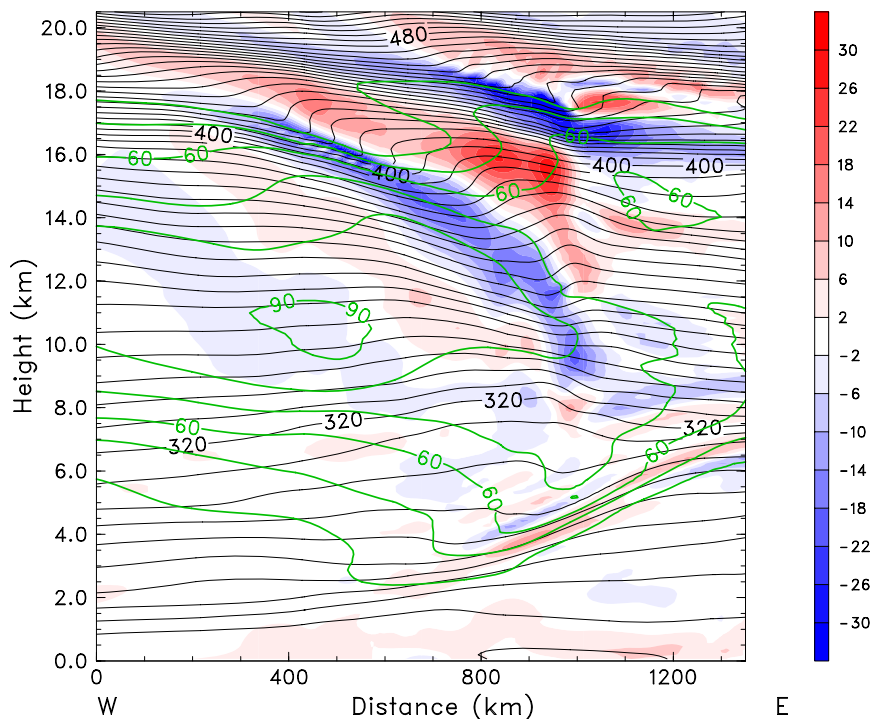


(b)

**Figure 3.5:** Data of run R2M D2 from 29 Jan 1998 at (a) 18 and (b) 23 UTC.  $\theta$  (K, black contour lines,  $\Delta\theta = 1$  K) and vertical velocity  $w$  ( $\text{cm s}^{-1}$ , shaded) at 13 km altitude. G-IV CAT-encounter (violet line).

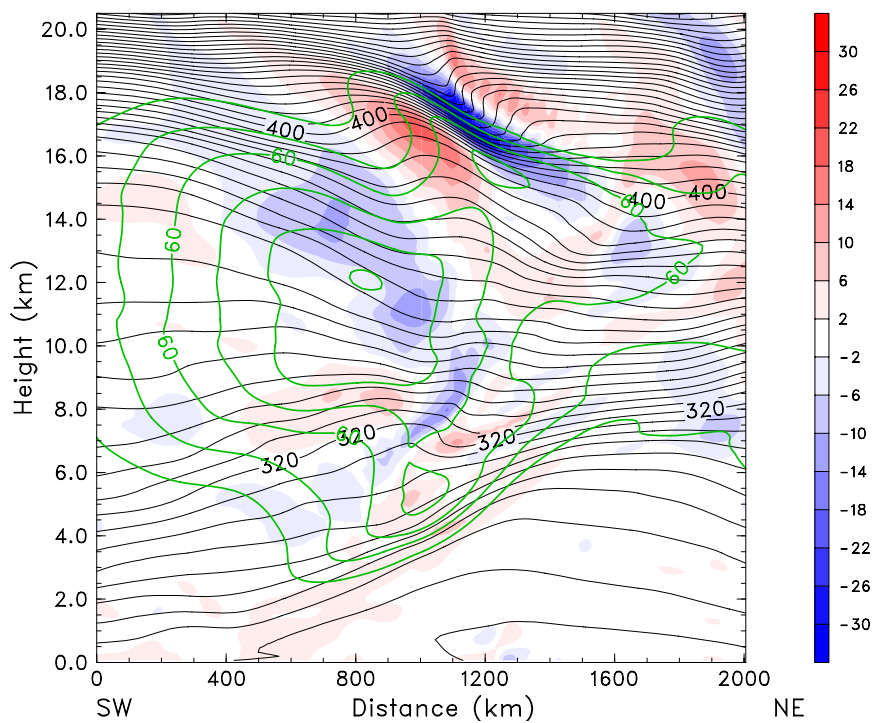


(a)

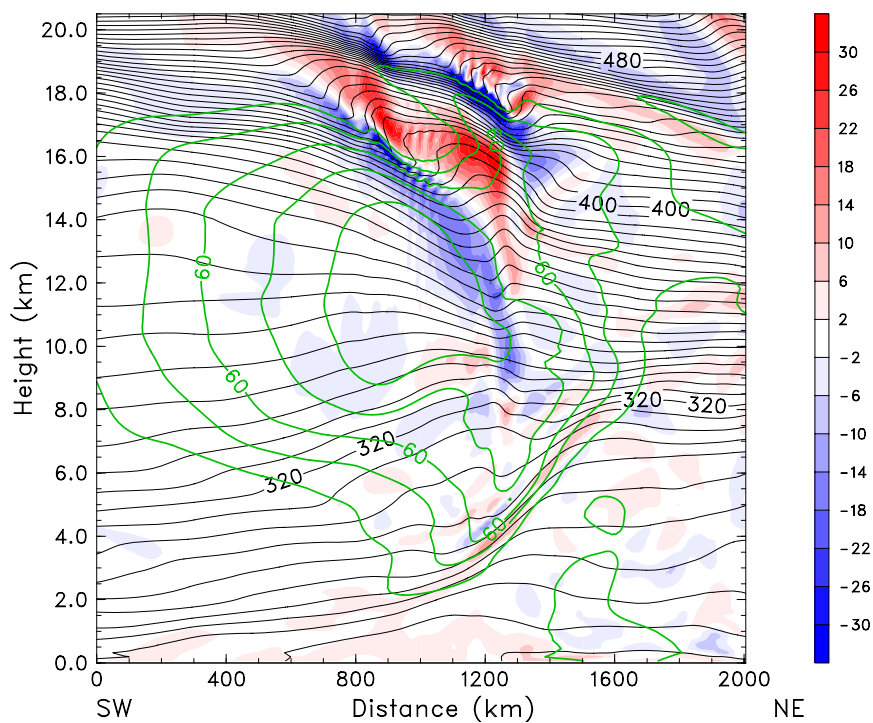


(b)

**Figure 3.6:** Data of run R2M D2 from 29 Jan 1998 at (a) 18 and (b) 23 UTC. Vertical cross-section along the black west-to-east line sketched in Fig. 3.5.  $\theta$  (K, black contour lines,  $\Delta\theta = 4$  K),  $v_h$  ( $\text{ms}^{-1}$ , green contour lines,  $\Delta v_h = 10 \text{ ms}^{-1}$ ) and  $\nabla_h \cdot \mathbf{v}_h$  ( $10^{-5} \text{ s}^{-1}$ , shaded).



(a)



(b)

**Figure 3.7:** Data of run R2M D2 from 29 Jan 1998 at (a) 18 and (b) 23 UTC. Vertical cross-section along the black southwest-to-northeast line sketched in Fig. 3.5.  $\theta$  (K, black contour lines,  $\Delta\theta = 4$  K),  $v_h$  ( $\text{ms}^{-1}$ , green contour lines,  $\Delta v_h = 10 \text{ ms}^{-1}$ ) and  $\nabla_h \cdot \mathbf{v}_h$  ( $10^{-5} \text{ s}^{-1}$ , shaded).

the numerical simulations suggest the contracted front as source region of the SGW packet. Probably, the strong vertical accelerations along the front caused up- and downward excursions of the isentropes large enough to excite the large-amplitude gravity waves. The background wind profile with increasing velocity with height favored their upward propagation.

The phase propagation of the SGW was in the direction  $\phi \approx 45^\circ$ . Note, that this was also the case for the LGW until 19 UTC as examined before. Its phase velocity relative to a ground-based observer, estimated as an average between 22 and 00 UTC, was  $c_h \approx 14.4 \text{ ms}^{-1}$ . At 23 UTC, the mean velocity parallel to the wavevector at 14 km altitude was  $v_{\parallel} \approx 30 \text{ ms}^{-1}$ , and then (3.2) leads to  $\hat{c}_h = -15.6 \text{ s}^{-1}$ . Horizontal and vertical wavelengths for this wave were estimated to  $\lambda_h \approx 143 \text{ km}$  and  $\lambda_z \approx 7.3 \text{ km}$ , respectively. This finally gives an intrinsic frequency of  $\hat{\omega} = \hat{c}_h k_h \approx 6.9 \cdot 10^{-4} \text{ s}^{-1}$  ( $\hat{\omega} \approx 9.4 f$ ).

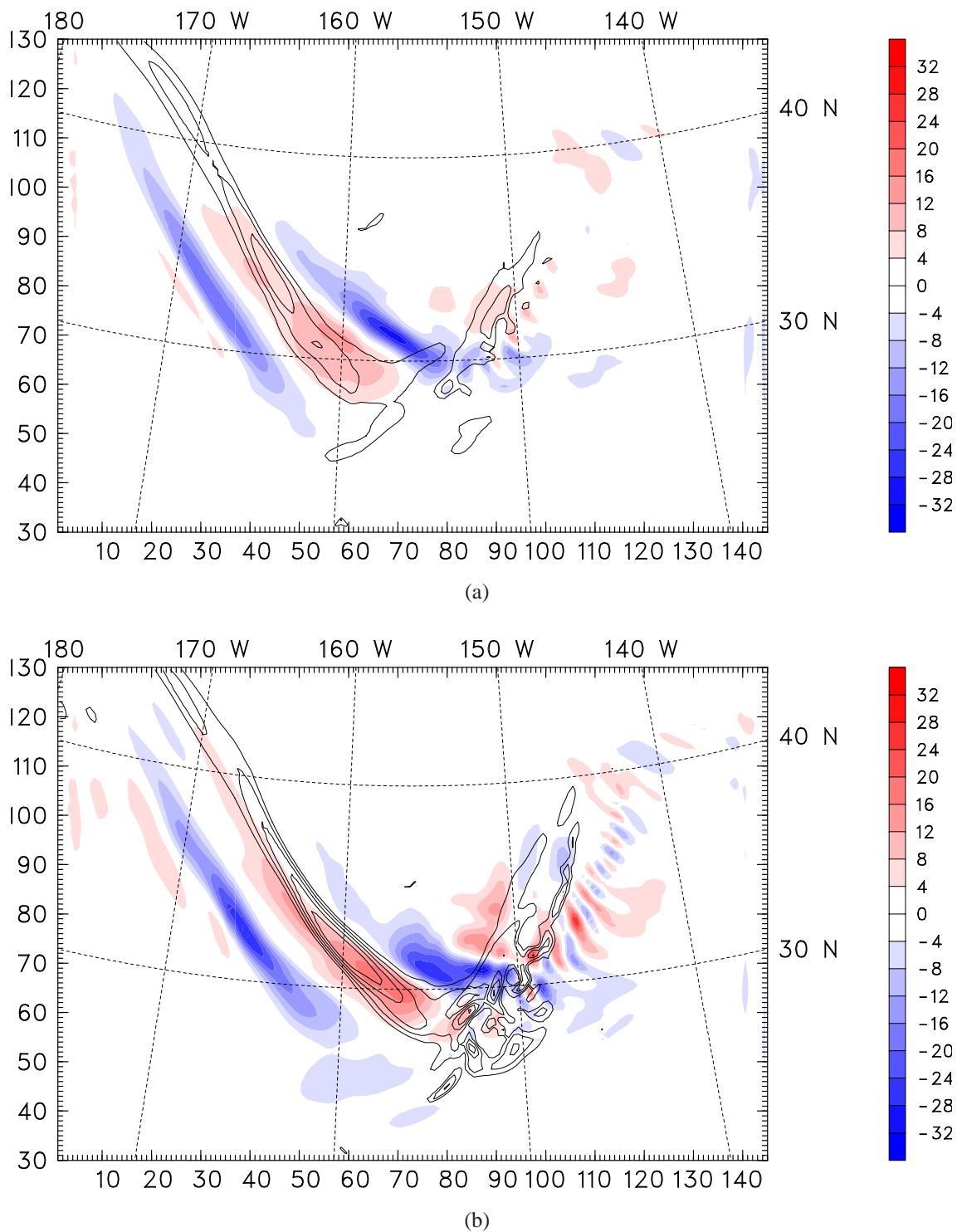
These SGW parameters result in an altitude of the corresponding critical level located above 20 km. From linear theory higher-frequency gravity waves in general have a higher vertical group velocity than lower-frequency waves. Also, the LGW was already retarded by its ICL. Therefore, the SGW propagated upwards through the jets into the LGW packet. This was clearly evident in the animations. Much interesting, an overturning of the isentropes, forming a convectively unstable region associated with the IGW motions, was simulated above the jet system in the lower stratosphere.

The simulated breaking of the wave occurred in a region where the backward (negative) vertical shear of the horizontal velocity was strongest below the ICL. The overturning intensified from 18 to 23 UTC (Figs. 3.6 and 3.7). Even if close to the lowest resolvable grid scale in the simulations, it is worth to mention some really small-scale features, likely to be waves that propagated away from the convective unstable region (such a region is likely to be turbulent in reality) in Fig. 3.7b. The employed grid resolution did not permit a further examination, and it is left whether these are physical or artificial disturbances resulting from numerical truncation.

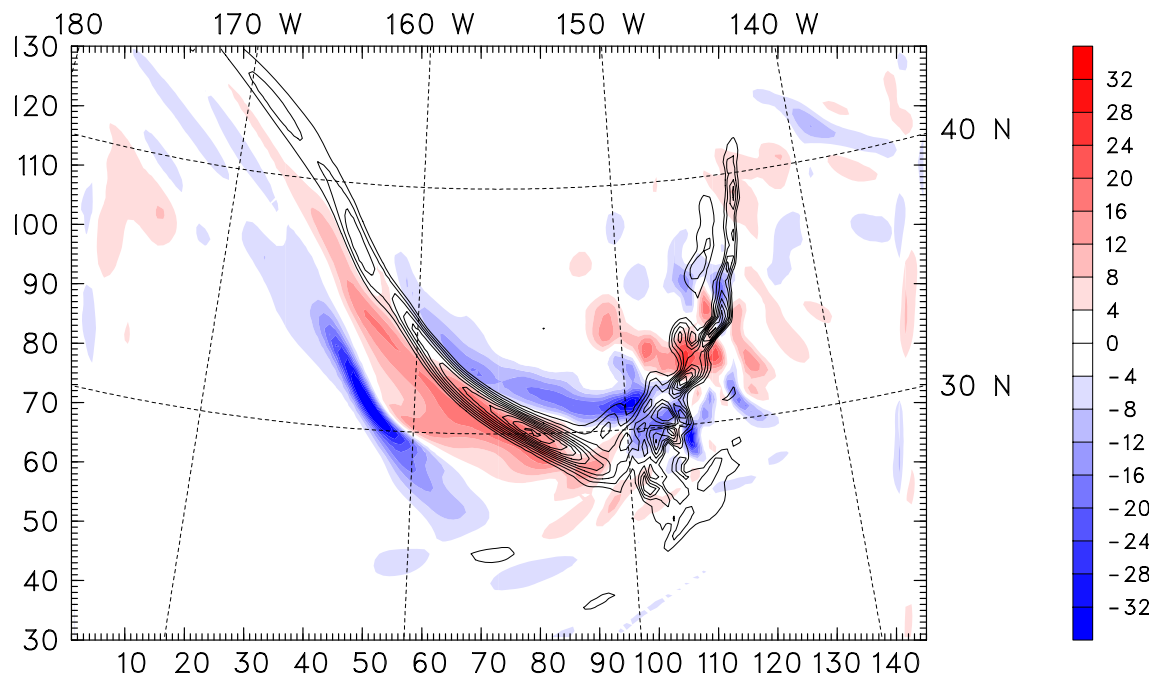
It is of value to examine the association of the low- to mid-tropospheric baroclinicity below the MTJ with the lower-stratospheric LGW packet in more detail.

Fig. 3.8 presents a superposition of the magnitude of the horizontal temperature gradient  $|\nabla_h T|$  (i.e. baroclinicity) at 600 hPa ( $\approx 4 \text{ km}$  geometrical height) and the lower-stratospheric  $\nabla_h \cdot \mathbf{v}_h$  at 100 hPa ( $\approx 12.5 \text{ km}$ ) at four different times from 15 UTC on January 29 till 00 UTC on January 30 1998. The related Table 2 lists some values of estimated parameters:  $|\nabla_h T|_{max}$  is the maximum contour value of  $|\nabla_h T|$  in association with north-west to south-east aligned front.  $\langle |\nabla_h \cdot \mathbf{v}_h|_{max} \rangle$  is a measure of the amplitude of the LGW which was determined by taking an average over the maximum  $\nabla_h \cdot \mathbf{v}_h$  contour values of the three front-aligned LGW phases. The quantity  $L_{\perp}$  is the cross-front scale. The arbitrarily taken minimum contour of  $|\nabla_h T|$  defined this average cross-front distance. The same procedure as for Table reftab:igw was applied to obtain  $\lambda_h$ .

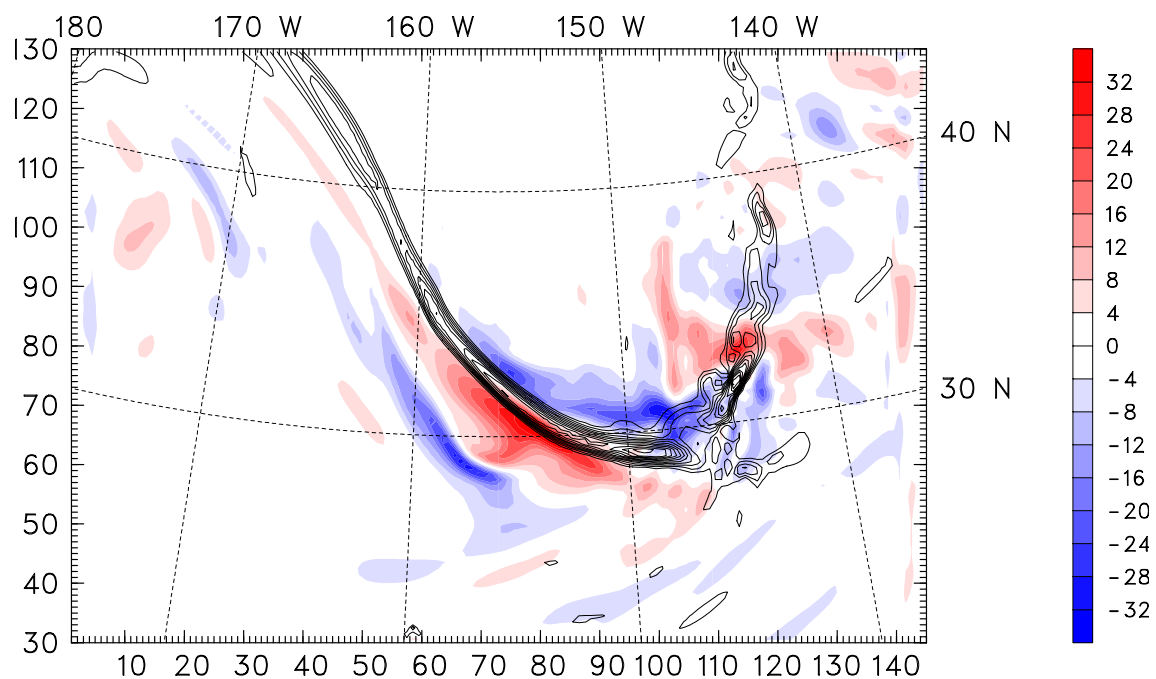
Fig. 3.8 and Table 2 stress two things. First, a connection of the LGW amplitude to the



**Figure 3.8:** Data of run R2M D1 from 29 Jan 1998 at (a) 15, (b) 18, (c) 21 UTC and 30 Jan (d) 00 UTC.  $|\nabla_h T|$  ( $10^{-5}$  K/m, black contour lines,  $\Delta|\nabla_h T| = 1.0 \cdot 10^{-5}$  K/m, minimum contour:  $3.0 \cdot 10^{-5}$  K/m) at the 600 hPa pressure surface and  $\nabla_h \cdot \mathbf{v}_h$  ( $10^{-5} s^{-1}$ , shaded) at 100 hPa.



(c)



(d)

**Figure 3.8:** (continued)

Time(UTC)	$ \nabla_h T _{max}(10^{-5} \text{ K/m})$	$\langle  \nabla_h \cdot \mathbf{v}_h _{max} \rangle (10^{-4} \text{ s}^{-1})$	$L_{\perp}(\text{km})$	$\lambda_h(\text{km})$
15	5.0	1.4	175	520
18	7.0	1.6	191	526
21	13.0	1.9	135	418
00	13.0	1.9	108	378

**Table 2:** Some parameters related to Fig. 3.8. See text for a description.

lower- to mid-tropospheric baroclinicity, and second, of the horizontal scale of the LGW to the cross-frontal scale.

From 15 to 18 UTC and from 18 to 21 UTC, an increase of  $\langle |\nabla_h \cdot \mathbf{v}_h|_{max} \rangle$  was accompanied by an increase of  $|\nabla_h T|_{max}$ . Afterwards, both quantities were constant until 00 UTC (see Table 2).

As  $L_{\perp}$  increased only slightly about 16 km from 15 to 18 UTC,  $\lambda_h$  was practically constant. Subsequent to 18 UTC, the frontal collapse of  $L_{\perp}$  was associated with a significant shortening of  $\lambda_h$  in the lower stratosphere (see Table 2). The cross-front scale  $L_{\perp}$  contracted about 83 km (43 %) while  $\lambda_h$  about 148 km (28 %) from 18 to 00 UTC.

The LGW phases are aligned with the 600 hPa-front during the entire period of Fig. 3.8a-d, and high magnitudes of  $|\nabla_h T|_{max}$  and  $\langle |\nabla_h \cdot \mathbf{v}_h|_{max} \rangle$  occurred in the same regions along the front.

The demonstrated relationships for the frontal quantities ( $|\nabla_h T|_{max}$ ,  $L_{\perp}$ ) existed on pressure levels in the interval  $500 < p < 700$  hPa. In contrast, for the frontal quantities on upper tropospheric levels (e.g. 300 hPa, 200 hPa) the connections were inexistent.

### 3.3 Comparison with observations

A comparison of run R2M with the observations from the G-IV is presented next. The focus is on the dynamics important for the generation of CAT at flight level. As shown in Fig. 3.5, the simulated SGW packet propagates upwards directly into the region where the G-IV encountered the CAT.

Fig. 3.9 presents a vertical south-north cross-section along the same baseline as the dropsonde vertical cross-section of Fig. 2.7 and coinciding with the violet line in Fig. 3.5. It displays the jet system with the strong shear layer below the MTJ in a view to the west (in contrast, Fig. 2.7 points to the east). Note that the latitudinal ranges displayed in Figs. 2.7 and 3.9 differ.

The simulated cold air dome, the northward upsloping front and the associated strong mid-tropospheric shear layer around distance = 1000 km (Fig. 3.9) resemble the observations (Fig. 2.7). The vertical distance of low static stability south to the MTJ between 600 and 360 hPa is  $\approx 3.5$  km in the observations (Fig. 2.7). Fig. 3.9 gave  $\approx 3.5$  km also for the simulations.

The simulations clearly reproduced the observed wave perturbations below the CAT-

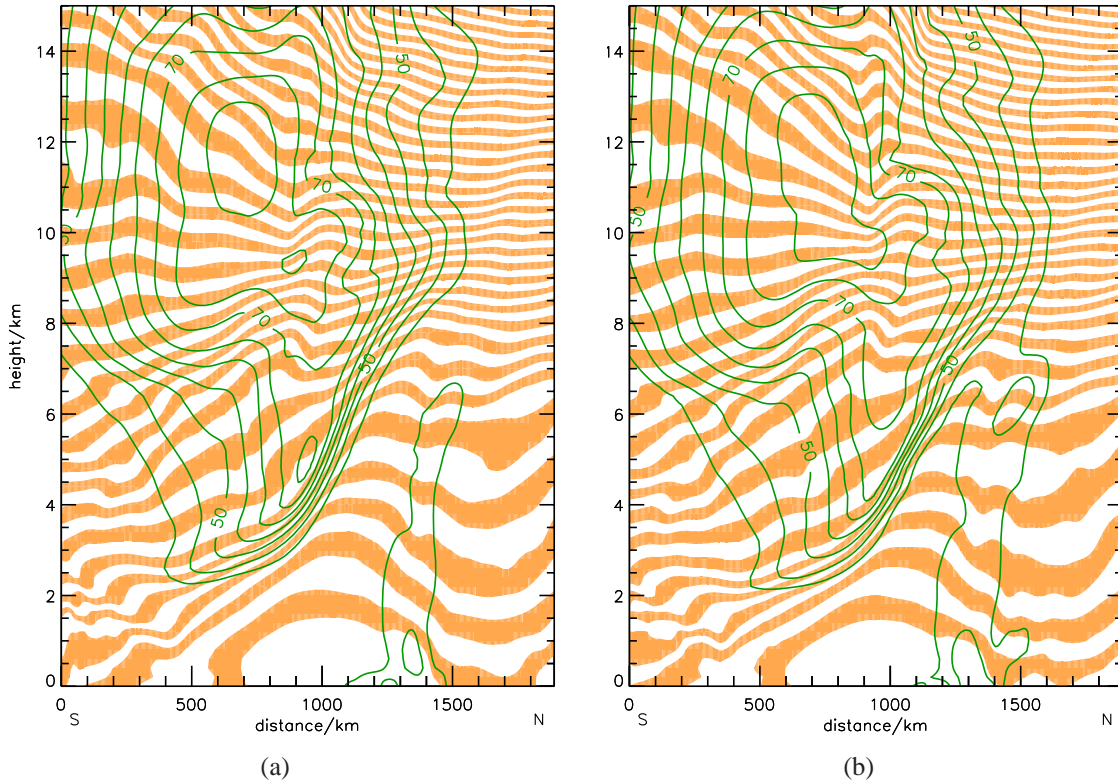


**Figure 3.9:** Data of run R2M D2 from 29 Jan 1998 at (a) 2130 and (b) 2230 UTC. Along-flight-track (south-north) vertical cross-section.  $\theta$  (K, shaded,  $\Delta\theta = 2$  K) and  $v_h$  ( $\text{ms}^{-1}$ , green contour lines,  $\Delta v_h = 5$   $\text{ms}^{-1}$ ).

region coinciding with the dropsonde observations between 2112 and 2129 UTC. As described in Section 3.2b, their occurrence is related to the strong frontogenesis associated with the MTJ. The simulations demonstrate a vertical propagation from the region of the mid-tropospheric front/jet system upwards through the cyclonic shear side of the STJ-core (Fig. 3.9). That is the case also in the dropsonde-derived cross-section (Fig. 2.7). The isentropes along the section give  $\lambda_h \approx 150$  km,  $\lambda_z \approx 6$ -8 km and a maximum peak-to-peak amplitude of  $\approx 500$  m at 2230 UTC (Fig. 3.9b). In comparison, the dropsonde-derived section (Fig. 2.7) gives  $\lambda_h \approx 100$ -150 km,  $\lambda_z \approx 3$ -4 km and a maximum peak-to-peak amplitude of  $\approx 750$  m (Section 2.2). The simulated upward propagating SGW lagged the observations by about 1 hour.

In the discussion of Fig. 2.7, layered structures in the isotachs and isentropes far to the north of jet system in the lower stratosphere were presumed to be associated with another IGW perturbation. Time animation of the vertical section (Fig. 3.9) showed this perturbation to be present in the simulation as well. A hodograph analysis of the simulation data of run R2M D2 at distance = 1600 km (Fig. 3.9) in the height range 9-13 km at 2130 UTC identified an upward propagating IGW. A weak signal of this wave can be discerned in Fig. 3.9a between distance = 1400 and 1800 km.

A calculation of the Richardson number  $Ri$  (2.3) along the same south-north cross-

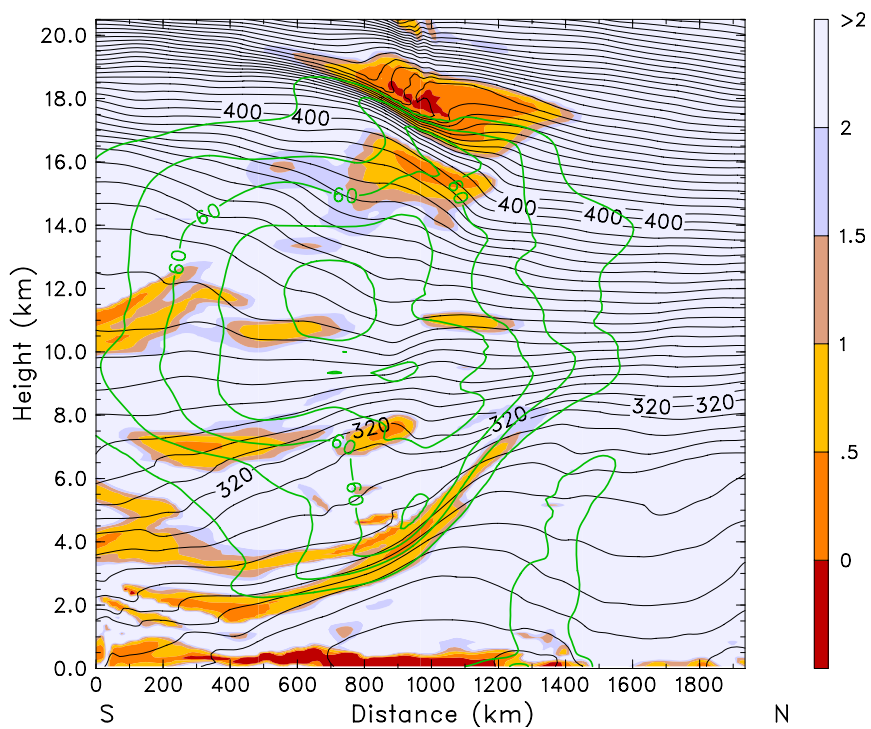
section using the model output of R2M in the domain D2 indicates regions susceptible to a shearing (or dynamical) instability and the possible generation of small-scale turbulence (Fig. 3.10). To note again, the grid sizes of the MM5-simulations are far too coarse from resolving small-scale turbulence explicitly, even though the computational effort was enormous (in relation to current general computer performance).

The simulation results indicate locations of low Richardson numbers throughout the jet system: regions of  $Ri < 1$  existed along the northward upsloping shear layer beneath the MTJ between 1 and 8 km altitude, some patches of  $Ri < 1$  occurred in regions with low static stability and low shear values, especially on the anti-cyclonic shear side of the STJ, and, finally, in the negative shear region above the jet system in the lower stratosphere. The latter region was influenced by the upward propagating LGWs motions. They locally altered the background (wave undisturbed) state of  $\theta$  and  $v_h$  (wave-modulated Richardson number, see Section 4.1). As mentioned earlier, these LGW motions propagated towards their critical level, overturned and broke. Thereby they formed a convectively unstable region which is indicated by the negative  $Ri$ . By examining the  $\theta$ -contours upwards from the MTJ in Fig. 3.10, one perceives the upward propagating SGW as discussed before. Unfortunately, no regions with low  $Ri$  were simulated in the vicinity of the NOAA's G-IV flight level (at  $\approx 12.6$  km altitude). This is in contrast with the G-IV observations (see Fig. 2.8 and the respective discussion).

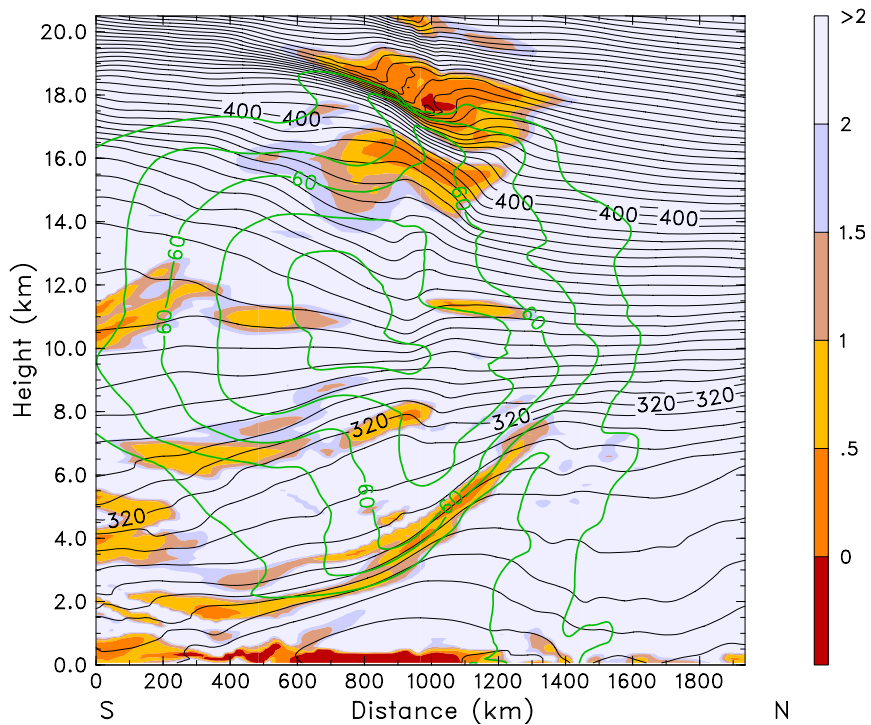
We tested various vertical cross-sections at adjacent locations from all different simulations in search of low  $Ri$  regions. However, none of the tested sections revealed any indication of low  $Ri$  close to the G-IV flight level. The reason for this disagreement is the smaller value of the simulated vertical shear of  $v_h$  compared to the observed profiles. This can be seen by a matching of Figs. 3.10 and 3.9 with the dropsonde vertical section Fig. 2.7. Fig. 3.11 directly compares 2118-UTC dropsonde DS3 (see Section 2.2) with simulated vertical profiles taken from domain D2 of the model run R2M.

The comparisons depicted in Fig. 3.11 pinpoint the absence of the observed velocity maximum at around 11.5 km altitude in the simulations. The observed velocity maximum was associated with the core of the STJ. In reality, they were  $10\text{-}20\text{ ms}^{-1}$  higher in comparison to the simulations. As discussed in Section 2.2b, the strong vertical shear of  $v_h$  above the maximum led to a low bulk Richardson number of  $Ri_B \approx 0.47$  indicating a dynamically unstable flow situation in a layer adjacent to the flight level of the G-IV. Except for the weakly developed jet at 2230 UTC, practically no such a STJ-velocity maximum was simulated in the numerical experiments. This was also the case at 2030 UTC when the velocity profile in the mid-troposphere, especially between 2 and 5 km altitude, matched best the observations. The absence of a pronounced core of the simulated STJ caused the very low shear values and, eventually, the large Richardson numbers  $Ri \gg Ri_c$  at the altitude of the G-IV-overflight. This finding applied to all simulations performed (not shown).

We suspect that the synoptic-scale ECMWF analyses used to initialize and force the MM5-simulations underpredicted the strength of the STJ. Unfortunately, because of the



(a)



(b)

**Figure 3.10:** Data of run R2M D2 from 29 Jan 1998 at (a) 2130 and (b) 2230 UTC. Along-flight-track (south-north) vertical cross-section.  $Ri$  (shaded),  $\theta$  (K, black contour lines,  $\Delta\theta = 4$  K) and  $v_h$  ( $\text{ms}^{-1}$ , green contour lines,  $\Delta v_h = 10\text{ms}^{-1}$ ).

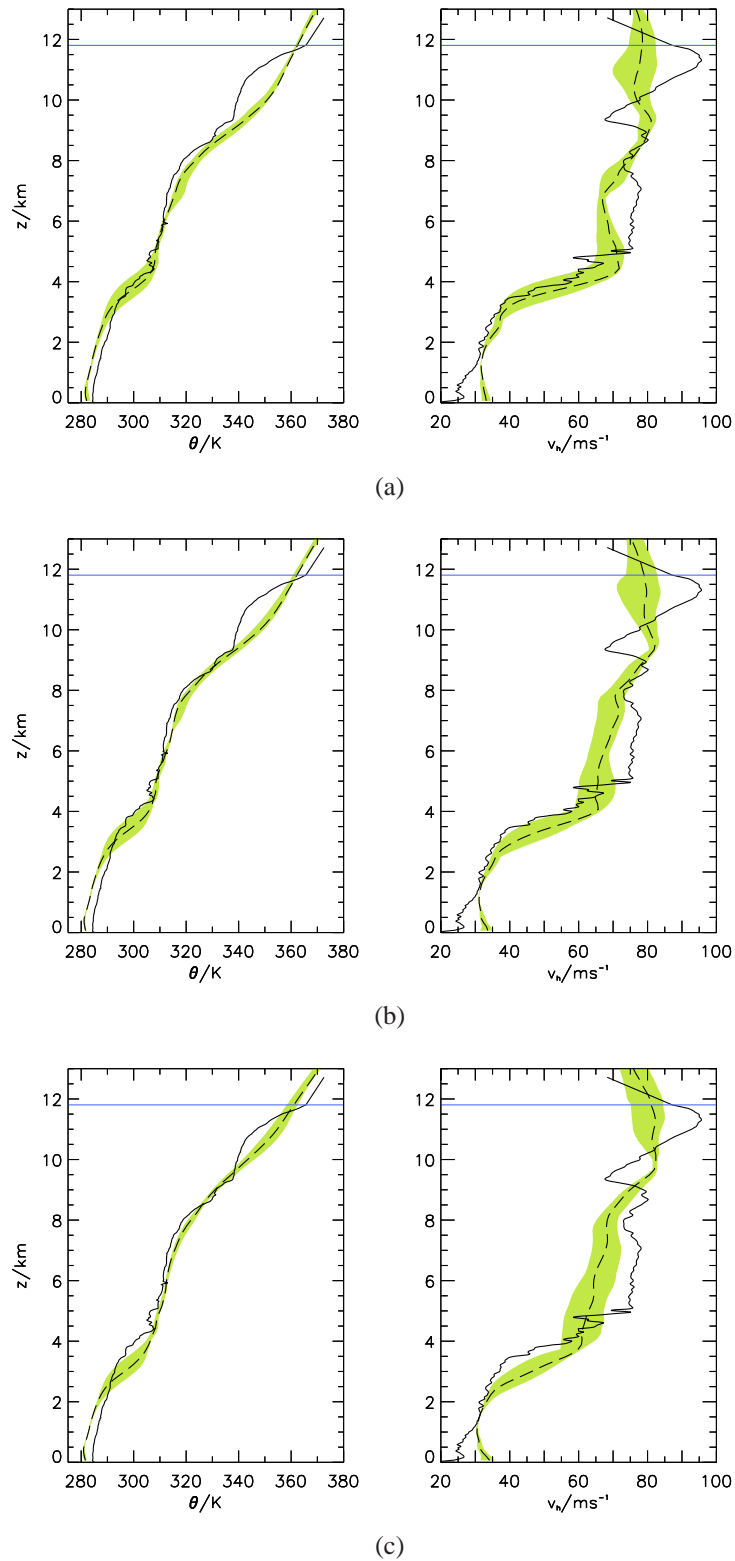


**Figure 3.11:** Vertical profiles of  $\theta$  (K) (left panel) and  $v_h$  ( $\text{ms}^{-1}$ ) (right panel). The solid line at all times represents the profile from dropsonde DS3. Simulation data from run R2M D2 from 29 Jan 1998 at (a) 2030, (b) 2130 and (c) 2230 UTC: corresponding profiles at the release position of dropsonde DS3 (29.95°N, 155.49°W) (dashed line), minimum and maximum values taken from an array of 5 model grid points in every horizontal direction starting from the release position of dropsonde DS3 (shaded).

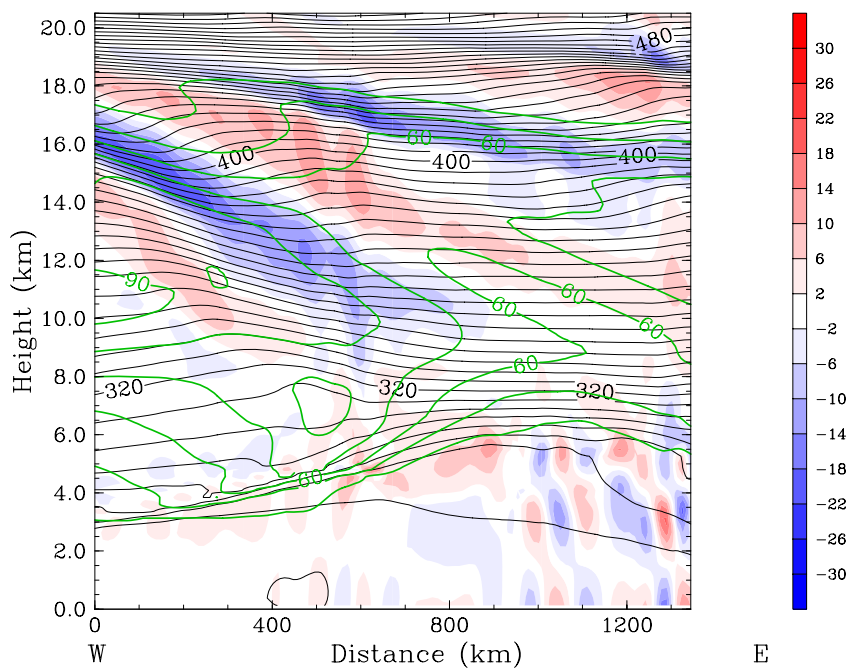
coarse temporal resolution of the ECMWF data, no direct comparison with this data and the observations in the region of the STJ and the CAT encounter was possible. An along-flight track vertical section similar to Fig. 2.7 and 3.9 using the ECMWF data from 29 Jan 18 UTC and 30 Jan 00 UTC indicated STJ maxima of 80 and 85  $\text{ms}^{-1}$ , respectively. These values were similar to the MM5 simulations. Therefore the ECMWF analysis data used to initialize and force the MM5 simulations likely imposed the lower STJ velocities. Underpredicted jet velocities in the ECMWF analysis might be partially due to the relatively low spatial (especially vertical) resolution of in January 1998. On the other hand, very few observations were used for the assimilation over the data-sparse Pacific Ocean (remember, one of the main reasons for NORPEX-98 was to supply additional observations to improve the forecast skill of the numerical weather prediction). Because the first dropsonde was released just 10 minutes before the CAT-encounter, none of the G-IV-sampled data could be used to improve the simulations, even though the MM5 modeling system has a 4-dimensional variational assimilation scheme. In a recent study performed by Weissmann et al. 2005, ECMWF data still showed deviations of windspeeds up to  $\pm 15 \text{ ms}^{-1}$  from airborne wind lidar observations over the data-sparse Atlantic Ocean. This was even though the data used in their study was at a spectral resolution T511 (triangular truncation) with 60 vertical layers compared to T213 with 31 vertical layers in our study.

### 3.4 Differences between MM5 simulations

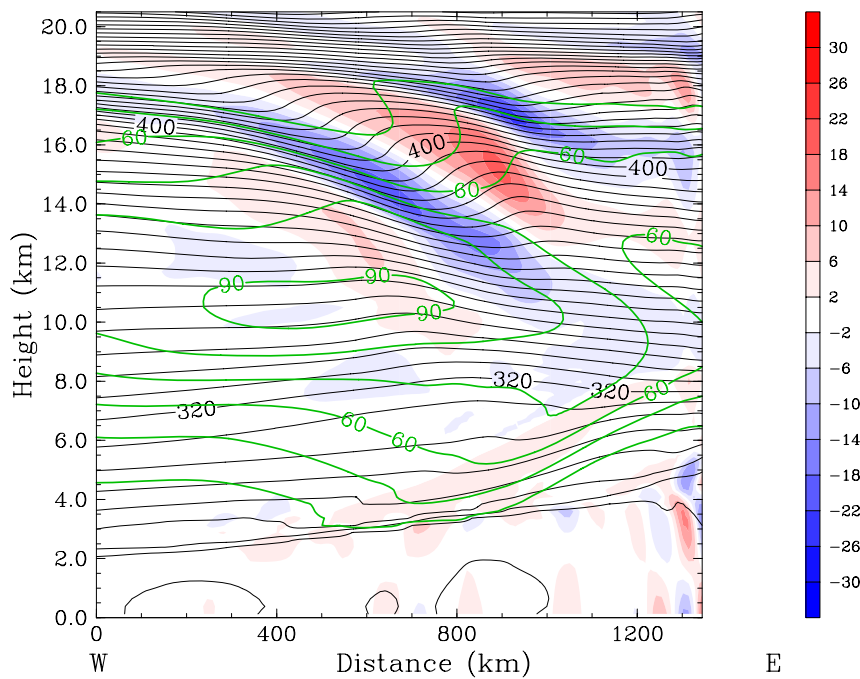
Up to now, results only from the simulations with domain configuration R2 (see Table 3 in Appendix A) were presented. As noted at the beginning of this chapter, these high-resolution runs matched the dropsonde observations best with respect to the gravity wave appearance. Simulations with the domain configuration R1 did not capture the described SGW emission, i.e. the formation of a IGW packet with a clearly higher aspect ratio ( $\lambda_z/\lambda_h$ ). For simulation times before 18 UTC on 29 Jan, the IGW dynamics occurred similar in runs R2 and R1.

The much weaker SGW emission of run R1 is illustrated in Fig. 3.12 showing a vertical cross-section equal to that of Fig. 3.6, but from run R1M D2 compared to run of R2M D2. The IGW amplitudes in the R1-D2-simulation (Fig. 3.12) were generally smaller. A horizontal contraction and a growth of the aspect ratio of the LGW packet from 18 to 23 UTC occurred also in R1 D2. However, the respective changes of the IGW characteristics were much less pronounced compared to run R2. Especially, the distinct signal of the SGW above the MTJ system is practically non-existent in Fig. 3.12. In addition, the simulated overturning of the isentropes in the negative shear region between 15 and 19 km altitude of runs R2 (see Fig. 3.6b) did not occur in R1.

As described in Section 3.2b discussing the run R2M, the SGW emission was related to the strong contraction of the isentropes at mid-tropospheric levels (i.e., 4 km- $\theta$  (Fig. 3.4)). A similar section for run R1M D1 (Fig. 3.13) depicts a rather different frontal evolution. The temporal continuous and spatially uniform contraction of the isentropes and the inten-



(a)



(b)

**Figure 3.12:** Data of run R1M D2 from 29 Jan 1998 at (a) 18 and (b) 23 UTC. Vertical cross-section along the black west-to-east line sketched in Fig. 3.5.  $\theta$  (K, black contour lines,  $\Delta\theta = 4$  K),  $v_h$  ( $\text{ms}^{-1}$ , green contour lines,  $\Delta v_h = 10 \text{ms}^{-1}$ ) and  $\nabla_h \cdot \mathbf{v}_h$  ( $10^{-5} \text{s}^{-1}$ , shaded).

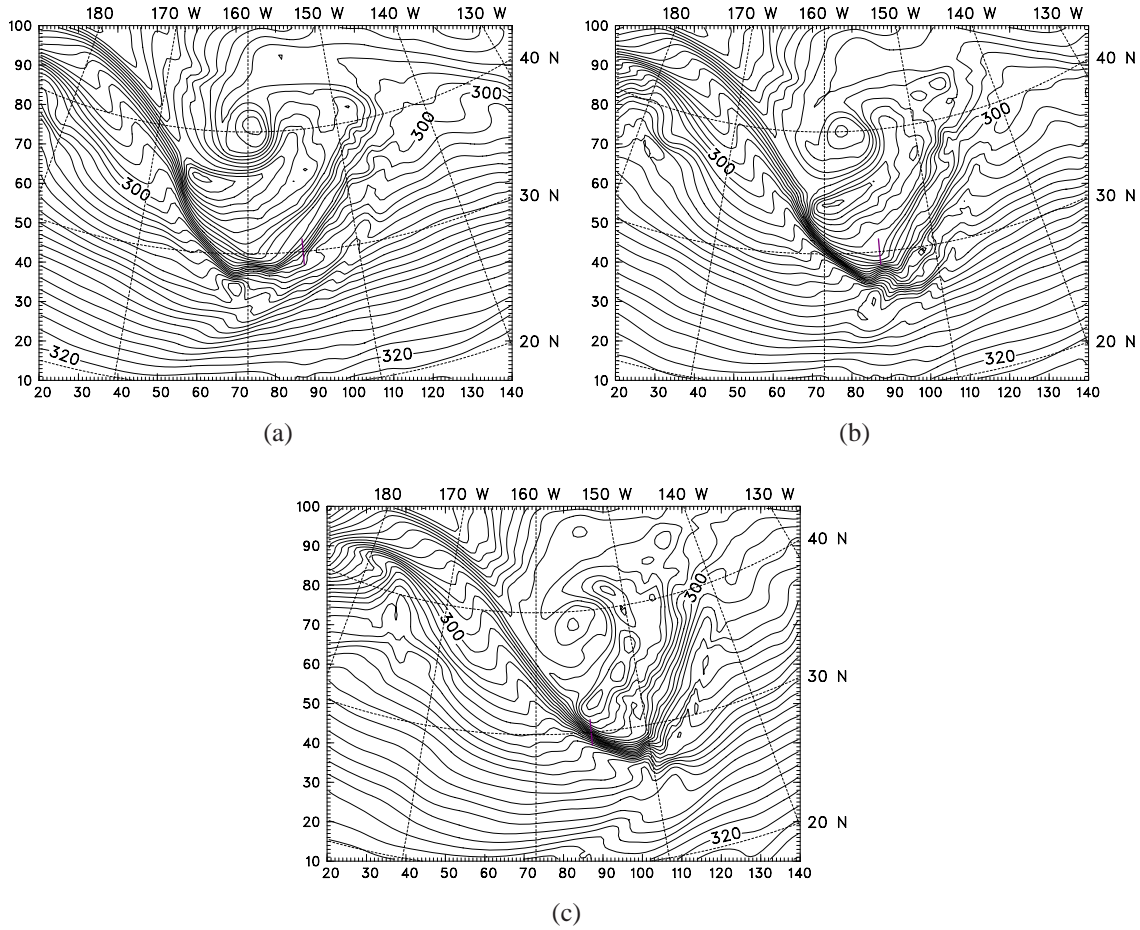


**Figure 3.13:** Data of run R1M D1 from 29 Jan 1998 at (a) 14 ,(b) 18 and (c) 22 UTC. Isentropes  $\theta$  (K, black contour lines,  $\Delta\theta = 1$  K) at 4 km altitude. G-IV CAT-encounter (violet line).

sification of the baroclinicity along the north-west to south-east aligned front from 14 to 22 UTC simulated by run R2M (Fig. 3.4), was interrupted in run R1M (Fig. 3.13). There was a partial intensification (not along the entire front) of the front from 14 to 18 UTC in R1M D1, but virtually no further intensification from 18 to 22 UTC (Fig. 3.13).

The different numerical results might be attributed to the different initialization times (runs of type R1 were started 12 hours before that of R2), the alignment of the integration domains (the domain boundaries of run R2 were apparently more advantageously positioned to simulate the flow in the region surround the CAT event) and the numerical resolutions of the simulations (the R2-simulations use much higher horizontal and vertical resolutions than R1: see Appendix A for details about the different MM5 simulations).

Analysing the different runs, it turned out that the spatial resolution played an important role in the simulation of the vertically propagating SGWs and the wave breaking region between 15 and 19 km altitude. Numerical experiments with the domain configuration R1 never simulated these smaller-scale waves and the stratospheric breaking. Most

likely, the lower numerical resolution and the associated greater numerical dissipation prevented or delayed the convective breaking of the LGW. It is important to note, that a two-way nesting scheme was utilized between the simulation domains of different horizontal resolutions. That means, the larger domains, with a coarser horizontal resolution, received a feedback from the smaller (inner) domains, which had a higher horizontal numerical resolution. For example, grid points of run R2M D2 within the boundaries of R2M D3 carried data which was integrated on D3, but afterwards interpolated to D2.

The results of this section suggest that the strong SGW emission simulated in runs R2 was dynamically connected to the strong frontogenesis below the MTJ system. However, it actually remains to be shown whether the influence of the numerical resolution finally resulted in the strong SGW emission alone. Up to now, no simulations with the same configuration as R2 and a coarser numerical resolution (i.e, without the innermost domain) were performed. Finally, the dry simulations R2D were, in terms of the gravity wave appearance, practically similar to the moist simulations R2M (compare Fig. 3.6 to Fig. 5.9 of Chapter 5). Thus, moisture had no important influence on the appearance of the SGW.



## 4 Clear-air turbulence generation mechanisms

Although the MM5 runs did not simulate the CAT region encountered by the G-IV (i.e., a dynamical unstable or even a convective unstable stable zone nearby) explicitly, they serve to identify hypotheses about processes which could have led to the observed CAT.

### 4.1 Wave-turbulence coupling

As a gravity wave propagates through an undisturbed (background) environment, a local modulation of the Richardson number field can result (e.g. Einaudi and Lalas 1975; Pavelin et al. 2001; Lane et al. 2004). This is theoretically demonstrated as follows (e.g. Lane et al. 2004). The Richardson number, defined in (2.3), can be written in height coordinates as,

$$Ri = \frac{g/\bar{\theta} (\partial_z \bar{\theta} + \partial_z \theta')}{(\partial_z \bar{u} + \partial_z u')^2 + (\partial_z \bar{v} + \partial_z v')^2} \quad (4.1)$$

in which the bar denotes variables of the background state and primes identify the wave perturbations, essentially  $\theta = \bar{\theta} + \theta'$ ,  $u = \bar{u} + u'$  and  $v = \bar{v} + v'$ . Assuming plane wave solutions of the form

$$u' = \tilde{u} \cos(\varphi + \alpha_u) \quad v' = \tilde{v} \cos(\varphi + \alpha_v) \quad \theta' = \tilde{\theta} \sin(\varphi) \quad (4.2)$$

with  $\tilde{u}$ ,  $\tilde{v}$  and  $\tilde{\theta}$  being the wave amplitudes of zonal, meridional velocity and potential temperature.  $\varphi = kx + ly + mz + \omega t$  describes the wave phase, in which  $k$ ,  $l$  and  $m$  are wave numbers in the directions of the Cartesian coordinates  $x$ ,  $y$  and  $z$ , respectively,  $\omega$  denotes the wave frequency relative to a fixed observer and  $t$  is the time. The parameters  $\alpha_u$  and  $\alpha_v$  are phase differences of the wave perturbations. Note, that the wave disturbances  $u'$ ,  $v'$  and  $\theta'$  are coupled via a set of equations describing the atmospheric dynamics. The general equations are adjusted or approximated to the problem under consideration, i.e. starting with the primitive equations one finally arrives at the polarization relations for inertia-gravity waves (e.g. Holton 1992; Fritts and Alexander 2003). By inserting (4.2) into (4.1) and assuming  $m \approx const.$  (actually performing the Wenzel-Kramers-Brillouin (WKB) approximation, see, for example, Nappo 2002),

$$Ri = \frac{g/\bar{\theta} (\partial_z \bar{\theta} + m\tilde{\theta} \cos(\varphi))}{(\partial_z \bar{u} - m\tilde{u} \sin(\varphi + \alpha_u))^2 + (\partial_z \bar{v} - m\tilde{v} \sin(\varphi + \alpha_v))^2}. \quad (4.3)$$

If the products of the vertical wavenumber  $m$  with the amplitudes are large enough so that,

$$m\tilde{u} \sim \partial_z \bar{u} \quad m\tilde{v} \sim \partial_z \bar{v} \quad m\tilde{\theta} \sim \partial_z \bar{\theta} \quad (4.4)$$

then the wave motions do have a significant influence on  $Ri$ . If appropriate, a local reduction of  $Ri$  can lead to a shearing instability when  $Ri < Ri_c$ .

A modulation of the  $Ri$  through IGW motions occurred also in the MM5 simulations conducted. Again referring to Fig. 3.10, bands of low  $Ri$  numbers in the strong negative shear above the jet system, which were aligned with the LGW fronts, have been simulated. These were definitely influenced by the upward propagating, large-amplitude LGW packet. The LGW motions in interaction with strong background shear even resulted in a convective instability, which is indicated by negative values of  $Ri$ . Low values of  $Ri$  along the strong shear layer below the MTJ, in contrast, resulted from a strong background shear, because this region was apparently less affected by gravity wave perturbations.

## 4.2 Some hypotheses about the clear-air turbulence generation

As discussed in Section 2.2, the G-IV encountered moderate-to-severe CAT in the negative shear region of the intense jet system (see, Figs. 2.6, 2.7 and 2.8). During the encounter, the G-IV flew at a flight altitude of  $\approx 12.6$  km ( $\approx 175$  hPa) at the upper boundary of a dynamically unstable layer ( $Ri_B \approx 0.47$ ) with a depth of approximately 1 km. It is likely therefore, that the CAT region was formed by a shearing instability. But, what dynamics led to such low values of  $Ri$  in this layer? Was a gravity or inertia-gravity wave (IGW) involved in creating it?

The numerical simulations (all simulations with configuration R2, see Tab. 3) identified an IGW that propagated upwards from the region of the MTJ system (the former named SGW) as the striking perturbation in the fields of  $\theta$  and  $v_h$  (c.f. Figs. 3.9 to 2.7). It is clearly evident from Fig. 2.7, that this wave propagated directly into the region that coincided with the flight segment where the G-IV experienced the CAT (see Fig. 2.6). As explained before, to obtain a significantly modulated local  $Ri$  through a gravity wave, the conditions of (4.4) should be satisfied.

Unfortunately, it was not possible to isolate wave perturbations and background parameters from the available observational data. However, as indicated in Fig. 2.7, the SGW exhibited a rather large amplitude, which therefore strongly disturbed the fields of  $\theta$  and  $v_h$ . Note in particular the strong wave-like distortion of the isotachs around 200 hPa on the cyclonic shear-side of the STJ, but bear again in mind the coarse horizontal resolution between the individual dropsondes while interpreting this depiction. Thus, although not quantitatively verified, it is supposed that the SGW, at least, had a significant influence on the local  $Ri$  in the region of the CAT, and perhaps, then caused  $Ri$  to fall below its critical value  $Ri_c$ . Breaking of secondary small-scale Kelvin-Helmholtz waves ultimately generated the CAT.

Because the MM5-simulated horizontal velocities  $v_h$  in the core of the STJ were under-predicted (see Section 3.3), lower background vertical shear of the simulated  $v_h$  prevented the formation of low  $Ri$  in the region of the encountered CAT (see Fig. 3.10). It must be stressed that the mesoscale numerical model reproduced the generation and upward prop-

agation of the SGW through that region well. However, it remains uncertain how exactly the model reproduced the amplitude of the SGW.

Under consideration of the available observational data and the results of the numerical simulations, it is most likely that the generation of the CAT region can be explained by the dynamical processes discussed. However a few other processes should be taken into account:

- The upward propagating SGW packet might have been reflected by the strong LGW breaking region, located higher upwards from the flight level. Such a strong breaking region was simulated in runs R2 (see Fig. 3.10). Reflected waves could have propagated downward and, maybe, interacted with the upward propagating SGWs. At the end, wave interference or parametric instability might have caused a wave breaking region.
- Secondary small-scale waves (which are not resolved in the simulations) were generated in the LGW breaking region and propagated downwards into the flight level, and somehow contributed to the generation of CAT. Secondary waves that propagate away from a breaking region of convectively generated gravity waves were simulated explicitly by (Lane and Sharman 2006) in a three-dimensional model with numerical resolutions up to 150 m in all spatial directions. The simulations used here indicate the generation of small-scale waves (see Fig. 3.7 and the respective discussion), although the grid increments used are too coarse to from properly resolve such features (e.g. Lane and Sharman 2006, and references therein).
- Horizontally shorter gravity waves (which are not resolved in the present simulations) were generated in the strong shear layer below the MTJ system and propagated upwards into the flight level and somehow contributed to the generation of CAT. As horizontally shorter waves have larger group velocities, they could contribute significantly to a wave breakdown in the height region of the flight level.
- A high vertical shear of  $v_h$  around the flight level of the G-IV was sufficient to cause a shearing instability without the influence of gravity waves. This scenario is unlikely because both observations and simulations showed a gravity wave, which significantly perturbs the fields in the region of the G-IV flight and during its passage time.

Because no critical level of the simulated LGWs lay below 18 km, it is unlikely that IGW breaking at a critical level was directly involved in the generation of the G-IV-CAT. Ultimately, only numerical runs with higher resolution will be able to resolve the generation of CAT. There are essentially two routes: either to nest a large-eddy simulation code into the mesoscale simulations (as done by Lane et al. 2004; Koch et al. 2005) or to perform systematic sensitivity studies to investigate the influence of the wave amplitude on the specified forcing mechanisms using an idealized set up.



## 5 Inertia-gravity wave source dynamics

A diagnostic IGW source analysis using the MM5 simulation data is performed in this chapter. The focus is on the dominant stratospheric LGW packet (actually LGW and SGW), already discussed in Section 2.1 and Chapter 3. This IGW packet existed during the later stages of the baroclinic wave development. It appeared upstream and within the area of the upper-level trough axis around 03 UTC 29 Jan and then retained this relative position to the baroclinic wave during its lifetime (see Figs. 2.1-2.4). The IGW fronts were parallel to the north-westerly flow upstream of the trough, especially to the flow in the mid-troposphere. This configuration corresponds to mode 3 as mentioned by Koch et al. 2005 and was simulated earlier by Zhang 2004 with an idealized configuration but with much smaller amplitudes as in the real case simulated here. In addition to the LGWs, another IGW packet with phase lines perpendicular to the MTJ axis will be discussed here.

As already mentioned in the introduction, many different mechanisms that generate IGWs have to be considered (e.g. Fritts and Alexander 2003, and references therein) and it is not unlikely that these mechanisms act together.

### 5.1 Spontaneous adjustment

In recent years, many authors put forward spontaneous adjustment (also called geostrophic or balance adjustment) as an important mechanism of IGW generation in association with strong baroclinic jet flows. The generated IGWs are predominantly mesoscale waves (e.g. Uccellini and Koch 1987; Fritts and Luo 1992; Luo and Fritts 1993; O'Sullivan and Dunkerton 1995; Zhang et al. 2000; Pavelin et al. 2001; Hertzog et al. 2001; Plougonven et al. 2003; Zhang 2004). In this sense, IGWs are a way of spontaneous adjustment of an imbalance between the mass and velocity fields, resulting from the unsteady large-scale flow.

A flow is said to be balanced if the three-dimensional velocity field  $\mathbf{u}(\mathbf{x}, t)$  is functionally related to the mass field. This means that the flow has, in effect, fewer degrees of freedom than a fully general flow (McIntyre 2003). Geostrophic balance is the lowest in a hierarchy of more accurate balance relations. These include the states of geophysical fluid flows in which the non-linear balance equation (NBE),

$$2J(u, v) - \beta u + f\zeta - \alpha \nabla_h^2 p = 0 \quad (5.1)$$

presented here in Cartesian-height coordinates, applies.  $J$  is the Jacobian operator,  $u$  and  $v$  are zonal and meridional velocity components,  $\zeta$  is relative vorticity,  $f$  is the Coriolis parameter,  $\beta$  is  $\partial f / \partial y$ ,  $\alpha$  is specific volume ( $\alpha = \rho^{-1}$ ) and  $p$  is pressure.  $\nabla_h^2$  is the horizontal Laplace operator.

The hydrostatic balance is inherently contained in all these balance assumptions and only then one can identify mass with pressure fields. IGW motions are not contained in

such idealized states of the atmosphere, but it is supposed that large deviations from this balance, for example, given as the residual of the NBE,

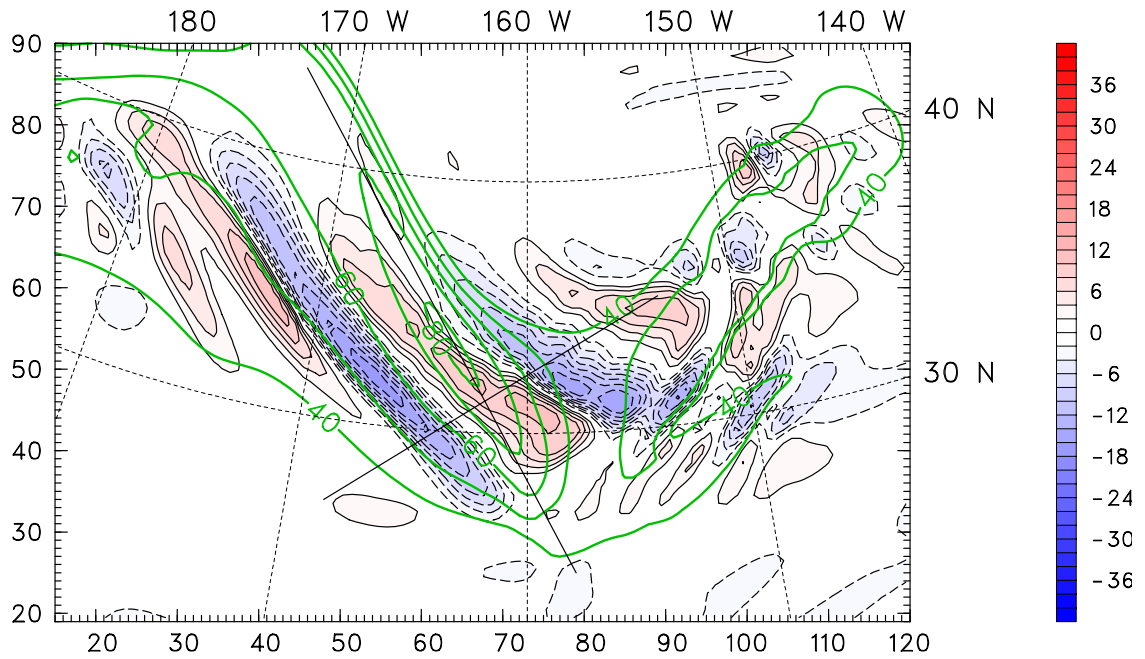
$$\Delta NBE = 2J(u, v) - \beta u + f\zeta - \alpha \nabla_h^2 p \quad (5.2)$$

result in a spontaneous adjustment back toward the balance (a mutual adjustment of mass and velocity distributions) by the emission of IGWs from the region where the large imbalance occurs (e.g. Zhang et al. 2000; McIntyre 2003; Zhang 2004). Because IGW motions are themselves not balanced, their signature exists also in the  $\Delta NBE$  field.

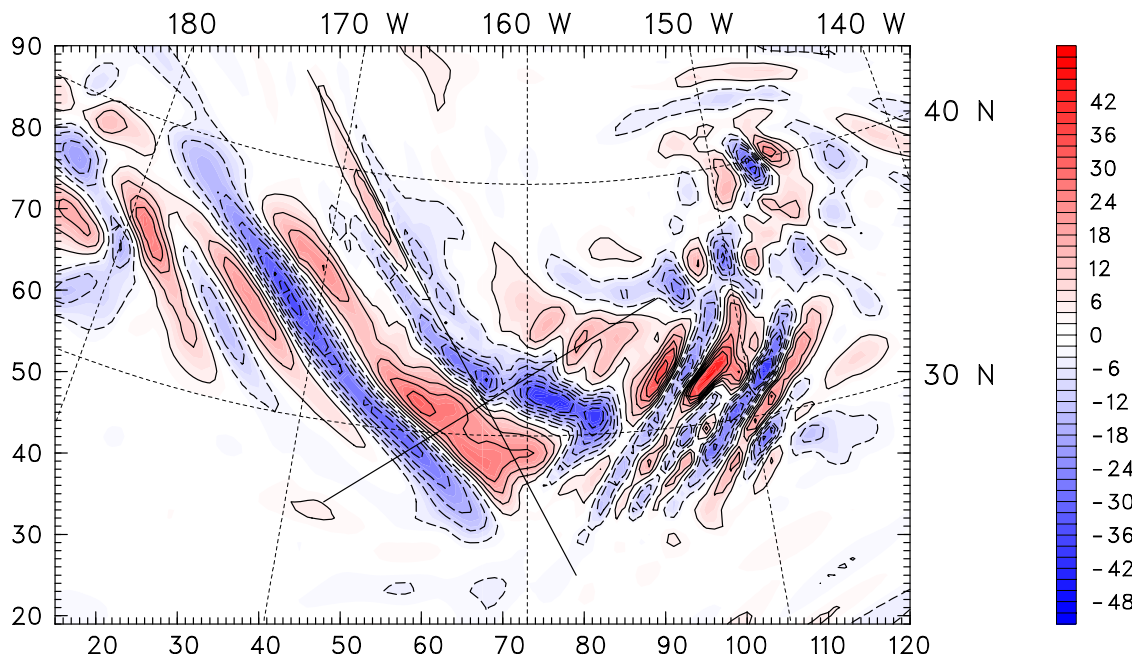
Fig. 5.1b shows the horizontal structure of the LGW by  $\Delta NBE$  at 16 km. It can be compared to the wave pattern of  $\nabla_h \cdot \mathbf{v}_h$  (Fig. 5.1a) (note that  $\Delta NBE$  is approximately  $d(\nabla_h \cdot \mathbf{v}_h)/dt$  (see Zhang et al. 2000; Lange 2002)). We chose data from a representative time having a mature stage of the LGW from 15 UTC on 29 Jan 1998 using run R1M D1 (see Tab. 3). From this time, the LGW was still in existence during the subsequent 9 hours of simulation.

The vertical cross-sections of Fig. 5.3 show some regions of imbalance by means of  $\Delta NBE$ . These were predominantly associated with wave motions: first, the LGW was strongly pronounced in the lower stratosphere above the dynamical tropopause ( $PV = 2$  PVU) with a maximum amplitude of  $|\Delta NBE|_{max} = 3.8 \cdot 10^{-8} \text{s}^{-2}$ . Run R2M D1 even had  $|\Delta NBE|_{max} = 6.4 \cdot 10^{-8} \text{s}^{-2}$  for the LGW at 15 UTC and  $|\Delta NBE|_{max} = 1.2 \cdot 10^{-7} \text{s}^{-2}$  after the frontal collapse at 22 UTC (not shown). Secondly, a mesoscale inertia-gravity wave (MGW) packet (e.g. Zhang 2004) with  $\lambda_h \approx 220$  km and  $\lambda_z \approx 6$  km, apparent in the field of  $\Delta NBE$  above the exit region of the MTJ south-east of the sharply rising tropopause in Fig. 5.3a. In contrast to the LGW, the MGW had phase lines perpendicular to the MTJ axis and a much smaller horizontal extent (see Fig. 5.4). Fig. 5.4b, the section from the dry simulation, shows a similar wave pattern as in previous studies of IGW generation in the exit regions of jets (e.g. O’Sullivan and Dunkerton 1995; Zhang 2004) and specifically of north-westerly jets in troughs (Plougonven et al. 2003). The different  $\Delta NBE$  fields in Fig. 5.4a and Fig. 5.4b were due to gravity waves excited from the parameterized moist convection. The MTJ system was slightly displaced between the two runs at this time (see the jet’s alignment to the baselines of the vertical sections).

The MGW packet apparently emanated from a region of large flow imbalance indicated by  $|\Delta NBE|_{max} = 3.8 \cdot 10^{-8} \text{s}^{-2}$ , associated with the exit region of the intense MTJ around 4 km altitude (Fig. 5.3a). The maximum magnitude of  $\Delta NBE$  associated with the MGW at 15 UTC was  $|\Delta NBE|_{max} = 2.8 \cdot 10^{-8} \text{s}^{-2}$  for run R1M D1 and  $|\Delta NBE|_{max} = 3.4 \cdot 10^{-8} \text{s}^{-2}$  for R2M D1 (not shown). Time looping showed that the MGWs appeared first with the intensification of the MTJ and the increase of flow deceleration in the exit of the jet around 09 UTC. Thereafter it remained in this position relative to the MTJ during its life time until around 22 UTC 30 Jan 1998. The MGW occurrence was consistently accompanied by large (linear) decelerations greater than  $\approx -6.0 \cdot 10^{-5} \text{s}^{-1}$  on the 310 K isentropic surface (note the blue contour line in Fig. 5.3). Fig. 5.6a constitutes an isentropic section at 310 K through this imbalance.



(a)



(b)

**Figure 5.1:** Data of run R1M D1 from 29 Jan 1998 at 15 UTC. (a)  $\nabla_h \cdot \mathbf{v}_h$  ( $10^{-5}\text{s}^{-1}$ , black solid contour lines positive, black dashed contour lines negative values with the following levels:  $\pm 2, \pm 4, \pm 6, \dots, 10^{-5}\text{s}^{-1}$  and shaded) at 16 km altitude and  $v_h > 40 \text{ ms}^{-1}$  ( $\text{ms}^{-1}$ , green contour lines,  $\Delta v_h = 10 \text{ ms}^{-1}$ ) on the 310 K isentropic surface. (b)  $\Delta NBE$  ( $10^{-9}\text{s}^{-2}$ , solid contour lines positive, dashed contour lines negative values with the following levels:  $\pm 4, \pm 10, \pm 16, \dots, 10^{-9}\text{s}^{-2}$  and shaded) at 16 km altitude.

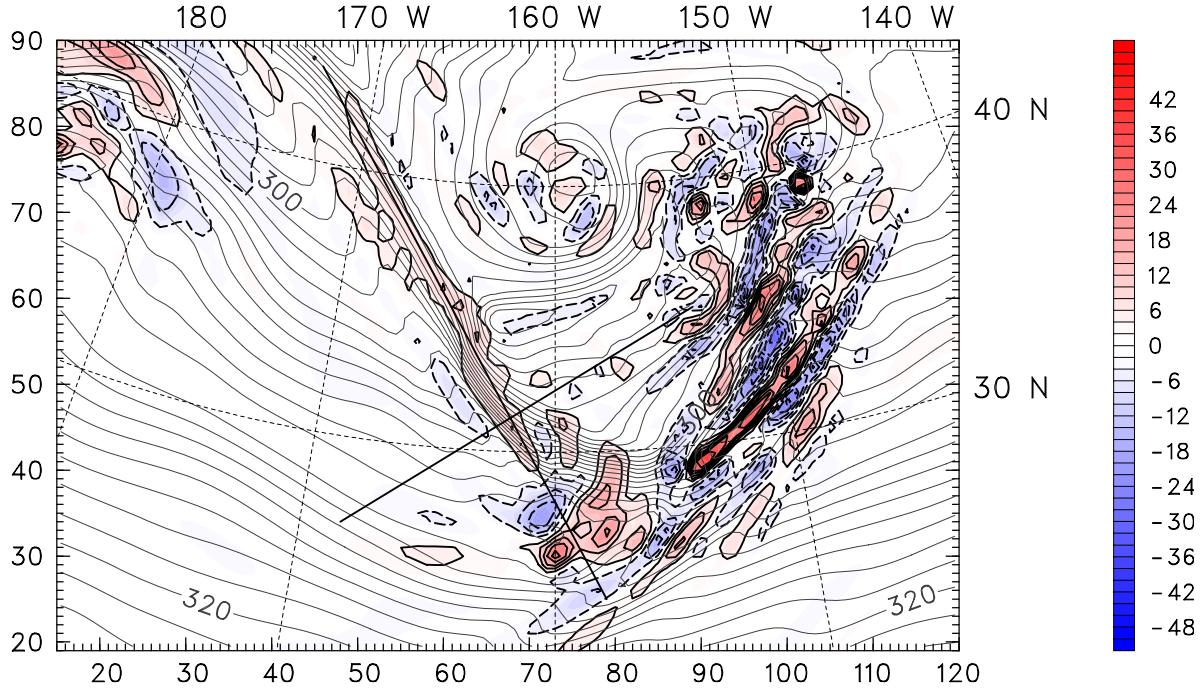


**Figure 5.2:** Data of run R1M D1 from 29 Jan 1998 at 15 UTC.  $\Delta NBE$  ( $10^{-9}\text{s}^{-2}$ , solid contour lines positive, dashed contour lines negative values with the following levels:  $\pm 4, \pm 10, \pm 16, \dots, 10^{-9}\text{s}^{-2}$  and shaded) and  $\theta$  (K, dark grey contour lines,  $\Delta\theta = 1$  K). All at 4.5 km altitude.

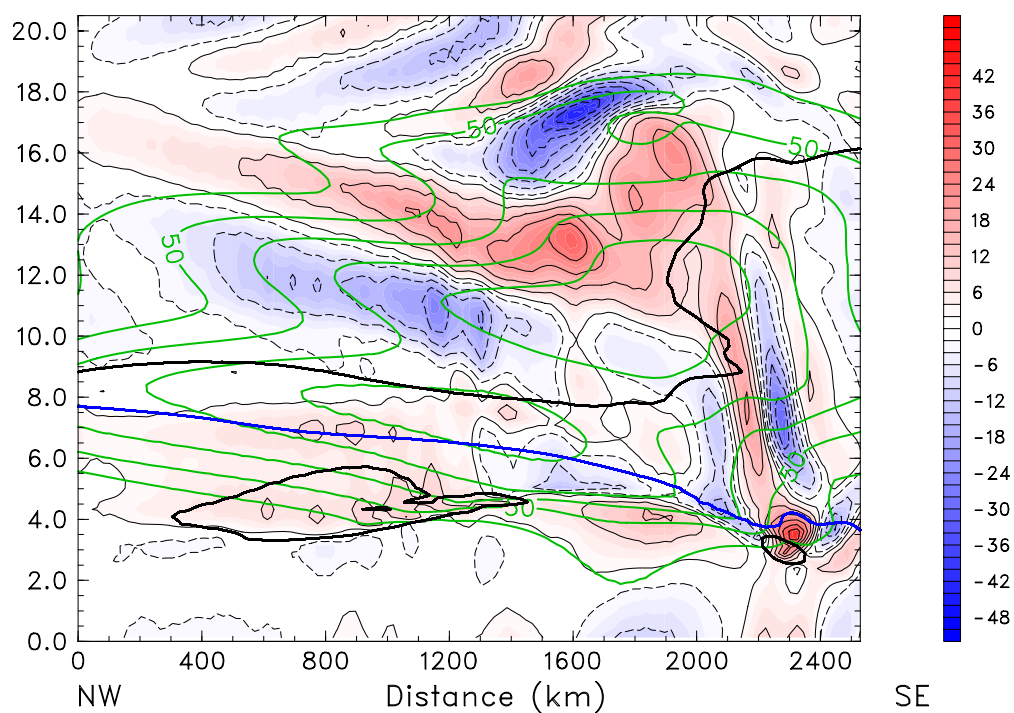
Imbalances were indicated also along the northwest-to-southeast aligned front around 4.5 km altitude (Fig. 5.2) and the vertical section along the front (Fig. 5.3a) with values of  $|\Delta NBE|_{max} = 1.0 \cdot 10^{-8}\text{s}^{-2}$ . Maximum magnitudes of  $\Delta NBE$  during strong low- to midtropospheric frontogenesis (or the frontal collapse) in run R2M around 20 UTC (see Figs. 3.4 and 3.8) were  $|\Delta NBE|_{max} = 2.2 \cdot 10^{-8}\text{s}^{-2}$  (not shown).

Another often used imbalance diagnostic is the dimensionless cross-stream Lagrangian Rossby number defined as,

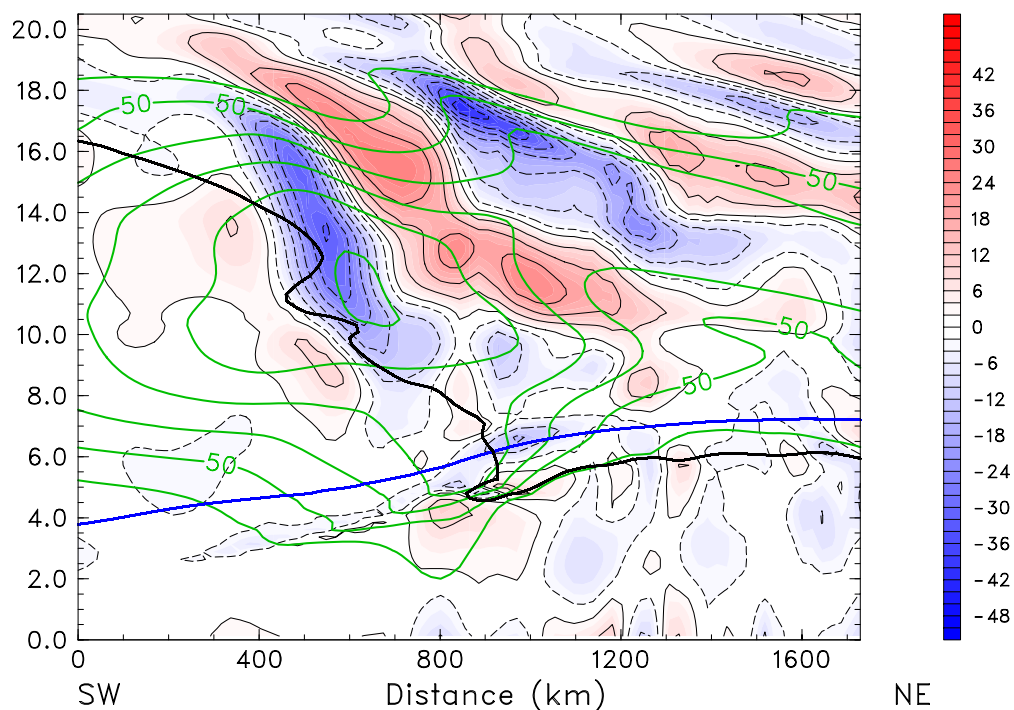
$$Ro_L^\perp = -\frac{Dv_h}{Dt} = \frac{v_a^\perp}{fv_h} \quad (5.3)$$

introduced by Koch and Dorian (1988) and later used in various studies of IGW generation by spontaneous (geostrophic) adjustment (e.g. O'Sullivan and Dunkerton 1995; Reeder and Griffiths 1996; Plougonven et al. 2003; Zülicke and Peters 2006). The quantity  $v_a^\perp$  refers to the cross-stream ageostrophic wind component (see Zülicke and Peters 2006). Vertical sections of  $Ro_L^\perp$  equal to Fig. 5.3 are given by Fig. 5.5.

The cross-stream Lagrangian Rossby number  $Ro_L^\perp$  as well showed unbalanced flow in the exit region of the MTJ in accordance with  $\Delta NBE$  (compare Fig. 5.5a to 5.3a



(a)



(b)

**Figure 5.3:** Data of run R1M D1 from 29 Jan 1998 at 15 UTC. Vertical cross-sections along the black northwest-to-southeast (a) and southwest-to-northeast (b) line sketched in Figs. 5.1 and 5.2.  $\Delta NBE$  ( $10^{-9}\text{s}^{-2}$ , black solid contour lines positive, dashed contour lines negative values with the following levels:  $\pm 2, \pm 8, \pm 14, \dots, 10^{-9}\text{s}^{-2}$  and shaded),  $v_h > 40 \text{ ms}^{-1}$  ( $\text{ms}^{-1}$ , green contour lines,  $\Delta v_h = 10 \text{ ms}^{-1}$ ),  $\theta = 310 \text{ K}$  (blue contour line),  $PV = 2 \text{ PVU}$  (thick black contour line).

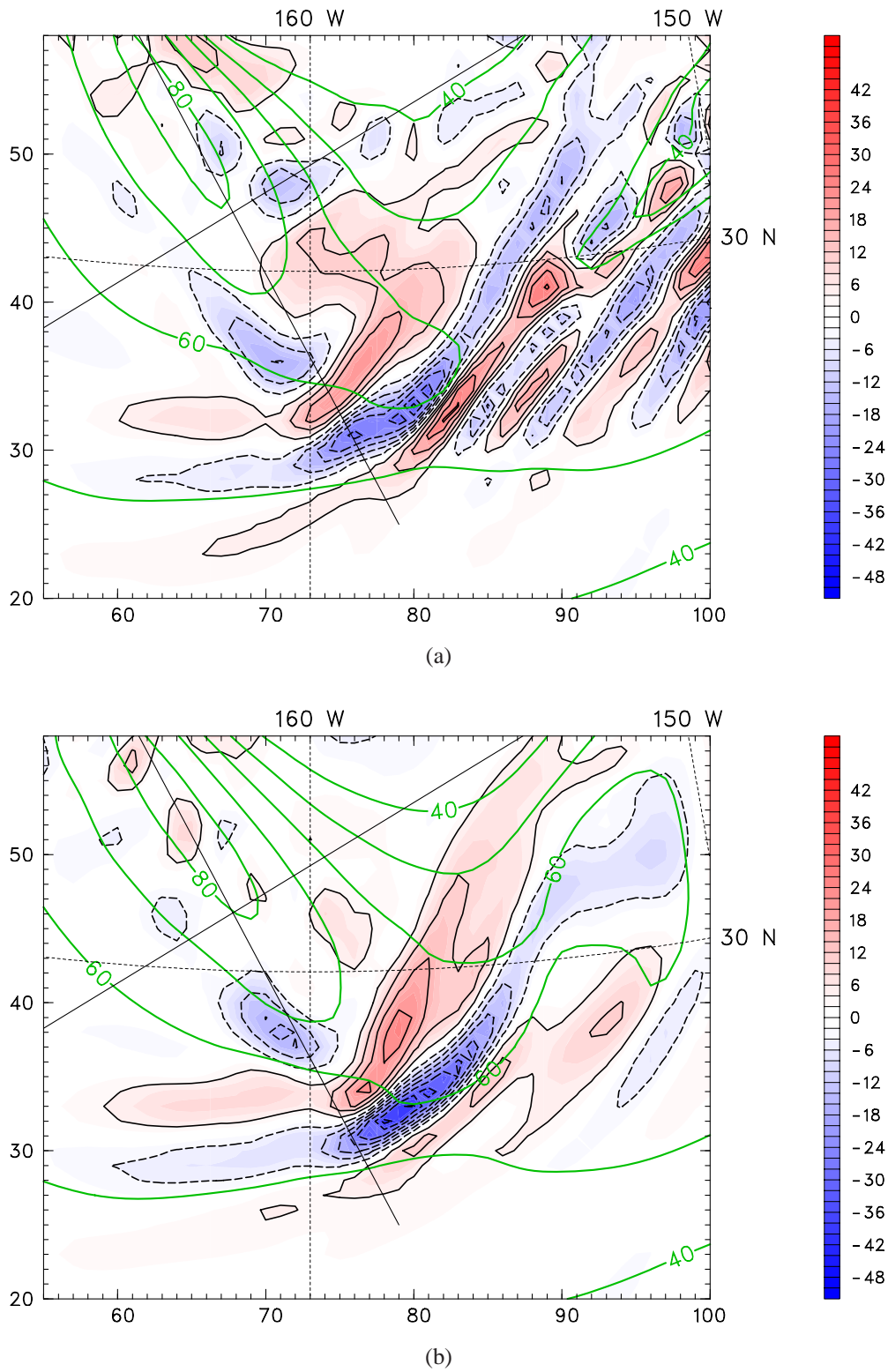
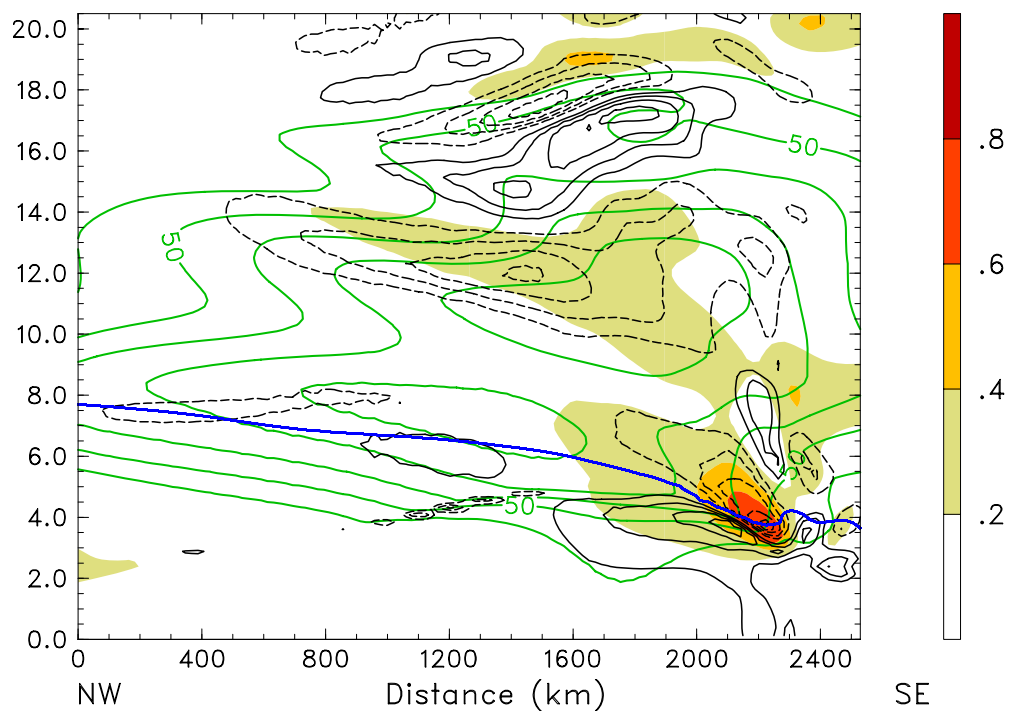
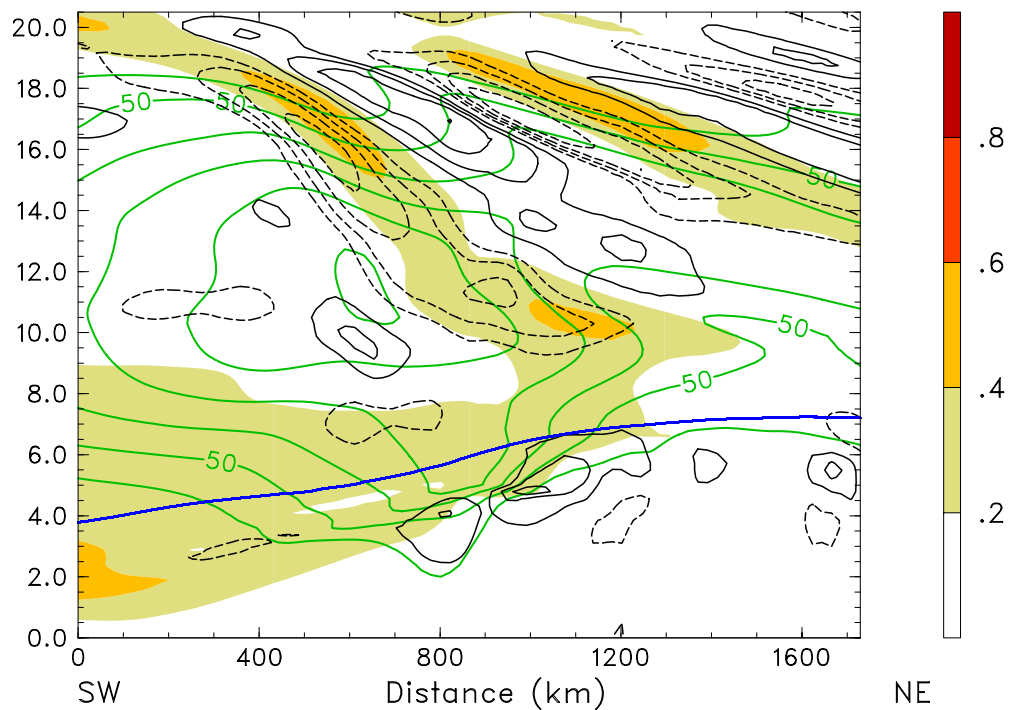


**Figure 5.4:** Data of run R1M D1 (a) and R1D D1 (b) from 29 Jan 1998 at 15 UTC.  $\Delta NBE$  ( $10^{-9}\text{s}^{-2}$ , black solid contour lines positive, dashed contour lines negative values with the following levels:  $\pm 2, \pm 8, \pm 14, \dots, 10^{-9}\text{s}^{-2}$  and shaded) and  $v_h > 40 \text{ ms}^{-1}$  ( $\text{ms}^{-1}$ , green contour lines,  $\Delta v_h = 10 \text{ ms}^{-1}$ ) all at 6.5 km altitude.



(a)



(b)

**Figure 5.5:** Data of run R1M D1 from 29 Jan 1998 at 15 UTC. Vertical cross-sections along the black northwest-to-southeast (a) and southwest-to-northeast (b) line sketched in Figs. 5.1 and 5.2.  $Ro_L^\perp$  (shaded),  $\nabla_h \cdot \mathbf{v}_h$  ( $10^{-5} \text{s}^{-1}$ , black solid contour lines positive, dashed contour lines negative values with the following levels:  $\pm 3, \pm 6, \pm 9, \dots, 10^{-5} \text{s}^{-1}$ ,  $v_h > 40 \text{ ms}^{-1}$  ( $\text{ms}^{-1}$ , green contour lines,  $\Delta v_h = 10 \text{ ms}^{-1}$ ),  $\theta = 310 \text{ K}$  (blue contour line).

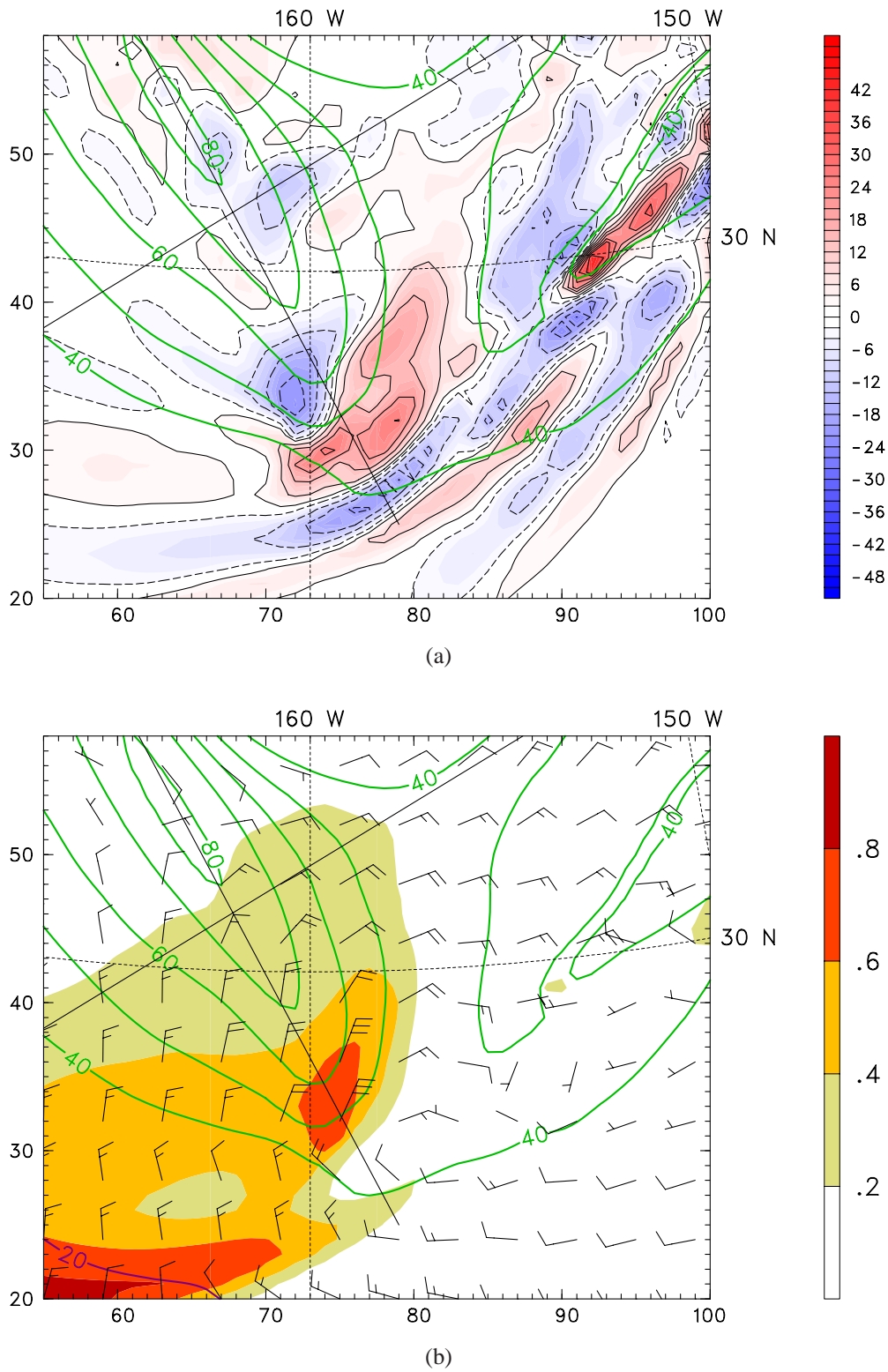


**Figure 5.6:** Data of run R1M D1 from 29 Jan 1998 at 15 UTC on the 310 K isentropic surface. (a)  $\Delta NBE$  ( $10^{-9} \text{s}^{-2}$ , black solid contour lines positive, dashed contour lines negative values with the following levels:  $\pm 2, \pm 8, \pm 14, \dots, 10^{-9} \text{s}^{-2}$  and shaded) and  $v_h > 40 \text{ ms}^{-1}$  ( $\text{ms}^{-1}$ , green contour lines,  $\Delta v_h = 10 \text{ ms}^{-1}$ ). (b)  $Ro_L$  (shaded), ageostrophic wind vectors ( $\text{ms}^{-1}$ , black barbs, half barb  $5 \text{ ms}^{-1}$ , full barb  $10 \text{ ms}^{-1}$ ),  $v_h > 40 \text{ ms}^{-1}$  ( $\text{ms}^{-1}$ , green contour lines,  $\Delta v_h = 10 \text{ ms}^{-1}$ ) and  $v_h = 20 \text{ ms}^{-1}$  (violet contour line).

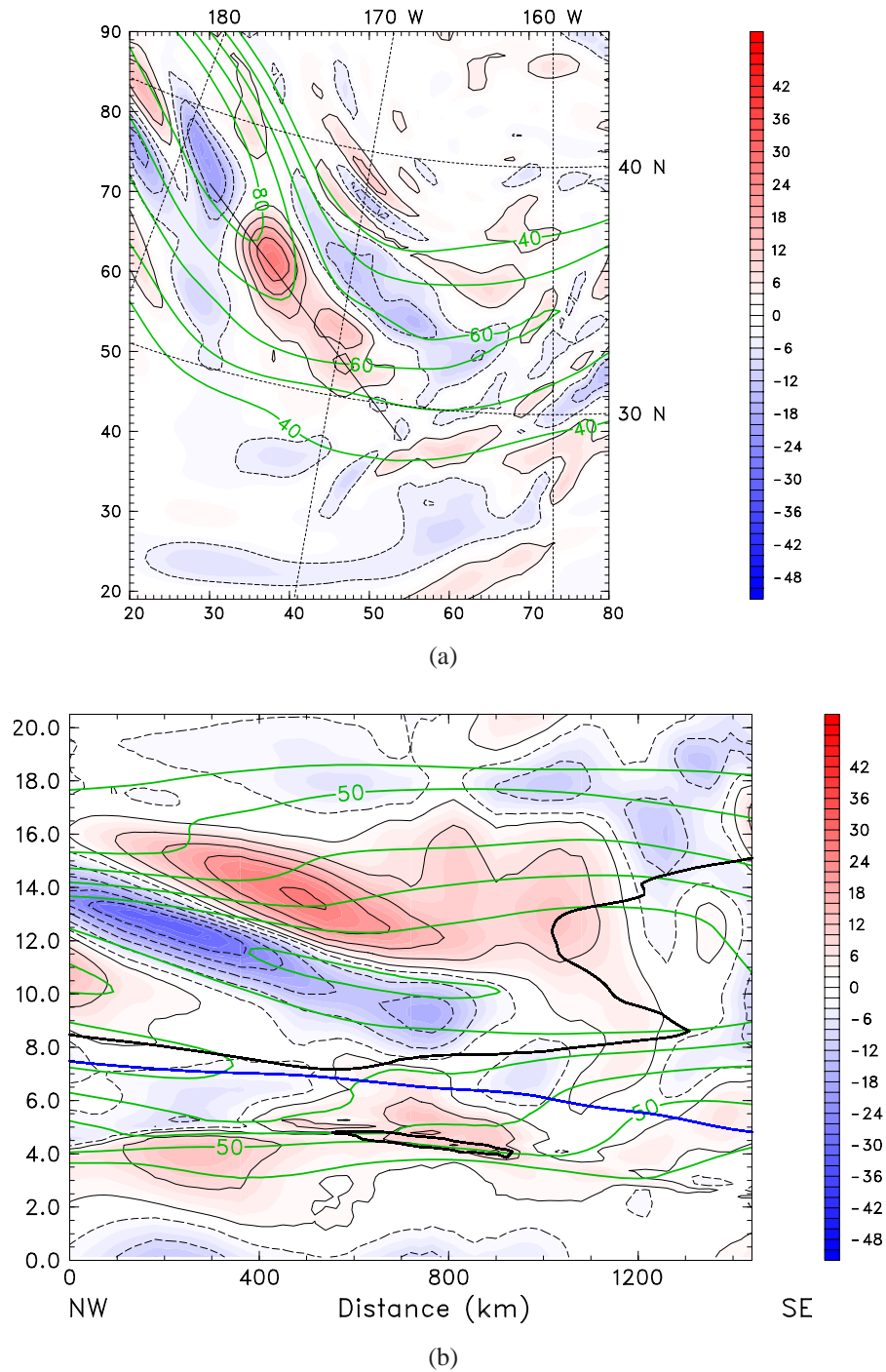


**Figure 5.7:** Data of run R1M D1 from 29 Jan 1998 at 05 UTC. (a)  $\Delta NBE$  ( $10^{-9}\text{s}^{-2}$ , black solid contour lines positive, dashed contour lines negative values with the following levels:  $\pm 4, \pm 10, \pm 16, \dots, 10^{-9}\text{s}^{-2}$  and shaded) at 14 km altitude,  $v_h > 40 \text{ ms}^{-1}$  ( $\text{ms}^{-1}$ , green contour lines,  $\Delta v_h = 10 \text{ ms}^{-1}$ ) at the 310 K isentropic surface. (b) Vertical cross-sections along the black northwest-to-southeast line sketched in (a).  $\Delta NBE$  ( $10^{-9}\text{s}^{-2}$ , black solid contour lines positive, dashed contour lines negative values with the following levels:  $\pm 2, \pm 8, \pm 14, \dots, 10^{-9}\text{s}^{-2}$  and shaded),  $v_h > 40 \text{ ms}^{-1}$  ( $\text{ms}^{-1}$ , green contour lines,  $\Delta v_h = 10 \text{ ms}^{-1}$ ),  $\theta = 310 \text{ K}$  (blue contour line),  $PV = 2 \text{ PVU}$  (thick black contour line).

and Fig. 5.6b to 5.6a). Values of  $Ro_L^\perp > 0.6$  indicated large imbalances in the decelerating flow (e.g. Plougonven et al. 2003; Zülicke and Peters 2006). High values of  $Ro_L^\perp (> 0.8)$  occurred also south-west of the MTJ-exit (Fig. 5.6b). These resulted from comparatively small ageostrophic cross-flow components in a region of low horizontal velocities  $v_h < 20 \text{ ms}^{-1}$  (see the violet contour line). Ultimately, no imbalance was indicated by  $Ro_L^\perp$  along the frontal zone (Fig. 5.5).

The LGW packet first appeared about 6 hours before the development of the imbalance in the exit of MTJ. Fig. 5.7 displays the incipient LGW with phase lines parallel to the MTJ at 05 UTC. There was neither a significant imbalance nor a MGW in the exit (Fig. 5.7b). Nevertheless, the LGW was quite pronounced at that time.

We tested the source code of the diagnostic tools used in this section on data from a former prestigious idealized model study by Fuqing Zhang (Texas A&M University) (Zhang 2004). Our code for  $\Delta NBE$  delivered the same results as his calculations.

The magnitudes of  $\Delta NBE$  in the idealized simulations of Zhang 2004 were about one order of magnitude lower than in the real case simulated here.

## 5.2 Shear generation

In addition to evanescent Kelvin-Helmholtz waves, shear layers can excite propagating gravity wave modes (Lalas and Einaudi 1976). In contrast to the simulations performed by Zhang 2004,  $Ri$  fell significantly below 1.0 in all our simulations in association with the development of the intense frontal MTJ around 03 UTC 29 Jan 1998. There was  $Ri < 1.0$  during the entire remaining time integration (until 00 UTC 30 Jan 1998). Fig. 5.8 displays  $Ri$  at 15 UTC as in Figs. 5.3 and 5.5.

## 5.3 Moist convective generation

The influence of moisture on the IGW had only minor consequences, if any. A comparison of Fig. 3.6 with Fig. 5.9 shows a qualitatively similar occurrence of the IGW in both sections even though the simulation of R2D (Fig. 5.9) did not include any moisture effects. Moist convection as an energy source of the LGW packet can consequently be eliminated.

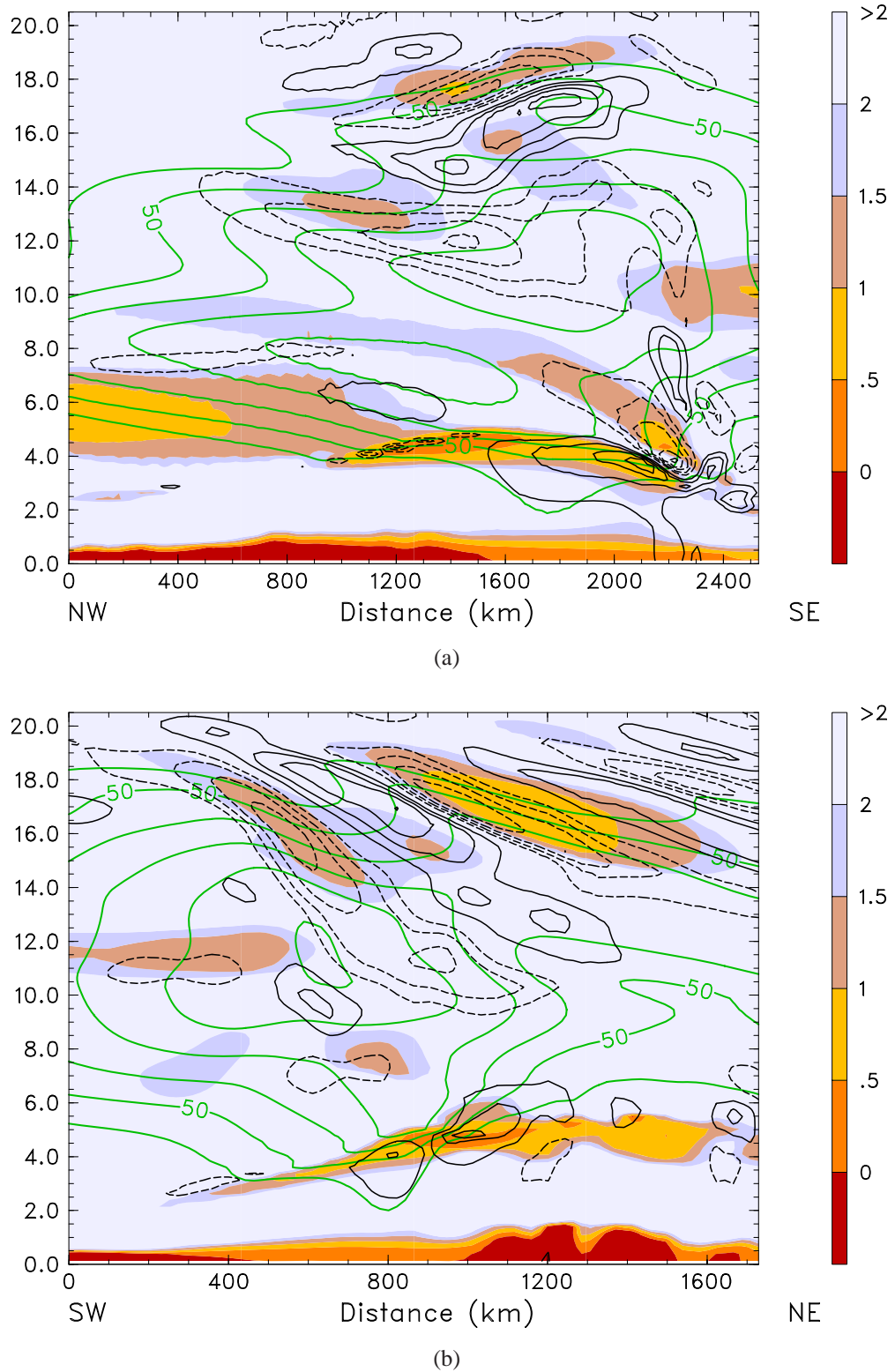
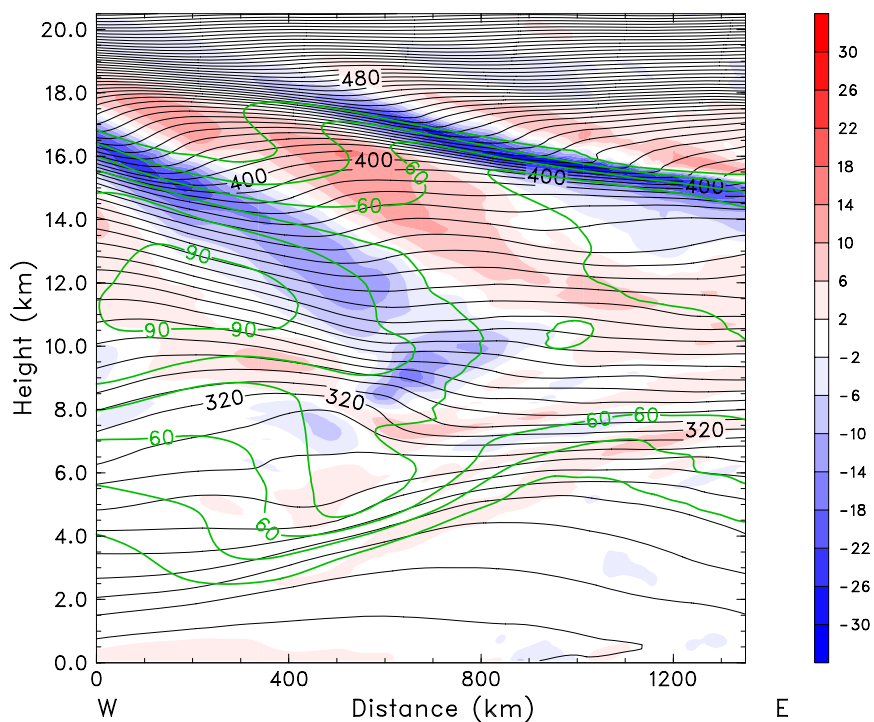
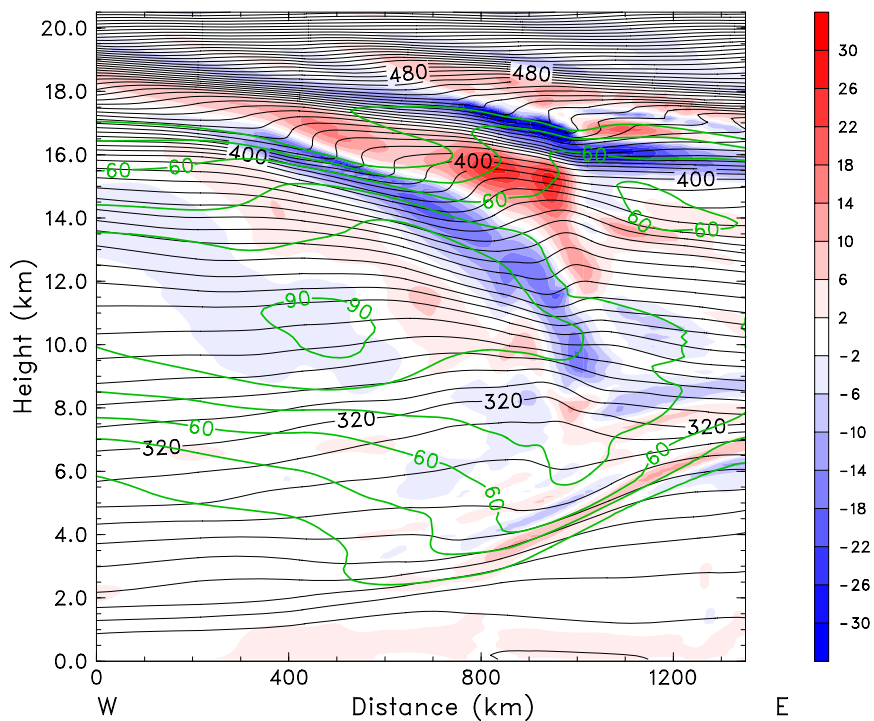


**Figure 5.8:** Data of run R1M D1 from 29 Jan 1998 at 15 UTC. Vertical cross-sections along the black northwest-to-southeast (a) and southwest-to-northeast (b) line sketched in Figs. 5.1 and 5.2.  $Ri$  (shaded),  $\nabla_h \cdot \mathbf{v}_h$  ( $10^{-5} \text{s}^{-1}$ , black solid contour lines positive, dashed contour lines negative values with the following levels:  $\pm 3, \pm 6, \pm 9, \dots, 10^{-5} \text{s}^{-1}$ ,  $v_h > 40 \text{ms}^{-1}$  ( $\text{ms}^{-1}$ , green contour lines,  $\Delta v_h = 10 \text{ms}^{-1}$ ).



(a)



(b)

**Figure 5.9:** Data of run R2D D2 from 29 Jan 1998 at (a) 18 and (b) 23 UTC. Vertical cross-section along the black west-to-east line sketched in Fig. 3.5.  $\theta$  (K, black contour lines,  $\Delta\theta = 4$  K),  $v_h$  ( $\text{ms}^{-1}$ , green contour lines,  $\Delta v_h = 10 \text{ms}^{-1}$ ) and  $\nabla_h \cdot \mathbf{v}_h$  ( $10^{-5} \text{s}^{-1}$ , shaded).

## 5.4 Summary

The MGW packet was generated by spontaneous adjustment associated with unbalanced flow in the exit of the MTJ. This was consistently indicated by  $\Delta NBE$  and  $Ro_L^\perp$ . No analogous imbalance was indicated along the frontal zone at low- to midtropospheric levels that was suggested to be the major source region of the LGW (and the SGW) by the analysis of Section 3.2. The LGW first appeared many hours before the imbalance in the exit of MTJ. This fact eliminates the imbalance in the MTJ-exit as the energy source for the large-amplitude LGW. A dynamical instability that caused the LGW may be possible, but seems unlikely because theories of shear instability generally predict maximum growth rates at much smaller horizontal wavelengths (Lalas and Einaudi 1976) and a perpendicular alignment of the wave phase lines to the shear vector. Low-frequency gravity waves or IGWs can be generated from direct topographic forcing (Dörnbrack et al. 2002), but this can surely be ruled out as a source of the LGW far away from any topography.

It is proposed that vertical accelerations (or vertical displacements of air parcels) associated with the secondary ageostrophic cross-frontal flow accompanying frontogenesis (see Holton 1992) could be a major source mechanism for the LGW (and for the SGW simulated in runs R2M).



## 6 Conclusion

The combination of observations, synoptic-scale meteorological analyses and high-resolution numerical simulations provided insight into the clear-air turbulence (CAT) encounter by the NOAA-G-IV research aircraft above the Pacific Ocean. The CAT was classified as moderate-to-severe.

Numerical experiments with high horizontal ( $\Delta X = 3$  km) and vertical ( $\Delta Z \approx 188$  m) resolutions were necessary to resolve the fast vertically propagating waves as the cross-front scale of the baroclinic zone collapsed rapidly at the end of the baroclinic amplification. The intense baroclinic development resulted in an alignment of the mid-tropospheric jet (MTJ) and the subtropical jet (STJ). This configuration was favorable to the vertical propagation of the gravity waves generated in the low- to midtropospheric levels.

Due to limitations in spatial resolution and the forcing of the synoptic-scale analyses, the mesoscale simulations were not able to simulate the CAT at the location where the G-IV encountered it. However, the basic mechanism which led to the CAT could be identified by the combination of observations and numerical modeling. The fast propagating gravity waves may have played a major role in the formation of the CAT.

This particular case examined here lead to the hypothesis that extreme CAT encounters are generated in breaking Rossby waves when the STJ becomes aligned with the frontal jet.

Based on the analysis presented, we showed that the large-amplitude inertia-gravity waves emanated from the region of the mid-tropospheric front/jet system. The dynamical state of the baroclinic development (cross-frontal scale contraction, occurrence of the MTJ) determined the horizontal wave length and amplitude of the inertia-gravity waves in the upper troposphere and lower stratosphere. Considering the similar wave propagation direction of the simulated larger-scale inertia-gravity waves (LGWs) and the smaller-scale inertia-gravity waves (SGWs) that developed later, it is hypothesized that the same dynamical source mechanisms caused their formation.

Diagnostics used in previous studies to detect sources of inertia-gravity waves ( $\Delta NBE$ ,  $Ro_L^\perp$ ) indicated unbalanced flow in the exit of the intense MTJ. This large imbalance generated mesoscale gravity waves (MGWs) with phase lines perpendicular to the flow by spontaneous (geostrophic, balance) adjustment.

No definite source mechanism could be found to generate the large-amplitude inertia-gravity waves with phase lines parallel to the flow. However, the study suggests the cross-flow past the low- to midtropospheric frontal zone as the source of the inertia-gravity waves (the LGWs and SGWs).

In the future, idealized numerical simulations can help to study the dependence of wave characteristics and instability mechanisms on tropospheric parameters. The configuration then requires a temporal development, i.e. intensification, of the tropospheric frontal zone.



## Appendix A

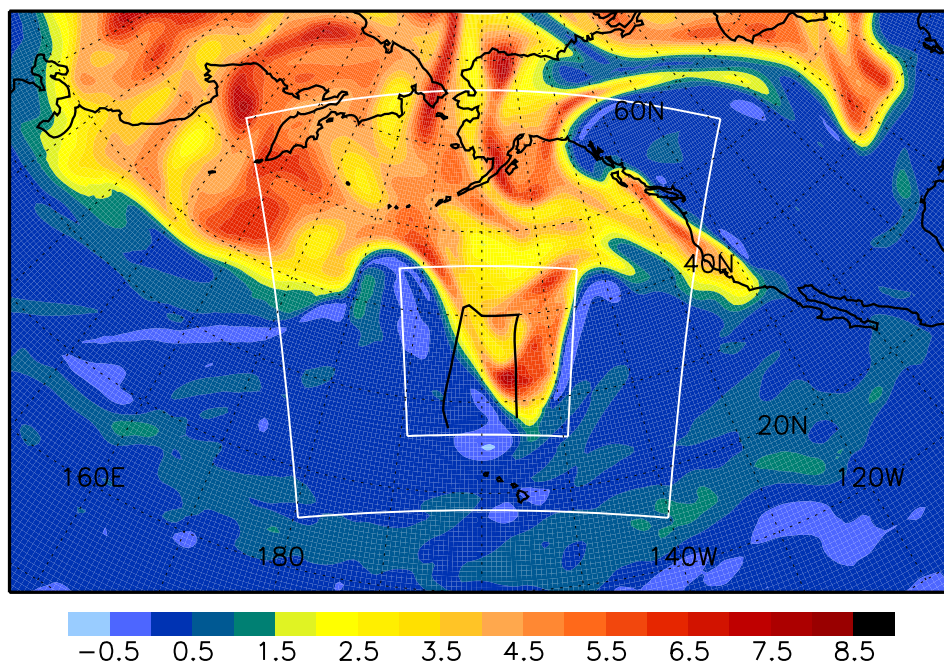
### MM5 configuration

Run	Domain	NX	NY	NZ	$\Delta X$ (km)	$\Delta Z$ (m)	$t_0$
R1M	1	145	145	144	36	$\approx 205$	00 UTC 29 Jan
	2	181	181	144	12	$\approx 205$	00 UTC 29 Jan
R1D	1	145	145	144	36	$\approx 205$	00 UTC 29 Jan
	2	181	181	144	12	$\approx 205$	00 UTC 29 Jan
R2M	1	145	145	157	27	$\approx 188$	12 UTC 29 Jan
	2	244	244	157	9	$\approx 188$	12 UTC 29 Jan
	3	301	217	157	3	$\approx 188$	12 UTC 29 Jan
R2D	1	145	145	157	27	$\approx 188$	12 UTC 29 Jan
	2	244	244	157	9	$\approx 188$	12 UTC 29 Jan
	3	301	217	157	3	$\approx 188$	12 UTC 29 Jan

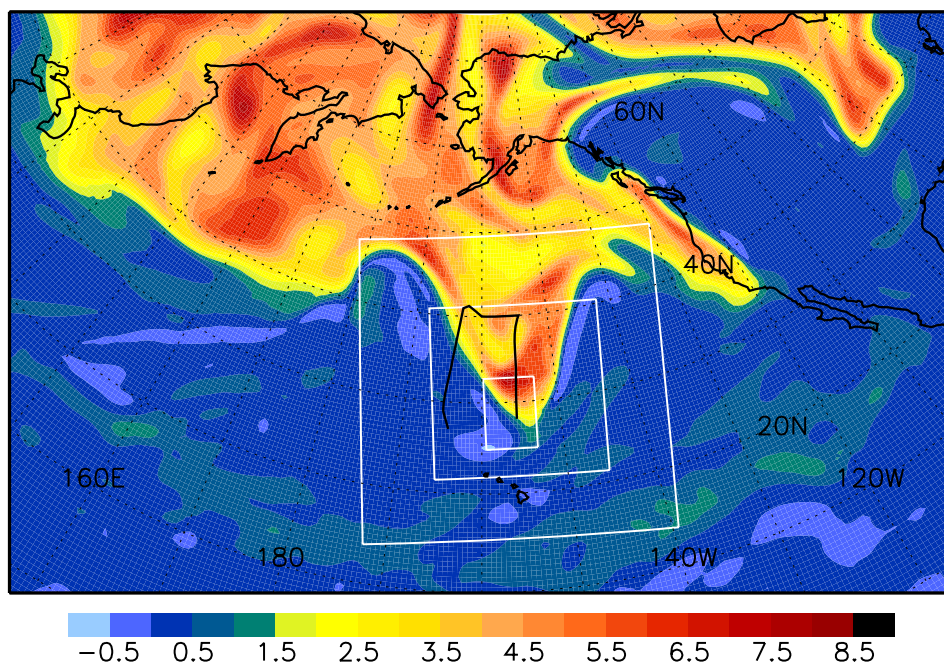
**Table 3:** Detailed listing of performed simulations. Configuration of the different simulations (Run) (R1, R2 were the different domain configurations (see Fig. A-1), D and M mean dry and full physics (moist), respectively). Designation of the nested model domains (Domain), the respective number of grid points in each dimension (NX,NY,NZ) and the resulting grid intervals ( $\Delta X, \Delta Z$ ). Note, NX is the number of grid points in the meridional direction and  $\Delta X = \Delta Y$ . Initialization time ( $t_0$ ).

The PSU/NCAR mesoscale weather prediction model MM5<sup>1</sup> was used to perform the high-resolution numerical simulations. The finite-difference model was initialized with T213-ECMWF analyses interpolated on a regular latitude/longitude grid of  $0.5^\circ \times 0.5^\circ$  resolution. These data were used also to provide boundary conditions at the lateral boundaries of the outer domain every 6 hours. The model used a sigma vertical coordinate, and its equations were solved in their non-hydrostatic compressible version. At the inner domain boundaries a two-way nesting was performed between domains of different horizontal model resolution. The upper boundary was set to 10 hPa. All simulations parameterized the boundary layer vertical diffusion with the Medium-Range Forecast (MRF) scheme. Full-physics (M) simulations included parameterizations for moist processes (Reisner) and convection (Grell). Radiation effects were neglected. An upper boundary condition was used to prevent the reflection of gravity waves (Zängl 2001). All the simulations were performed on a NEC-SX5 supercomputer.

<sup>1</sup><http://www.mmm.ucar.edu/mm5/>



(a)



(b)

**Figure A-1:** Model domain alignment of the MM5 simulations: (a) R1 and (b) R2 (white lines) (see Tab. 3). ECMWF analysis data from 29 Jan 1998 at 18 UTC: PV (shaded) on the 310K isentropic surface. Additionally, NOAA's G-IV flight track (black line)

## Acronyms

<b>CAT</b>	clear-air turbulence
<b>ECMWF</b>	European Centre for Medium-Range Weather Forecasts
<b>GPS</b>	Global Positioning System
<b>G-IV</b>	Gulfstream-IV
<b>IGW</b>	inertia-gravity wave
<b>ICL</b>	inertial critical level
<b>LGW</b>	larger-scale inertia-gravity wave
<b>MGW</b>	mesoscale inertia-gravity wave
<b>MM5</b>	Mesoscale Model, Version 5
<b>MTJ</b>	mid-tropospheric jet
<b>NBE</b>	non-linear balance equation
<b>NCAR</b>	National Centre for Atmospheric Research
<b>NOAA</b>	National Oceanographic and Atmospheric Administration
<b>NORPEX-98</b>	North Pacific Experiment 1998
<b>PSU</b>	Pennsylvania State University
<b>PV</b>	Ertel potential vorticity
<b>PVU</b>	potential vorticity units
<b>SGW</b>	smaller-scale inertia-gravity wave
<b>STJ</b>	subtropical jet



---

## Bibliography

- Atlas, D., J. I. Metcalf, J. H. Richter, and E. E. Gossard, 1970: The Birth of 'CAT' and Microscale Turbulence. *Journal of Atmospheric Sciences*, **27**, 903–913.
- Bacmeister, J. T., P. A. Newman, B. L. Gary, and R. K. Chan, 1994: An algorithm for forecasting mountain wave-related turbulence in the stratosphere. *Weather and Forecasting*, **9**, 241–253.
- Bluestein, H. B., 1993: *Synoptic-dynamic meteorology in midlatitudes. Vol. 2, Observations and theory of weather systems*. Oxford University Press.
- Booker, J. R. and F. P. Bretherton, 1967: The critical layer for internal gravity waves in a shear flow. *Journal of Fluid Mechanics*, **27**, 513–539.
- Browning, K. A., 1971: Structure of the atmosphere in the vicinity of large-amplitude Kelvin-Helmholtz billows. *Quarterly Journal of the Royal Meteorological Society*, **97**, 283–299.
- Clark, T. L., W. D. Hall, R. M. Kerr, D. Middleton, L. Radke, F. M. Ralph, P. J. Neiman, and D. Levinson, 2000: Origins of aircraft-damaging clear-air turbulence during the 9 December 1992 Colorado downslope windstorm: Numerical simulations and comparison with observations. *Journal of the Atmospheric Sciences*, **57**, 1105–1131.
- Danielsen, E. F., 1968: Stratospheric-Tropospheric Exchange Based on Radioactivity, Ozone and Potential Vorticity. *Journal of Atmospheric Sciences*, **25**, 502–518.
- Dörnbrack, A., 1998: Turbulent mixing by breaking gravity waves. *Journal of Fluid Mechanics*, **375**, 113–141.
- Dörnbrack, A., T. Birner, A. Fix, H. Flentje, A. Meister, H. Schmid, E. V. Browell, and M. J. Mahoney, 2002: Evidence for inertia gravity waves forming polar stratospheric clouds over Scandinavia. *Journal of Geophysical Research (Atmospheres)*, **107**, 30–1, doi:10.1029/2001JD000452.
- Dörnbrack, A., M. Leutbecher, R. Kivi, and E. Kirö, 1999: Mountain wave induced record low stratospheric temperatures above northern Scandinavia. *Tellus*, **51**, 951–963.
- Dudhia, J., 1993: A nonhydrostatic version of the Penn State-NCAR mesoscale model: Validation tests and simulation of an Atlantic cyclone and cold front. *Monthly Weather Review*, **121**, 1493–1513.
- Dutton, J. A. and H. A. Panofsky, 1970: Clear air turbulence: A mystery may be unfolding. *Science*, **167**.

- Eichenbaum, H., 2003: Historical overview of turbulence accidents and case study analysis. *MCR Federal, inc.Rep.BR-M021/080-1*, 82 pp.
- Einaudi, F. and D. P. Lalas, 1975: Wave-Induced Instabilities in an Atmosphere Near Saturation. *Journal of the Atmospheric Sciences*, **32**, 536–547.
- Eliassen, A. and E. Palm, 1960: On the transfer of energy in stationary mountain waves. *Geofysiske Publikasjoner XXII*, 1–23.
- Ellrod, G. P. and D. I. Knapp, 1992: An objective clear-air turbulence forecasting technique: Verification and operational use. *Weather and Forecasting*, **7**, 150–165.
- Fritts, D. C. and M. J. Alexander, 2003: Gravity wave dynamics and effects in the middle atmosphere. *Reviews of Geophysics*, **41**, 3–1, doi:10.1029/2001RG000106.
- Fritts, D. C. and Z. Luo, 1992: Gravity Wave Excitation by Geostrophic Adjustment of the Jet Stream. Part I: Two-Dimensional Forcing. *Journal of the Atmospheric Sciences*, **49**, 681–697.
- Gill, A., 1982: *Atmosphere-Ocean Dynamics*. Academic Press.
- Guest, F. M., M. J. Reeder, C. J. Marks, and D. J. Karoly, 2000: Inertia-gravity waves observed in the lower stratosphere over Macquarie island. *Journal of the Atmospheric Sciences*, **57**, 737–752.
- Hertzog, A., C. Souprayen, and A. Hauchecorne, 2001: Observation and backward trajectory of an inertio-gravity wave in the lower stratosphere. *Annales Geophysicae*, **19**, 1141–1155.
- Holton, J. R., 1992: *An introduction to dynamic meteorology*. International geophysics series, San Diego, New York: Academic Press, 3rd ed.
- Hoskins, B. J., M. E. McIntyre, and A. W. Robertson, 1985: On the use and significance of isentropic potential vorticity maps. *Quarterly Journal of the Royal Meteorological Society*, **111**, 877–946.
- Howard, L. N., 1961: Note on the Paper of John W. Miles. *Journal of Fluid Mechanics*, **10**, 509.
- Jiang, Q. and J. D. Doyle, 2004: Gravity wave breaking over the central Alps: Role of complex terrain. *Journal of the Atmospheric Sciences*, **61**, 2249–2266.
- Keyser, D. and M. A. Shapiro, 1986: A review of the structure and dynamics of upper-level frontal zones. *Monthly Weather Review*, **114**, 452–499.

- Koch, S. E. and P. B. Dorian, 1988: A mesoscale gravity wave event observed during CCOPE. Part III: Wave environment and probable source mechanisms. *Monthly Weather Review*, **116**, 2570–2592.
- Koch, S. E., B. D. Jamison, C. Lu, T. L. Smith, E. I. Tollerud, C. Girz, N. Wang, T. P. Lane, M. A. Shapiro, D. D. Parrish, and O. R. Cooper, 2005: Turbulence and Gravity Waves within an Upper-Level Front. *Journal of the Atmospheric Sciences*, **62**, 3885–3908.
- Lalas, D. P. and F. Einaudi, 1976: On the Characteristics of Gravity Waves Generated by Atmospheric Shear Layers. *Journal of Atmospheric Sciences*, **33**, 1248–1259.
- Lane, T. P., J. D. Doyle, R. Plougonven, M. A. Shapiro, and R. D. Sharman, 2004: Observations and numerical simulations of inertia gravity waves and shearing instabilities in the vicinity of a jet stream. *Journal of the Atmospheric Sciences*, **61**, 2692–2706.
- Lane, T. P. and R. D. Sharman, 2006: Gravity wave breaking, secondary wave generation, and mixing above deep convection in a three-dimensional cloud model. *Geophysical Research Letters*, in press.
- Lane, T. P., R. D. Sharman, T. L. Clark, and H.-M. Hsu, 2003: An Investigation of Turbulence Generation Mechanisms above Deep Convection. *Journal of Atmospheric Sciences*, **60**, 1297–1321.
- Lange, H., 2002: *Die Physik des Wetters und des Klimas. Ein Grundkurs zur Theorie des Systems Atmosphäre*. Reimer.
- Langland, R. H., Z. Toth, R. Gelaro, I. Szunyogh, M. A. Shapiro, S. J. Majumdar, R. E. Morss, G. D. Rohaly, C. Velden, N. Bond, and C. H. Bishop, 1999: The North Pacific Experiment (NORPEX-98): Targeted Observations for Improved North American Weather Forecasts. *Bulletin of the American Meteorological Society*, vol. 80, Issue 7, pp.1363-1384, **80**, 1363–1384.
- Luo, Z. and D. C. Fritts, 1993: Gravity-Wave Excitation by Geostrophic Adjustment of the Jet Stream. Part II: Three-Dimensional Forcing. *Journal of the Atmospheric Sciences*, **50**, 104–115.
- McIntyre, M. E., 2003: Balanced flow. *Encyclopedia of Atmospheric Sciences*. Academic Press., **2**, 680–685.
- Miles, J., 1986: Richardson's criterion for the stability of stratified shear flow. *Physics of Fluids*, **29**, 3470–3471.
- Miles, J. W., 1961: On the stability of heterogeneous shear flows. *Journal of Fluid Mechanics*, **10**, 496.

- Moldovan, H., F. Lott, and H. Teitelbaum, 2002: Wave breaking and critical levels for propagating inertio-gravity waves in the lower stratosphere. *Quarterly Journal of the Royal Meteorological Society*, **128**, 713–732.
- Nappo, C. J., 2002: *An Introduction to Atmospheric Gravity Waves*. Academic Press, 2002 International Geophysics Series, vol. 85, ISBN 0125140827.
- O’Sullivan, D. and T. J. Dunkerton, 1995: Generation of inertia-gravity waves in a simulated life cycle of baroclinic instability. *Journal of the Atmospheric Sciences*, **52**, 3695–3716.
- Pavelin, E., J. A. Whiteway, and G. Vaughan, 2001: Observation of gravity wave generation and breaking in the lowermost stratosphere. *Journal of Geophysical Research (Atmospheres)*, **106**, 5173–5180.
- Plougonven, R., H. Teitelbaum, and V. Zeitlin, 2003: Inertia gravity wave generation by the tropospheric midlatitude jet as given by the Fronts and Atlantic Storm-Track Experiment radio soundings. *Journal of Geophysical Research (Atmospheres)*, **108**, 14–+, doi:10.1029/2003JD003535.
- Reeder, M. J. and M. Griffiths, 1996: Stratospheric inertia-gravity waves generated in a numerical model of frontogenesis. II: Wave sources, generation mechanisms and momentum fluxes. *Quarterly Journal of the Royal Meteorological Society*, **122**, 1175–1195.
- Shapiro, M. A., 1980: Turbulent Mixing within Tropopause Folds as a Mechanism for the Exchange of Chemical Constituents between the Stratosphere and Troposphere. *Journal of Atmospheric Sciences*, **37**, 994–1004.
- Sharman, R., C. Tebaldi, G. Wiener, and J. Wolff, 2006: An integrated approach to mid- and upper-level turbulence forecasting. *Weather and Forecasting*, in press.
- Shutts, G., 1995: Gravity-wave drag parametrization over complex terrain: The effect of critical-level absorption in directional wind-shear. *Quarterly Journal of the Royal Meteorological Society*, **121**, 1005–1021.
- Smith, S. A. and A. D. DelGenio, 2001: Analysis of aircraft, radiosonde, and radar observations in cirrus clouds observed during FIRE II: The interactions between environmental structure, turbulence, and cloud microphysical properties. *Journal of the Atmospheric Sciences*, **58**, 451–461.
- Sprenger, M., M. Croci Maspoli, and H. Wernli, 2003: Tropopause folds and cross-tropopause exchange: A global investigation based upon ECMWF analyses for the time period March 2000 to February 2001. *Journal of Geophysical Research (Atmospheres)*, **108**, 3–1, doi:10.1029/2002JD002587.

- Thomas, L., R. M. Worthington, and A. J. McDonald, 1999: Inertia-gravity waves in the troposphere and lower stratosphere associated with a jet stream exit region. *Annales Geophysicae*, **17**, 115–121.
- Thompson, R. O. R. Y., 1978: Observation of inertial waves in the stratosphere. *Quarterly Journal of the Royal Meteorological Society*, **104**, 691–698.
- Thorncroft, C. D., B. J. Hoskins, and M. E. McIntyre, 1993: Two paradigms of baroclinic-wave-life-cycle behaviour. *Quarterly Journal of the Royal Meteorological Society*, **119**, 17–55.
- Uccellini, J. and S. E. Koch, 1987: The synoptic setting and possible source mechanisms for mesoscale gravity wave events. *Monthly Weather Review*, **115**, 721–729.
- Weissmann, M., R. Busen, A. Dörnbrack, S. Rahm, and O. Reitebuch, 2005: Targeted observations with an airborne wind lidar. *Journal of Atmospheric and Oceanic Technology*, **22**, 1706–1719.
- Zängl, G., 2001: An improvement of the upper radiative boundary condition. (<http://www.mmm.ucar.edu/mm5/workshop/ws01/zaengl1.pdf>).
- Zhang, F., 2004: Generation of Mesoscale Gravity Waves in Upper-Tropospheric Jet-Front Systems. *Journal of the Atmospheric Sciences*, **61**, 440–457.
- Zhang, F., S. Koch, C. A. Davis, and M. L. Kaplan, 2000: A survey of unbalanced flow diagnostics and their application. *Advances in Atmospheric Sciences*, **17**, 165–183.
- Zhang, F., S. Wang, and R. Plougonven, 2004: Uncertainties in using the hodograph method to retrieve gravity wave characteristics from individual soundings. *Geophysical Research Letters*, **31**, 11110–+.
- Züllicke, C. and D. Peters, 2006: Simulation of inertia-gravity waves in a poleward breaking Rossby wave. *Journal of the Atmospheric Sciences*.



## Danksagung

Mein Dank gilt vor allem Dr. Andreas Dörnbrack. Er führte mich leidenschaftlich an das Thema der Diplomarbeit heran und stand mir in allen Fragen immer hilfreich zur Seite. Prof. Roger K. Smith danke ich für wertvolle Anregungen zum Inhalt und zur Formulierung der Arbeit. Auch gilt mein Dank Dr. Melvin A. Shapiro (NOAA) für die Bereitstellung von Abbildungen und Informationen zum Flugverlauf der Messkampagne. Des weiteren möchte ich mich bei Dr. Christoph Zülicke (IAP Kühlungsborn) für die Bereitstellung von Quellcode bedanken. Dr. Fuqing Zhang (Texas A&M University) gab mir die Möglichkeit meinen programmierten Quellcode an seinen Simulationsdaten zu testen. Ich danke dafür. Meiner Abteilung am Institut für Physik der Atmosphäre, allen voran Dr. George Craig, danke ich für die angenehme Umfeld. Winfried Beer stand immer für Fragen mit den Rechnern im Institut bereitwillig und kompetent zu Verfügung. Vielen Dank. Jörg Wegener (Lund University) verdient dank für die Unterstützung bei der Benutzung des Textsatzprogrammes LaTeX. Dem Deutschen Zentrum für Luft- und Raumfahrt (DLR) danke ich für die Bereitstellung eines Arbeitsplatzes und die Versorgung mit Hard- und Software.

Für Elvira, Meike, Richard, Stephanie und Lieselotte.



## **Erklärung**

Die vorliegende Diplomarbeit wurde selbstständig verfasst. Die verwendeten Quellen und Hilfsmittel sind angegeben. Diese Arbeit lag bisher nicht zur Erlangung eines Diplomgrades vor.

München, November 2006

Christian Kühnlein